

University of Windsor

## Scholarship at UWindor

---

Electronic Theses and Dissertations

Theses, Dissertations, and Major Papers

---

10-5-2017

# ANALYSIS OF FLOW STRUCTURES AROUND INCLINED BLUFF BODIES

Kohei Fukuda  
*University of Windsor*

Follow this and additional works at: <https://scholar.uwindsor.ca/etd>

---

### Recommended Citation

Fukuda, Kohei, "ANALYSIS OF FLOW STRUCTURES AROUND INCLINED BLUFF BODIES" (2017). *Electronic Theses and Dissertations*. 7258.

<https://scholar.uwindsor.ca/etd/7258>

This online database contains the full-text of PhD dissertations and Masters' theses of University of Windsor students from 1954 forward. These documents are made available for personal study and research purposes only, in accordance with the Canadian Copyright Act and the Creative Commons license—CC BY-NC-ND (Attribution, Non-Commercial, No Derivative Works). Under this license, works must always be attributed to the copyright holder (original author), cannot be used for any commercial purposes, and may not be altered. Any other use would require the permission of the copyright holder. Students may inquire about withdrawing their dissertation and/or thesis from this database. For additional inquiries, please contact the repository administrator via email ([scholarship@uwindsor.ca](mailto:scholarship@uwindsor.ca)) or by telephone at 519-253-3000ext. 3208.

ANALYSIS OF FLOW STRUCTURES AROUND INCLINED BLUFF BODIES

by

Kohei Fukuda

A Dissertation

Submitted to the Faculty of Graduate Studies

through Mechanical, Automotive and Materials Engineering

in Partial Fulfillment of the Requirements for

the Degree of Doctor of Philosophy at the

University of Windsor

Windsor, Ontario, Canada

2017

© 2017 Kohei Fukuda

ANALYSIS OF FLOW STRUCTURES AROUND INCLINED BLUFF BODIES

by

Kohei Fukuda

APPROVED BY:

---

E. Savory, External Examiner  
Western University

---

R. Carriveau  
Department of Civil and Environmental Engineering

---

O. Iqbal  
Fiat Chrysler Automobiles

---

G. Rankin  
Department of Mechanical, Automotive & Materials Engineering

---

B. Zhou  
Department of Mechanical, Automotive & Materials Engineering

---

R. Barron, Co-Advisor  
Department of Mechanical, Automotive & Materials Engineering

---

R. Balachandar, Co-Advisor  
Department of Mechanical, Automotive & Materials Engineering

September 20, 2017

## **Declaration of Co-Authorship / Previous Publication**

### **I. Co-Authorship Declaration**

I hereby declare that this thesis incorporates the outcome of joint research undertaken in collaboration with my co-supervisors, Dr. Balachandar and Dr. Barron. The collaboration is covered in Chapter 3 and 4 of the thesis. In all cases, the key ideas, primary contributions, numerical simulations, data analysis and interpretation were performed by the author, and the contributions of the co-authors in the associated journal and conference publications were primarily through the provision of guidance and discussions on technical issues and editing of the manuscripts.

I am aware of the University of Windsor Senate Policy on Authorship and I certify that I have properly acknowledged the contributions of other researchers to my thesis and have obtained written permission from each of the co-authors to include the above materials in my thesis.

I certify that, with the above qualifications, this thesis, and the research to which it refers, is the product of my own work.

## II. Declaration of Previous Publication

This thesis includes three original papers that have been previously published/submitted for publication in peer-reviewed journals and conference proceedings as indicated below:

Thesis Chapter	Publication title/full citation	Publication status
Chapter 3	Fukuda, K., Balachandar, R., and Barron, R.M., 2017, Flow past an infinitely long inclined flat plate. <i>Physics of Fluids</i> .	Under review
Chapter 3	Fukuda, K., Balachandar, R., and Barron, R.M., 2018, Numerical investigation of three-dimensional fluid structures developed in the wake of an infinitely long inclined flat plate. 3 <sup>rd</sup> Thermal and Fluids Engineering Conference, Fort Lauderdale, Florida, USA, March 4-7.	Under review
Chapter 4	Fukuda, K., Balachandar, R., and Barron, R.M., 2017, Analysis of flow structures around an inclined plate near a wall. <i>ASME Journal of Fluid Engineering</i> .	Under review

I certify that I have obtained written permission from the copyright owners to include the above published materials in my thesis. I certify that the above material describes work completed during my registration as a graduate student at the University of Windsor.

I declare that to the best of my knowledge, my thesis does not infringe upon anyone's copyright nor violate any proprietary rights and that any ideas, techniques, quotations, or any other material from the work of other people included in my thesis, published or otherwise, are fully acknowledged in accordance with the standard referencing practices. Furthermore, to the extent that I have included copyrighted material that surpasses the bounds of fair dealing within the meaning of the Canada Copyright Act, I certify that I have obtained written permission from the copyright owners to include such material(s) in my thesis.

I declare that this is a true copy of my thesis, including any final revisions, as approved by my thesis committee and the Graduate Studies office, and that this thesis has not been submitted for a higher degree to any other University or Institution.

## Abstract

This thesis uses numerical investigations to examine details of the turbulent flow past bluff bodies, in particular around various inclined flat plate configurations. The study consists of three phases: (1) flow past an infinitely long inclined flat plate, (2) flow past a finite length inclined flat plate near a wall and (3) flow past a stand-alone solar panel with support structure.

In Phase 1, the development of three-dimensional fluid structures around an infinitely long inclined flat plate at Reynolds number of  $1.57 \times 10^5$  is reported. The Detached Eddy Simulation (DES) is validated against well-established experimental data. The flow analysis in two-dimensional planes provides fundamental information about the spanwise and streamwise vortices that develop near the body and in its wake, but offers limited information on the formation and evolution of these vortices. Using the  $\lambda_2$ -criterion to visualize the three-dimensional fluid structures, the interaction between the spanwise and streamwise vortical structures and the shear layers is discussed. It is found that the spanwise wavelength of the streamwise vortical structures lie in the range corresponding to the mode B instability reported in previous studies of wake transition.

The effect of a wall on the flow structures around a finite length inclined flat plate at two proximities from the wall is investigated in Phase 2. In the mean analysis, it is found that the small clearance produces a wall-jet like flow in the gap which elongates the wake region, whereas a strong upwash is captured for the larger gap, reducing the length of the wake. Transient three-dimensional flow structures are captured using the  $\lambda_2$ -criterion. The early stage development of the flow around the plate shows inverted hairpin-like vortices

that generate a counter-rotating sheared vortex and a pair of vertical vortex tubes extending from the wall. This pair of vortex tubes is considered as the source of the meandering structures reported in the literature. At the later flow development stage, an asymmetric distorted flow for the smaller gap is observed, whereas there is a nearly symmetric wake pattern for the larger gap.

Numerical investigation of flow past a stand-alone solar panel with a supporting post is conducted using DES in Phase 3. Two elevations of the solar panel are examined. Mean velocity profiles and two-dimensional mean vorticity contours do not illustrate significant changes in the flow patterns, except for relatively weak vortices that develop along the post. The transient three-dimensional analysis using the  $\lambda_2$ -criterion captures four unique fluid structures around the body for the small gap case. On the other hand, the large gap case shows minimum influence from the post except for ligaments of vortex tubes that extend from the post. The same vortex structures also develop in the small gap case but are merged into the large scale vortices in the wake.



## **Dedication**

To all my family

## Acknowledgements

My thanks go to my advisors, Dr. Balachandar and Dr. Barron, for their support and guidance throughout my studies in graduate school. Especially, I would like to express thanks for their patience for the project conducted parallel to the work presented in this thesis. It would not have been successful without their support to complete those works. I appreciate my committee members, Dr. R. Carriveau, Dr. O. Iqbal, Dr. G. Rankin, Dr. B. Zhou, and especially Dr. E. Savory for their valuable time going through my work. I would also like to thank Dr. V. Roussinova for her involvement in many other aspects for my study.

I would like to thank all my fellow colleagues throughout my studies in graduate school: Sudharsan Annur Balasubramanian, Mohammadali Esmailzadi, Ravinder Gill, Mehdi Heidari, Vimaldoss Jesudhas, Jean-Paul Martins, Ghassan Nasif and Mehrdad Shademan have helped me in discussions in subjects of thermo-fluids, numerical modeling and post-processing. Also, thanks to Junting Chen, Sachin Sharma, Kharuna Ramrukheea, David Jarrod Hill, Matheson West, Priscilla Williams and Peng Wu for sharing their moments during my study.

I would like to extend my thanks to all faculty and staff members of the Department of Mechanical, Automotive and Materials Engineering and Faculty of Graduate Studies, and not to forget all my friends for their help.

This work was made possible by the facilities of the Shared Hierarchical Academic Research Computing Network (SHARCNET) and Compute/Calcul Canada.

## Table of Contents

Declaration of Co-Authorship / Previous Publication .....	iii
Abstract .....	vi
Dedication .....	viii
Acknowledgements .....	ix
List of Tables .....	xiii
List of Figures .....	xiv
List of Abbreviations, Symbols, Nomenclature .....	xix
Chapter 1. Introduction .....	1
Chapter 2. Numerical modeling .....	5
2.1. Turbulence model .....	5
2.2. Visualization methods .....	10
Chapter 3. Turbulent flow past an infinitely long inclined flat plate .....	13
3.1. Introduction .....	13
3.2. Methodology: Geometry and numerical setup .....	18
3.3. Validation: Pressure distribution along the inclined plate and shedding frequency .....	21
3.4. Analysis and discussion: Flow visualizations .....	23
3.4.1. Two-dimensional flow visualization .....	23

3.4.2.	Three-dimensional flow visualization.....	28
3.5.	Conclusions .....	39
Chapter 4.	Analysis of flow structures around an inclined plate near a wall .....	41
4.1.	Introduction .....	41
4.2.	Methodology .....	46
4.2.1.	Geometry setup .....	46
4.2.2.	Governing equations .....	49
4.3.	Mean flow analysis.....	50
4.4.	Transient flow structure analysis.....	65
4.4.1.	Transient flow analysis on the central plane.....	65
4.4.2.	Three-dimensional transient flow analysis .....	68
4.4.2.1.	Early stage flow development .....	68
4.4.2.2.	Steady state condition in the mean .....	74
4.5.	Conclusions .....	76
Chapter 5.	Analysis of flow structures around a stand-alone solar panel.....	78
5.1.	Introduction .....	78
5.2.	Methodology .....	80
5.2.1.	Geometry setup .....	80
5.2.2.	Governing equations .....	82
5.3.	Mean flow analysis.....	82

5.4. Three-dimensional transient flow analysis.....	95
5.4.1. Early stage flow development.....	95
5.4.2. Steady state condition in the mean.....	101
5.5. Conclusions .....	104
Chapter 6. Conclusions and recommendations.....	106
6.1. Conclusions .....	106
6.2. Recommendations .....	110
References.....	112
Vita Auctoris.....	121

## List of Tables

Table 3.1: Summary of spanwise instability modes in wake transition.....	17
--------------------------------------------------------------------------	----

## List of Figures

Figure 1.1: Examples of solar panels installed in a solar farm (adapted from The Globe and Mail) and in a rural area .....	1
Figure 3.1: Schematic of streamwise vortex formation along a shear layer braid in mode B instability with sectional view in section AA (adopted from Williamson [26]) .....	14
Figure 3.2: Schematic of computational domain .....	19
Figure 3.3: The distribution of pressure coefficient along the inclined plate .....	22
Figure 3.4: Instantaneous velocity vectors superimposed on the spanwise vorticity contours during a complete shedding period (T) .....	24
Figure 3.5: Instantaneous velocity vectors superimposed on streamwise vorticity contours on the transverse cross-section at $X/b = 1.0$ downstream from the centre of the inclined plate over a full shedding period (T). The contour lines of spanwise vorticity of $\pm 10 \text{ s}^{-1}$ are shown as a solid line for counter-clockwise and as a dashed line for clockwise rotation. ....	26
Figure 3.6: Instantaneous velocity vectors superimposed on streamwise vorticity contours on the transverse cross-section at $X/b = 3.0$ downstream from the centre of the inclined plate over a full shedding period (T). The contour lines of spanwise vorticity of $\pm 10 \text{ s}^{-1}$ are shown as a solid line for counter-clockwise and as a dashed line for clockwise rotation. ....	27
Figure 3.7: Instantaneous three-dimensional flow structures using the iso-surface of $\lambda_2/\lambda_{2\min} = 0.01$ coloured with the spanwise vorticity contours viewed from a) isometric, b)	

top, c) side and d) bottom, at time  $T/6$ . The arrow indicates direction of approaching flow: (1) shear layer, (2) streamwise vortices (ribs), (CR) clockwise rotating spanwise vortex, (CCR) counter-clockwise rotating spanwise vortex. .... 29

Figure 3.8: Instantaneous flow structures using the iso-surface of  $\lambda_2/\lambda_{2min} = 0.01$  coloured with the streamwise vorticity contours, viewed from the top at time a)  $3T/6$  and b)  $9T/6$ . ..... 30

Figure 3.9: Instantaneous flow structures using the iso-surface of  $\lambda_2/\lambda_{2min} = 0.01$  coloured with the streamwise vorticity contours, in the isometric view of a) the trailing edge at time  $4T/6$ , and b) the leading edge at time  $T/6$ . ..... 31

Figure 3.10: Vortical structure development in sequence in the near wake region using the iso-surface of  $\lambda_2/\lambda_{2min} = 0.01$  coloured with streamwise vorticity contours, viewed from the side at times  $6T/8$ ,  $7T/8$  and  $8T/8$ . The iso-surface is clipped at  $Z/b = -2.3$  from the midspan of the plate to produce a clear view of the flow structures. .... 33

Figure 3.11: Instantaneous velocity vectors superimposed on streamwise vorticity contours on the transverse cross-section at the a) leading edge ( $X/b = -0.322$ ), b) centre of the plate ( $X/b = 0.0$ ) and c) trailing edge ( $X/b = 0.322$ ) at  $T/6$  of a shedding period. The contour lines of transverse vorticity are at levels  $\pm 100 \text{ s}^{-1}$ , where a solid line corresponds to the positive (counter-clockwise) value and a dashed line represents the negative (clockwise) value. .... 35

Figure 3.12: New coordinate system with axes parallel ( $X_{alt}$ ) and normal ( $Y_{alt}$ ) to the inclined plate, and locations of planes normal to the plate used in Figure 3.13 and 3.14. 36



Figure 3.13: Instantaneous velocity vectors superimposed on $X_{alt}$ -vorticity contours on the cross-section normal to the plate near the leading edge ( $X_{alt}/b = -0.45$ ) over the shedding period (T). Solid lines near $Y_{alt}/b = 0.0$ represent the cut section of the inclined plate.....	37
Figure 3.14: Instantaneous velocity vectors superimposed on $X_{alt}$ -vorticity contours on the cross-section normal to the plate near the trailing edge ( $X_{alt}/b = 0.45$ ) over the shedding period (T). Solid lines near $Y_{alt}/b = 0.0$ represent the cut section of the inclined plate.....	38
Figure 4.1: Dimensions of calculation domain, a) side view and b) view from the inlet .	47
Figure 4.2: Velocity (— — —) and turbulence intensity (- - -) profiles at the inlet boundary .....	48
Figure 4.3: Velocity profiles at locations $X/\Delta = 0.5, 1.5, 2.5$ and $3.5$ . a) streamwise; b) depthwise; c) spanwise velocity.....	52
Figure 4.4: Mean velocity flow streamtraces on the central plane, superimposed with mean pressure (Pa) contours ( $H/\Delta=0.22$ and $H/\Delta=1.11$ ).....	57
Figure 4.5: Streamtraces superimposed with X-vorticity contours on YZ planes at $X/\Delta=0.5, 1.5, 2.5$ and $3.5$ for $H/\Delta=0.22$ (left) and $H/\Delta=1.11$ (right).....	59
Figure 4.6: Definitions of axes and section planes parallel and normal to the inclined plate.....	60
Figure 4.7: Streamtraces and vorticity contours on planes parallel to inclined plate for $H/\Delta=0.22$ (left) and $H/\Delta=1.11$ (right).....	62

Figure 4.8: Streamtraces and vorticity contours on planes normal to inclined plate for $H/\Delta=0.22$ (left) and $H/\Delta=1.11$ (right).....	64
Figure 4.9: Instantaneous velocity vector field superimposed with Z-vorticity at early flow development stage: (a-c) $H/\Delta = 0.22$ , and (d-f) $H/\Delta = 1.11$ .....	67
Figure 4.10: Identification of flow structures around the inclined plate with $H/\Delta = 0.22$ gap after 0.16 s: (1) hairpin-like vortex, (2) inverted hairpin-like vortex developed at the leading edge, (3) a pair of vortices extending from the wall, and (4) corner vortices .....	69
Figure 4.11: Early stage flow structures development around the inclined plate for $H/\Delta = 0.22$ (left) and $H/\Delta = 1.11$ (right).....	72
Figure 4.12: Iso-surfaces of $\lambda_2$ at $t = 1.55$ s for $H/\Delta = 0.22$ , with the contours of X-vorticity on the surfaces .....	73
Figure 4.13: Iso-view of the iso-surfaces of $\lambda_2$ with the contours of Y-vorticity on the left, and a bottom view of the same structures with the filtering plane set at $Y/\Delta = 0.22$ on the right ( $H/\Delta = 0.22$ ) .....	74
Figure 4.14: Iso-surfaces of $\lambda_2$ at $t = 5.60$ s with the contours of Y-vorticity on these surfaces for $H/\Delta=0.22$ (left) and $H/\Delta=1.11$ (right) .....	75
Figure 4.15: Bottom view of iso-surfaces of $\lambda_2$ with Y-vorticity contours on its surfaces (left) and the same view of Y-vorticity contours on XZ plane at $Y/\Delta = 0.05$ (right) after $t = 5.60$ s in the $H/\Delta=0.22$ gap case .....	75
Figure 5.1: Dimensions of calculation domain, a) side view and b) view from the inlet.	81
Figure 5.2: Velocity profiles at locations $X/\Delta = 0.5, 1.5, 2.5$ and $3.5$ , a) streamwise; b) depthwise; c) spanwise velocity, for $H/\Delta = 0.22$ .....	86

Figure 5.3: Velocity profiles at locations $X/\Delta = 0.5, 1.5, 2.5$ and $3.5$ , a) streamwise; b) depthwise; c) spanwise velocity, for $H/\Delta = 1.11$ .....	87
Figure 5.4: Velocity profiles at locations $X/\Delta = 0.0, 0.4D, 0.6D$ and $1.0$ , a) streamwise; b) depthwise; c) spanwise velocity, for $H/\Delta = 0.22$ and $1.11$ .....	89
Figure 5.5: Mean velocity flow streamtraces on the central plane, superimposed with mean pressure (Pa) contours for a) $H/\Delta = 0.22$ with post, b) $H/\Delta = 0.22$ without post, c) $H/\Delta = 1.11$ with post and d) $H/\Delta = 1.11$ without post .....	90
Figure 5.6: Streamtraces superimposed with X-vorticity contours on YZ planes at $X/\Delta = 0.5, 1.5, 2.5$ and $3.5$ for $H/\Delta = 0.22$ with post (left) and $H/\Delta = 0.22$ without post (right)	92
Figure 5.7: Streamtraces superimposed with X-vorticity contours on YZ planes at $X/\Delta = 0.5, 1.5, 2.5$ and $3.5$ for $H/\Delta = 1.11$ with post (left) and $H/\Delta = 1.11$ without post (right)	94
Figure 5.8: Early stage development of flow structures around the inclined plate for $H/\Delta = 0.22$ with post (left) and without post (right).....	97
Figure 5.9: Early stage development of flow structures around the inclined plate for $H/\Delta = 1.11$ with post (left) and without post (right).....	99
Figure 5.10: Bottom view of the same structures with the filtering plane set at $Y/\Delta = 0.22$ for $H/\Delta = 0.22$ with post (left) and without post (right) .....	101
Figure 5.11: Iso-surfaces of $\lambda_2$ at $t = 5.60$ s with colour contours of Y-vorticity on these surfaces for $H/\Delta=0.22$ (left) and $H/\Delta=1.11$ (right) .....	103

## List of Abbreviations, Symbols, Nomenclature

b	width of the inclined plate, [m]
$C_{des}$	calibration constant
$C_p$	pressure coefficient; $(p - p_0)/\frac{1}{2}\rho U_0^2$
CFD	Computational Fluid Dynamics
CFL	Courant-Friedrichs-Lewy
CR	clockwise rotation
CCR	counter-clockwise rotation
D	cylinder diameter, [m]
DDES	delayed Detached Eddy Simulations
DES	Detached Eddy Simulation
DNS	Direct Numerical Simulation
d	wall distance, [m]
$\tilde{d}$	DES length scale, [m]
$F_1, F_2$	blending factors
FFT	Fast Fourier Transformation
$F(M_t)$	compressibility function
f	shedding frequency, [Hz]
$G_k, G_\omega$	production terms of turbulent kinetic energy and specific dissipation rate
H	gap height, [m]
k	turbulent kinetic energy, [m <sup>2</sup> /s <sup>2</sup> ]

L	length of the inclined plate, [m]
$L_t$	turbulent length scale, [m]
LES	Large Eddy Simulation
p	pressure, [Pa]
$p_0$	reference pressure, [Pa]
QP	quasi-periodic
R	streamwise vortices (ribs)
RANS	Reynolds-Averaged Navier-Stokes
Re	Reynolds number; $(U_0 \cdot b)/\nu$
$Re_t$	Turbulent Reynolds number; $k/(\nu\omega)$
RT	reflection-transition
$S_{ij}$	shear strain tensor; $\frac{1}{2}(U_{i,j} + U_{j,i})$ , [ $s^{-1}$ ]
St	Strouhal number; $(f \cdot b)/U_0$
SIMPLE	Semi-Implicit Method for Pressure Linked Equations
SST	Shear-Stress Transport
t	time, [s]
T	shedding period, [s]
$U_i$ , or	instantaneous velocity components; $\bar{U}_1 + u'_i$ , [m/s]
U, V, W	
$U(y)$	streamwise velocity at distance y from the bottom wall, [m/s]
$U_g$	geostrophic wind velocity, [m/s]
$U_{i,j}$	velocity gradients, [ $s^{-1}$ ]
$U_0$	reference approaching velocity, [m/s]

$u_\tau$	friction velocity, [m/s]
$X_i$ , or	Cartesian coordinate directions, [m]
$X, Y, Z$	
$X_{Alt}, Y_{Alt}$	parallel and perpendicular axes to the inclined plate, [m]
$Y_k, Y_\omega$	dissipation terms of turbulent kinetic energy and specific dissipation rate
$Y^*$	normal direction normalized by $H$ for the gap region and $\Delta$ for the upper region
$y_g$	atmospheric boundary layer height in an open terrain, [m]
$y^+$	wall normal distance; $(u_\tau \cdot y)/\nu$
$\alpha$	constant exponent based on terrain type
$\alpha^*$	coefficient of low Reynolds number correction
$\Delta$	projected height of the inclined plate; $b \cdot \sin(\pi - \phi)$ , [m]
$\Delta_{max}$	maximum grid spacing in each coordinate direction, [m]
$\delta_{ij}$	Kronecker delta
$\kappa$	von Kármán constant; $\kappa = 0.41$
$\lambda$	eigenvalue
$\lambda_{min}$	global minimum eigenvalue
$\mu_t$	turbulent viscosity, [m <sup>2</sup> /s]
$\nu$	kinematic viscosity, [m <sup>2</sup> /s]
$\nu_t$	turbulent eddy viscosity, [m <sup>2</sup> /s]
$\rho$	air density, [kg/m <sup>3</sup> ]
$\sigma$	turbulent Prandtl number

$\tau_w$	wall shear stress, [Pa]
$\phi$	inclination angle of the plate, [deg]
$\Omega_{ij}$	rotation tensor; $\frac{1}{2}(U_{i,j} - U_{j,i})$ , [ $s^{-1}$ ]
$\omega$	specific dissipation rate, [ $s^{-1}$ ]

#### Symbols

—	time-averaged
'	fluctuation
$\nabla$	gradient operator

## Chapter 1. Introduction

Flow past bluff bodies is of interest in many disciplines of engineering ranging from aerospace to civil engineering. The characteristics of flow past bluff bodies have been studied extensively for the last few decades, primarily considering the drag, lift and vortex shedding phenomena. Recently, there has been a renewed interest in this area due to the proliferation in the use of solar panels.

Canada is one of the top ten countries in the world in terms of solar panel installations and Ontario is one of the largest contributors among the provinces/territories [1]. The industry continues to grow as evident in the ongoing project by Samsung Renewable Energy Inc., which is developing the solar farm at the Windsor International Airport. Solar panels are not only installed in large solar farms (Figure 1.1, left) but also on rooftops and as stand-alone structures (Figure 1.1, right). Solar panels are typically installed in an open terrain for maximum exposure to sunlight where, unfortunately, they will also be subjected to wind forces [2, 3].



Figure 1.1: Examples of solar panels installed in a solar farm (adapted from The Globe and Mail) and in a rural area



A number of studies have been conducted to evaluate the wind load on solar panels from the perspective of assessing conditions which could cause damage to the devices. In studies of a ground mounted solar array in a single row [4, 5], the first panel of the array facing towards the approaching flow direction was found to experience the largest wind load. A sheltering effect, identified by a reduction in force on the second and subsequent panels of the array, was noted. A similar observation was reported in experiments of wind loads on ground mounted multiple row solar panels tested in a boundary layer wind tunnel facility [6]. These studies also showed that the outer array panels were subjected to higher load compared to the inner panels. The above observations and the mean velocity and pressure contour plots presented in the works of Shademan et al. [4] and Jubayer and Hangan [5] indicate that in the case of a ground mounted solar array, the approaching flow has its greatest impact on the front panels of the array, whereas the panels in the downstream region behind the front row have lower wind loads. Research has also been conducted to investigate the wind loads on flat rooftop panels located in an array [7]. It was reported that a larger space between the array outer rows and the raised perimeter of the building could reduce the wind load on the array. Meanwhile, in the case of a flat rooftop solar array, Pratt and Kopp [8] suggested that the force acting on the panel was the result of either the suction due to the large separation bubble that formed above the array or the local flow reattachment around the array. Additionally, the wind loads on the flat rooftop solar array depended on the flow that developed around the building.

It is important to understand the nature of the forces generated due to the fluid-structure interaction and further investigation of the flow features will provide more insight into the physical mechanisms of the flow development. In order to study the flow

development around a bluff body, the single stand-alone solar panel geometry becomes an obvious first choice. Most previous studies mainly considered the time-averaged flow and discussed only the mean flow quantities [9, 10]. More recently, Shademan et al. [11] has numerically investigated the transient characteristics of the fluid structures generated by the flow and bluff body interaction. Especially, the study showed the significance of the wall proximity on the flow that developed around the bluff body and identified unique fluid structures that formed around the body using three-dimensional flow visualization techniques. Joint examination of one-dimensional quantitative analysis, and two- and three-dimensional qualitative flow analysis was found useful to understand the development of the flow around a bluff body.

The present study, which extends the work of Shademan et al. [11], is divided into three phases:

- 1) Flow past an inclined infinitely long flat plate
- 2) Flow past an inclined finite length (three-dimensional) flat plate
- 3) Flow past a ground mounted solar panel

In Phase 1, the flow past an inclined infinitely long flat plate is examined. Although this flow has been investigated experimentally and numerically for the last 100 years, the purpose of this phase is to explore the detailed fluid structures in the wake and to enhance our understanding of the mechanisms that generate these structures. This study is conducted using three-dimensional computational fluid dynamics (CFD) simulations. The validation of the numerical setup, including boundary conditions and turbulence model, is performed for a well-known classical flow over an inclined infinitely long plate in a

freestream (Fage and Johansen [12]). Chapter 3 of this thesis deals with Phase 1 of the study.

In Phase 2, a finite length inclined three-dimensional bluff body is set near a wall. This phase focuses on the effect of the gap ( $H = 0.5$  and  $2.5$  m) between the wall and the bluff body. The flow field is analyzed in two stages: (1) early development stage and (2) steady state condition in the mean. Phase 2 of the research is discussed in Chapter 4 of the thesis.

Phase 3 deals with the numerical simulation of the flow around a realistic ground mounted solar panel. Building on the knowledge acquired from Phase 2, a vertical circular cylinder supporting the solar panel is incorporated in the geometry. Again, two different heights of the plate from the ground are examined under the same conditions as in Phase 2. New structures that form due to the interactions of the bed, the support and the panel are identified and discussed. This phase is addressed in Chapter 5.

The conclusions of the thesis are summarized in Chapter 6. Since each chapter contains a separate review of the literature relevant to the problem being addressed, a detailed discussion of the literature is not included here.

## **Chapter 2. Numerical modeling**

The unsteady incompressible Navier-Stokes equations are solved using a finite volume formulation in all three phases of this study. The same turbulence model and flow visualization method have been used for all problems considered. In this chapter, detailed definitions related to the selected turbulence model and visualization method are reviewed. Specific details of the numerics are also presented in each chapter. Throughout this dissertation, ANSYS Fluent 15.0 is used to conduct the computational fluid dynamics simulations.

### **2.1. Turbulence model**

An important objective of this study is to capture the flow developing around the bluff body. To accurately predict the nature of turbulence, the selection of a turbulence model is critical. Reynolds-Averaged Navier-Stokes (RANS) two-equation turbulence models, such as the family of  $k$ - $\epsilon$  and  $k$ - $\omega$  models, are especially popular in industry for their lower computational cost [13]. These models are governed by ensemble-averaged continuity and momentum equations while the turbulence kinetic energy and dissipation rate are modeled assuming the turbulence is isotropic. Large Eddy Simulation (LES), on the other hand, solves the full Navier-Stokes equations in the domain where large eddies are present, whereas a model is applied in the regions of the computational domain where small eddies are dominant [14]. Like RANS models, LES still requires careful meshing in the wall region but further grid refinement in all directions is necessary for filtering in LES; thus, LES is computationally expensive. Taking advantage of both RANS and LES turbulence models, a hybrid turbulence model was proposed by Spalart [15]. Detached

Eddy Simulation (DES) is a hybrid of LES and RANS, where the near wall flow is modeled using RANS which is well-suited to model the isotropic turbulence of small scale eddies. Although various RANS turbulence models are available as an option for DES in commercial CFD software, the SST  $k-\omega$  model [16] is selected in the current study. The SST  $k-\omega$  model is preferred since the turbulence model is tuned such that the thin boundary layer, which develops along the bluff body, can be well predicted [17]. The activation of the RANS mode in DES is determined when the DES length scale  $\tilde{d}$  is equal to the wall distance ( $d$ ) from the local cells. The LES mode is turned on if the length scale reaches the value of  $C_{des}\Delta_{max}$  where  $C_{des}$  is a calibration constant and  $\Delta_{max}$  is the maximum grid spacing in each coordinate system. In order to maintain the RANS mode active within the thicker boundary layer region relative to the small  $\Delta_{max}$  detected in the region, an alternative definition of the DES length scale is needed. A delayed DES (DDES), one of options for DES, calculates the DES length scale as

$$\tilde{d} = d - f_d \max[0, d - C_{des}\Delta_{max}] \quad (1)$$

$$f_d = 1 - \tanh[(8r_d)^3] \quad (2)$$

$$r_d = \frac{v_t + \nu}{\sqrt{U_{i,j}U_{i,j}}\kappa^2 d^2} \quad (3)$$

where  $v_t$  is the kinematic eddy viscosity,  $U_{i,j}$  are the velocity gradients and  $\kappa$  is the von Kármán constant specified as 0.41 [18].

The instantaneous continuity and momentum equations, presented below, are solved in the LES region:

$$\frac{\partial \rho}{\partial t} + \frac{\partial}{\partial X_i} (\rho U_i) = 0 \quad (4)$$

$$\begin{aligned} \frac{\partial}{\partial t} (\rho U_i) + \frac{\partial}{\partial X_j} (\rho U_i U_j) \\ = -\frac{\partial p}{\partial X_i} + \frac{\partial}{\partial X_j} \left[ \mu \left( \frac{\partial U_i}{\partial X_j} + \frac{\partial U_j}{\partial X_i} - \frac{2}{3} \delta_{ij} \frac{\partial U_i}{\partial X_j} \right) \right] + \frac{\partial}{\partial X_j} (-\rho \overline{u_i' u_j'}) \end{aligned} \quad (5)$$

where  $\delta_{ij}$  is the Kronecker delta. On the other hand, for unsteady RANS the ensemble-averaged Navier-Stokes equations are solved, written in the form,

$$\frac{\partial \rho}{\partial t} + \frac{\partial}{\partial X_i} (\rho \bar{U}_i) = 0 \quad (6)$$

$$\begin{aligned} \frac{\partial}{\partial t} (\rho \bar{U}_i) + \frac{\partial}{\partial X_j} (\rho \bar{U}_i \bar{U}_j) \\ = -\frac{\partial p}{\partial X_i} + \frac{\partial}{\partial X_j} \left[ \mu \left( \frac{\partial \bar{U}_i}{\partial X_j} + \frac{\partial \bar{U}_j}{\partial X_i} - \frac{2}{3} \delta_{ij} \frac{\partial \bar{U}_i}{\partial X_j} \right) \right] + \frac{\partial}{\partial X_j} (-\rho \overline{u_i' u_j'}) \end{aligned} \quad (7)$$

where overbar indicates the mean velocity. The Reynolds stresses,  $-\rho \overline{u_i' u_j'}$ , are required to be modeled to close the momentum equations.

Transport equations of the SST  $k$ - $\omega$  model, without source terms, are given as [19]

$$\frac{\partial}{\partial t} (\rho k) + \frac{\partial}{\partial X_i} (\rho k \bar{U}_i) = \frac{\partial}{\partial X_j} \left[ \left( \rho \nu + \frac{\mu_t}{\sigma_k} \right) \frac{\partial k}{\partial X_j} \right] + G_k - Y_k \quad (8)$$

$$\frac{\partial}{\partial t} (\rho \omega) + \frac{\partial}{\partial X_i} (\rho \omega \bar{U}_i) = \frac{\partial}{\partial X_j} \left[ \left( \rho \nu + \frac{\mu_t}{\sigma_\omega} \right) \frac{\partial \omega}{\partial X_j} \right] + G_\omega - Y_\omega \quad (9)$$

where  $G$  and  $Y$  with subscripts of  $k$  and  $\omega$  are the production and dissipation terms of turbulence kinetic energy ( $k$ ) and specific dissipation rate ( $\omega$ ), respectively. The turbulent viscosity,  $\mu_t$ , is defined as

$$\mu_t = \frac{\rho k}{\omega} \frac{1}{\max\left[\frac{1}{\alpha^*}, \frac{SF_2}{a_1 \omega}\right]} \quad (10)$$

and the turbulent Prandtl numbers of  $k$  and  $\omega$  are given by

$$\sigma_k = \frac{1}{F_1/\sigma_{k,1} + (1 - F_1)/\sigma_{k,2}} \quad (11)$$

$$\sigma_\omega = \frac{1}{F_1/\sigma_{\omega,1} + (1 - F_1)/\sigma_{\omega,2}}. \quad (12)$$

In these equations,  $S$  is the strain rate magnitude and other constants are specified as  $a_1 = 0.31$ ,  $\sigma_{k,1} = 1.176$ ,  $\sigma_{k,2} = 1.0$ ,  $\sigma_{\omega,1} = 2.0$ , and  $\sigma_{\omega,2} = 1.168$ . The coefficient of low Reynolds number correction to damp the turbulent viscosity is given by

$$\alpha^* = \alpha_\infty^* \left( \frac{\alpha_0^* + Re_t/R_k}{1 + Re_t/R_k} \right) \quad (13)$$

where  $R_k = 6.0$ ,  $\alpha_\infty^* = 1.0$  and the rest of parameters can be obtained from

$$Re_t = \frac{k}{\nu \omega} \quad (14)$$

$$\alpha_0^* = \frac{\beta_i}{3} \quad (15)$$

$$\beta_i = 0.072. \quad (16)$$

The blending functions,  $F_1$  and  $F_2$ , are defined as

$$F_1 = \tanh(\Phi_1^4) \quad (17)$$

$$F_2 = \tanh(\Phi_2^2) \quad (18)$$

$$\Phi_1 = \min \left[ \max \left( \frac{\sqrt{k}}{0.09 \omega y}, \frac{500 \nu}{y^2 \omega} \right), \frac{4 \rho k}{\sigma_{\omega,2} D_\omega^+ y^2} \right] \quad (19)$$

$$D_{\omega}^+ = \max \left[ \frac{2\rho}{\sigma_{\omega,2}} \frac{\partial k}{\omega} \frac{\partial \omega}{\partial x_j}, 10^{-10} \right] \quad (20)$$

$$\Phi_2 = \max \left[ 2 \frac{\sqrt{k}}{0.09\omega y}, \frac{500\nu}{y^2\omega} \right] \quad (21)$$

where  $y$  is the distance to the nearest boundary. The terms representing production of  $k$  and  $\omega$  are calculated using

$$G_k = -\rho \overline{u_i' u_j'} \frac{\partial \bar{U}_j}{\partial X_i} \quad (22)$$

$$G_{\omega} = \frac{\alpha}{\nu_t} G_k \quad (23)$$

$$\alpha = \frac{\alpha_{\infty}}{\alpha^*} \left( \frac{\alpha_0 + Re_t/R_{\omega}}{1 + Re_t/R_{\omega}} \right) \quad (24)$$

$$\alpha_{\infty} = F_1 \alpha_{\infty,1} + (1 - F_1) \alpha_{\infty,2} \quad (25)$$

$$\alpha_{\infty,1} = \frac{\beta_{i,1}}{\beta_{\infty}^*} - \frac{\kappa^2}{\sigma_{\omega,1} \sqrt{\beta_{\infty}^*}} \quad (26)$$

$$\alpha_{\infty,2} = \frac{\beta_{i,2}}{\beta_{\infty}^*} - \frac{\kappa^2}{\sigma_{\omega,2} \sqrt{\beta_{\infty}^*}} \quad (27)$$

where constants are  $\alpha_0 = 1/9$ ,  $R_{\omega} = 2.95\alpha^*$ ,  $\beta_{i,1} = 0.075$ ,  $\beta_{i,2} = 0.0828$ ,  $\beta_{\infty}^* = 0.09$ , and again  $\kappa = 0.41$ .

Similarly, the terms representing dissipation of  $k$  and  $\omega$  are obtained by

$$Y_k = \rho \beta^* k \omega F_{DES} \quad (28)$$

$$Y_{\omega} = \rho \beta_i \omega^2 \quad (29)$$

where  $\beta^*$  and  $\beta_i$  is computed from



$$\beta^* = \beta_i^*[1 + 1.5F(M_t)] \quad (30)$$

$$\beta_i^* = 0.09 \left[ \frac{\frac{4}{15} + \left(\frac{Re_t}{8}\right)^4}{1 + \left(\frac{Re_t}{8}\right)^4} \right] \quad (31)$$

$$\beta_i = F_1\beta_{i,1} + (1 - F_1)\beta_{i,2}. \quad (32)$$

$F(M_t)$  is the compressibility function, defined as:

$$F(M_t) = \begin{cases} 0 & \sqrt{\frac{2k}{\gamma RT}} \leq 0.25 \\ \frac{2k}{\gamma RT} - (0.25)^2 & \sqrt{\frac{2k}{\gamma RT}} > 0.25 \end{cases}. \quad (33)$$

For DES the dissipation of  $k$ ,  $Y_k$ , is modified from the original SST  $k$ - $\omega$  model with an added  $F_{DES}$  term to the equation, where

$$F_{DES} = \max \left[ \frac{L_t}{C_{des}\Delta_{max}}(1 - F_{SST}), 1 \right] \quad (34)$$

and the turbulent length scale,  $L_t$ , can be found from

$$L_t = \frac{\sqrt{k}}{\beta^*\omega} \quad (35)$$

where  $C_{des} = 0.61$  which is a calibration constant,  $\Delta_{max}$  is the maximum local grid spacing along the coordinate direction, and  $F_{SST}$  is the blending function of the SST model which can be either zero,  $F_1$  or  $F_2$ .

## 2.2. Visualization methods

To analyze the flow structures as the flow develops around a bluff body, a two-dimensional sectional plane is usually generated in the field of interest. However, the three-dimensional fluid structures that develop around the bluff body are cut by the 2-D

plane, making it difficult to picture the overall shape of the structures. Several options are available to capture the three-dimensional fluid structures using the iso-surface of fluid characteristics: pressure, vorticity magnitude, etc. [20]. It is common practice to identify the fluid structures using the vortex core identification methods such as Q-criterion,  $\Delta$ -criterion and  $\lambda_2$ -criterion. The Q-criterion, developed by Hunt et al. [21], identifies a vortex as a region where the second invariant of the velocity gradient tensor, Q, is positive. The second invariant of  $\nabla U_i$  is defined as:

$$Q = \frac{1}{2} (\|\Omega_{ij}\|^2 - \|S_{ij}\|^2) \quad (36)$$

where

$$S_{ij} = \frac{1}{2} (U_{i,j} + U_{j,i}) \quad (37)$$

$$\Omega_{ij} = \frac{1}{2} (U_{i,j} - U_{j,i}). \quad (38)$$

The positive second invariant indicates the region of excess rotation rate ( $\|\Omega_{ij}\|$ ) over the strain rate ( $\|S_{ij}\|$ ).

The  $\Delta$ -criterion, defined by Chong et al. [22], determines a vortex as a region where the velocity gradient tensor,  $\nabla U_i$ , has complex eigenvalues. This criterion considers the complex eigenvalues to show the region where the streamlines are closed or form a spiral pattern. The eigenvalues of  $\nabla U_i$  in the local flow field are found from the equation:

$$\lambda^3 + P\lambda^2 + Q\lambda + R = 0 \quad (39)$$

where P, Q and R are invariants of  $\nabla U_i$  (first, second and third invariants, respectively) which are defined as:

$$P = -\nabla \cdot U_i \quad (40)$$

$$R = -\det(\nabla U_i) \quad (41)$$

and where the second invariant,  $Q$ , is shown in equation (36). The condition to have complex eigenvalues for incompressible flow, where  $P = 0$ , is given by:

$$\Delta = \left(\frac{1}{2}R\right)^2 + \left(\frac{1}{3}Q\right)^3 > 0. \quad (42)$$

The  $\lambda_2$ -criterion, defined by Jeong and Hussain [23], takes the two negative eigenvalues of the pressure Hessian to identify the vortex core. The eigenvalues of the pressure Hessian were derived by first taking the gradient of the Navier-Stokes equations.

$$\frac{DS_{ij}}{Dt} - \nu S_{ij,kk} + S_{ik}S_{kj} + \Omega_{ik}\Omega_{kj} = -\frac{1}{\rho}p_{,ij} \quad (43)$$

The unsteady irrotational straining and the viscous effects, the first and second terms in equation (43), are dropped for simplification, giving

$$S_{ik}S_{kj} + \Omega_{ik}\Omega_{kj} = -\frac{1}{\rho}p_{,ij} \quad (44)$$

The second eigenvalue of equation (44),  $\lambda_2$ , where  $\lambda_1 \geq \lambda_2 \geq \lambda_3$ , should be negative in the core of the vortex.

$Q$ -criterion and  $\Delta$ -criterion consider the excess rotational motion over shear strain as determination of a vortex, while the pressure minima are not involved in identification of the vortex. Since the  $\lambda_2$ -criterion takes pressure minima due to the vortical motion, it is considered preferable for vortex core identification [20, 23]. Therefore, the  $\lambda_2$ -criterion was chosen to illustrate the three-dimensional vortical structures around the bluff bodies in this work.

## **Chapter 3. Turbulent flow past an infinitely long inclined flat plate**

### **3.1. Introduction**

The flow past an infinitely long inclined flat plate, a classic problem in bluff body aerodynamics, is typically considered as a two-dimensional problem. The applications of such a study can be extended to flow past an airfoil, a large solar panel, and many other mechanical systems. The von Kármán vortex street is a major flow structure expected in the wake of the bluff body. In the study of flow past an infinitely long circular cylinder, Roshko [24] identified three regimes based on the stable and irregular velocity fluctuations, and transition between stable and irregular fluctuations. Further experimental and numerical investigations in the transition regime by Williamson [25] indicated the occurrence of three-dimensional flow features. The critical Reynolds number of the wake transition was determined to be around  $Re = 180$  by Williamson [26] in the study of flow past a circular cylinder. The flow was categorised into two modes; mode A and mode B. The mechanism of the mode A instability was due to the vortex dislocation of the primary vortex core. The primary vortex core deforms in the spanwise direction, stretches towards the bluff body and influences the next vortex core. The mode B instability was a result of streamwise vortex pairs (streamwise vortices in Figure 3.1) formed from the primary shedding vortex (primary vortex A in Figure 3.1) and residing close to a developing braid (braid shear layer B in Figure 3.1) which gets perturbed by the pairs. The mode A instability has large spanwise wavelength ( $\approx 4D$ ) due to a primary vortex core instability, whereas the instability of mode B has small spanwise wavelength

( $\approx 1D$ ) along the braid. Zhang et al. [27] defined a new three-dimensional instability, namely mode C, with a spanwise wavelength of about  $1.8D$  and wider spacing of the von Kármán vortices in the streamwise direction compared to modes A and B were observed.

A three-dimensional fluid structures analysis using Direct Numerical Simulation (DNS) was presented by Mittal and Balachandar [28]. Their work considered the flow at  $Re = 525$  based on the diameter of the cylinder. The flow structures visualized using the  $\lambda_2$ -criterion showed the generation of streamwise vortical structures (ribs) around spanwise vortical structures (rollers) due to either a braid instability or a core instability. Spanwise distortion of the rollers (bulges and valleys) was observed close to the bluff body. Near the wake region, crescent shape structures were attached on the roller shedding from the body, developed into a horseshoe-like vortex and eventually became a hairpin-like vortex in the next sequence. Since this study used only one cylinder diameter for the spanwise width of the computational domain, it restricted any possible identification of the wake transition mode.

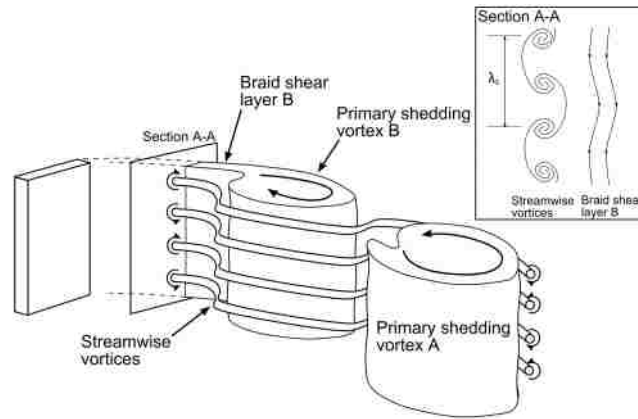


Figure 3.1: Schematic of streamwise vortex formation along a shear layer braid in mode B instability with sectional view in section AA (adopted from Williamson [26])

The above three-dimensional flow instability modes were also captured in the flow past an infinitely long square cylinder (Robichaux et al. [29]). In comparison with the flow past a circular cylinder, the spanwise wavelengths for mode A and B in the case of flow past a square cylinder were found to be shifted to 5.2D and 1.2D, respectively, in the range of  $150 < Re < 175$  for mode A and  $175 < Re < 205$  for mode B. Robichaux et al. [29] performed Floquet stability analysis and also found an intermediate three-dimensional instability called mode S. The spanwise wavelength of streamwise vortex structures was found to be 2.8D with Reynolds numbers in the range  $175 < Re < 205$ . Mode S showed a non-symmetric pattern in the space-time streamwise vorticity plots, whereas mode A and B presented odd and even reflection-transition (RT) symmetry about the wake centre line. Later, the mode was realized as a quasi-periodic mode (or mode QP) by Blackburn and Lopez [30].

The effect of the inclination of an infinitely long square cylinder suspended horizontally was examined numerically by Sheard et al. [31]. The range of inclination angles tested in the study was  $0 \leq \Phi \leq 45$  degree, and the characteristic length for Reynolds number and Strouhal number was the projected height of the inclined bluff body. The study demonstrated that the occurrence of the three-dimensional mode A instability first appeared for 0 to 12 degrees and then again above 26 degrees incidence angle, whereas for incidence angles between 12 and 26 degrees, mode C was observed. Once the Reynolds number of the flow was increased beyond the critical Reynolds number at any incidence angles, mode B instability occurred at around  $Re = 200$ . The spanwise wavelength was found to vary with incidence angles. The wavelength for the mode A

ranged from 4.8D to 5.8D while the mode C ranged from 2.0D to 2.4D, whereas the mode B had no significant change in wavelength ( $\approx 1.0D$ ).

The role of aspect ratio of an infinitely long rectangular object on three-dimensional instability was also observed by Choi and Yang [32]. The aspect ratio was defined as depth over height of the object. The study proposed new modes of instability for the flow past a normal thin flat plate (aspect ratio close to zero): modes A2 and QP2. Mode A2 had the spanwise wavelength of 2.0D and that of mode QP2 was found to be 5.0D for a thin flat plate, whereas the spanwise wavelength reduced to 1.0D for mode A2 while the wavelength of mode QP2 varied in the range of 4.8D to 5.8D when the aspect ratio was increased toward unity (square shape).

When the flow approaches the infinitely long thin flat plate at various incident angles, multiple spanwise wavelengths of streamwise vortical structures were observed simultaneously. Yang et al. [33] examined the three-dimensional wake transition behind an infinitely long inclined flat plate at 25 degrees incident angle, for Reynolds numbers varying from 275 to 800. From the instantaneous flow visualization using  $\lambda_2$ -criterion at  $Re = 325$ , two wavelengths of 0.5D and 0.8D were observed between the periodic structures in the spanwise direction. Using the probability density function (PDF) of the spanwise wavelength, three different spanwise wavelengths, 0.88D, 1.77D and 2.75D, were detected in the case of  $Re = 400$ , with 0.88D was the dominant wavelength. Once the Reynolds number was increased, the PDF showed that the two larger wavelengths (1.77D and 2.75D) were diminished and the major spanwise wavelength was around 1.0D. Further analysis was conducted for the inclination angles of 20, 25 and 30 degrees. As seen in the work of Sheard et al. [31], mode B was observed in this range of

inclination angles with the small spanwise wavelength (around 1.0D) as a first occurrence instability at critical Reynolds number above  $Re = 200$ . The mode QP coexisted at higher Reynolds number with the spanwise wavelength ranging from 2.0D to 3.5D for angles of 20 and 25 degrees, whereas the wavelength shifted to the range of 1.5D to 2.0D for the case of 30 degrees incident angle.

Table 3.1: Summary of spanwise instability modes in wake transition

Mode				
A	$Re < 260$ <b>4.0D</b>	$150 < Re < 175$ <b>5.2D</b>	$Re < 200$ $0^\circ < \alpha < 12^\circ, \alpha > 26^\circ$ <b>4.8 – 5.8D</b>	-
B	$Re > 260$ <b>1.0D</b>	$175 < Re < 205$ <b>1.2D</b>	$Re \geq 200$ <b>1.0D</b>	$275 < Re < 800$ $20^\circ < \alpha < 30^\circ$ <b>0.5 – 2.8D</b>
C	$170 < Re < 205$ <b>1.8D</b>	-	$Re < 200$ $12^\circ < \alpha < 26^\circ$ <b>2.0 – 2.4D</b>	-
QP (S)	-	$175 < Re < 205$ <b>2.8D</b>	-	$20^\circ < \alpha < 25^\circ$ <b>2.0 – 3.5D</b> $\alpha = 30^\circ$ <b>1.5 – 2.0D</b>

The above-mentioned studies were focused on the wake transition where the Reynolds numbers ranged from roughly  $150 < Re < 800$ . In this range, the shapes and orientations of bluff bodies influence the flow instabilities. However, the majority of engineering applications are operated in the turbulent flow regime; therefore, the mode B instability should be expected in the three-dimensional instability where the expected spanwise wavelength is around 1.0D. Numerical studies of flow past bluff bodies at high Reynolds number were conducted by Lloyd and James [34], Lysenko et al. [35], Narasimhamurthy and Andersson [36], Rajani et al. [37] and Tian et al. [38] using Large-Eddy Simulation (LES) and DNS. These studies visualized the fluid structures developed around the bluff body using the Q-criterion and  $\lambda_2$ -criterion; however, there was no further discussion



about the characteristics of the streamwise vortical structures of the flow at higher Reynolds numbers.

Even though the turbulence of the flow at high Reynolds number is complex, some similarities are observed in the three-dimensional fluid structures developed in the wake transition regime. The small scale streamwise vortical structures, which develop around the large scale fluid structures, do not have a major impact on forces acting on the bodies but can contribute to some engineering problems such as noise and vibration, dust emission and snow drift around objects, etc. [39-41]. To have a better control of the flow in such applications, further studies on flow structures developing around bluff bodies are required. In order to determine the mechanisms that produce three-dimensional fluid structures at high Reynolds number, three-dimensional numerical simulation of the flow past a bluff body is conducted in the current study. A body, with fixed separation points is chosen to minimize any possible Reynolds number effects. Based on the work of Fage and Johansen [12], flow past an infinitely long inclined plate at 49.85 degrees was used. Validation of the numerical setup is first performed by comparing the pressure distribution along the plate and the shedding frequency of eddies with the experimental data. The flow visualizations in two- and three-dimensions are then processed to observe the von Kármán vortex street (two-dimensional flow structures) and the three-dimensional flow structures behind the bluff body.

### **3.2. Methodology: Geometry and numerical setup**

The computational domain and numerical setup for the flow past an infinitely long inclined flat plate are presented in this section. As discussed in the previous section, three-dimensional flow structures are expected to develop around the bluff body;

therefore, an unsteady three-dimensional numerical calculation is performed in the current study. The dimensions of the inclined flat plate are acquired from the experimental work of Fage and Johansen [12]. The width of the inclined plate is  $b = 0.15$  m, with a thickness of 3% of its width (4.53 mm) and inclination angle set at  $\Phi = 49.85$  degrees. The distances from the centre of the inclined plate to the inlet and outlet boundaries are set to  $5b$  and  $10b$ , respectively. To meet the requirement for the area based blockage ratio to be less than 3%, as recommended by Franke et al. [42], the overall vertical height of  $26b$  and the spanwise length of  $10b$  is set for the computational domain. These dimensions and the plate orientation are illustrated in Figure 3.2.

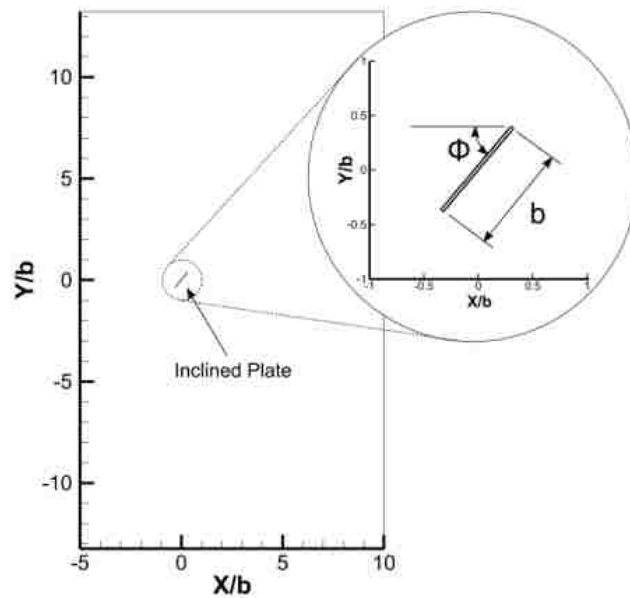


Figure 3.2: Schematic of computational domain

A freestream flow approaches the bluff body at the speed of 15.24 m/s, yielding a Reynolds number based on 'b' of  $1.57 \times 10^5$ . This uniform velocity is applied at the inlet boundary with 5% turbulence intensity and a pressure outlet condition (atmospheric pressure) is considered at the outlet boundary. To avoid any development of boundary

layers at the top, bottom and side surfaces of the computational domain that might influence the flow around the bluff body, these boundaries are treated as slip walls. The windward and leeward surfaces and two edges are modelled as no-slip wall boundaries.

The numerical study is conducted using the commercial computational fluid dynamics (CFD) software, ANSYS Fluent 15.0. The entire computational domain is discretized in space using hexahedral cells. The hexahedral cells near the inclined bluff body are aligned with the body. Grid clustering is applied around the bluff body to capture the high shear stresses. The smallest grid size is chosen to achieve dimensionless distance normal to the plate wall ( $y^+$ ) to be less than unity, where  $y^+$  is defined as  $y^+ = (u_\tau \cdot y)/\nu$  and the frictional velocity,  $u_\tau$ , is given by  $u_\tau = \sqrt{\tau_w/\rho}$ . The total number of cells in the calculation domain is approximately five million.

The governing equations are discretized using the finite volume method and the convective terms are discretized in space using a second-order upwinding scheme [13]. A second-order implicit time marching scheme is applied for time discretization with the time-step size of 0.1 ms to ensure that the Courant-Friedrichs-Lewy (CFL) number is close to unity ( $CFL \leq 3.0$ ). The semi-implicit method for pressure linked equations (SIMPLE) algorithm is selected for pressure and velocity coupling to solve the Navier-Stokes equations.

The turbulence model used in the current study is Detached Eddy Simulation (DES) [17], a hybrid of a Reynolds-Averaged Navier-Stokes (RANS) turbulence model and Large Eddy Simulation (LES). In DES, a two-equation RANS model, the SST  $k-\omega$  turbulence model [16], is applied near the wall boundaries. In previous numerical studies, it has been

shown that DES is well-suited to capture the fluid structures around a bluff body [11, 43, 44]. DES activates the RANS mode within the distance of the DES length scale ( $\tilde{d}$ ) normal to wall boundaries whereas the LES mode is turned on only outside of this range. The DES length scale  $\tilde{d}$  is determined using a delayed DES (DDES):

$$\tilde{d} = d - f_d \max[0, d - C_{des}\Delta_{max}] \quad (45)$$

$$f_d = 1 - \tanh[(8r_d)^3] \quad (46)$$

$$r_d = \frac{v_t + \nu}{\sqrt{U_{i,j}U_{i,j}}\kappa^2 d^2} \quad (47)$$

where  $d$  is wall normal distance,  $C_{des}$  is a calibration constant,  $\Delta_{max}$  is the maximum grid spacing in each coordinate direction,  $v_t$  is turbulent eddy viscosity,  $U_{i,j}$  is the velocity gradient and  $\kappa$  is the von Kármán constant which is set to 0.41 [45]. DDES maintains the RANS mode active in a thick boundary layer when the maximum grid space,  $\Delta_{max}$ , is relatively smaller than the boundary layer thickness. The governing equations for DES are summarized in Chapter 2 and are given in detail by ANSYS [19].

### **3.3. Validation: Pressure distribution along the inclined plate and shedding frequency**

To ensure that the numerical setup discussed in the previous section is appropriate, the simulation is validated using the experimental results provided in the work of Fage and Johansen [12]. The mean pressure coefficient ( $\overline{C_p}$ ) distributions along the windward and leeward of the inclined plate are compared with the experimental data, where  $\overline{C_p}$  is defined by:

$$\overline{C_p} = \frac{\overline{p} - \overline{p_0}}{\frac{1}{2}\rho U_0^2}. \quad (48)$$

The reference pressure,  $\overline{p_0}$ , is the pressure in the undisturbed air, taken in the simulation at the middle distance between the centre of the flat plate and the top face of the computational domain. The pressure data are sampled for 3 seconds (30,000 sampled data) after the flow around the bluff body has achieved a steady state condition in the mean. Figure 3.3 presents the simulated mean pressure coefficient along the leading ( $X_{alt}/b = 0.0$ ) and trailing edges ( $X_{alt}/b = 1.0$ ) of the inclined plate compared with the experimental result, where  $X_{alt}$  is the axis along the plate. The simulation shows excellent agreement with the experimental result along the windward and leeward surfaces.

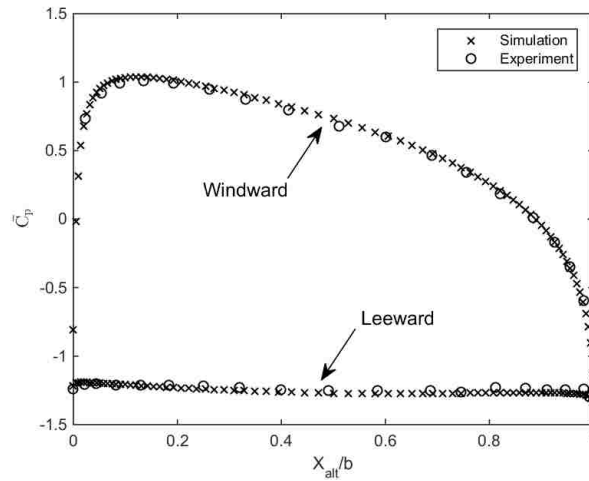


Figure 3.3: The distribution of pressure coefficient along the inclined plate

Additionally, the shedding frequency of the vortices detaching from the trailing edge is validated with the experiment. A Fast Fourier Transform of the pressure signal at the point  $X/b = 5.0$  and  $Y/b = 1.5$ , the same measurement point as in the experiments, with sampling frequency of 10 kHz over the three-second sampling time is performed. The Strouhal number ( $St$ ) associated with the peak power spectrum of the sampled signal is

found to be 0.204, equivalent to the shedding frequency of 21.36 Hz (or the shedding period of  $T = 46.8$  ms), which is close to the experimental value of  $St = 0.196$  [12].

From the above validations, it can be concluded that the simulation is properly set up to accurately capture the forces acting on the body as well as the shedding vortices. Detailed analysis of the flow development around the bluff body was then performed to elucidate the mechanisms of vortex formation and breakdown in the wake region.

### **3.4. Analysis and discussion: Flow visualizations**

In this section, the fluid structures developed around the infinitely long inclined flat plate are visualized using various approaches. Throughout this section, the transient flow development within a shedding period ( $T = 46.8$  ms) out of 64 shedding events over the three-second sampling will be considered. First, planar fields-of-view in the streamwise and spanwise directions are constructed to analyze the flow in two dimensions, which is the common scenario in experiments. Following the two-dimensional analysis, three-dimensional flow visualization is exploited to further analyze the three-dimensional fluid structures.

#### **3.4.1. Two-dimensional flow visualization**

To identify the von Kármán vortex street, an XY plane is cut through the midspan of the plate. Figure 3.4 shows plots of the instantaneous velocity vectors around the bluff body, superimposed on the contours of the Z-component (spanwise) of vorticity over a complete shedding period. The flow is from left to right in this figure and all the linear dimensions are normalized by the width ( $b$ ) of the plate. These figures clearly show that two vortices (red and blue patches near the body) shed from the leading and trailing

edges of the inclined plate. The spanwise vorticity contours capture patches of vortices (rollers) which shed periodically and travel downstream. These vortices lose strength at downstream locations in the wake. This is an indication of large energy dissipation of the flow due to the high turbulence in the wake region. Braids of shedding vortices are not captured clearly.

As mentioned in the work of Williamson [26], the streamwise vortex structures (ribs) develop along the braids, which can be observed by taking transverse cut sections in the downstream of the bluff body and plotting the streamwise vorticity contours.

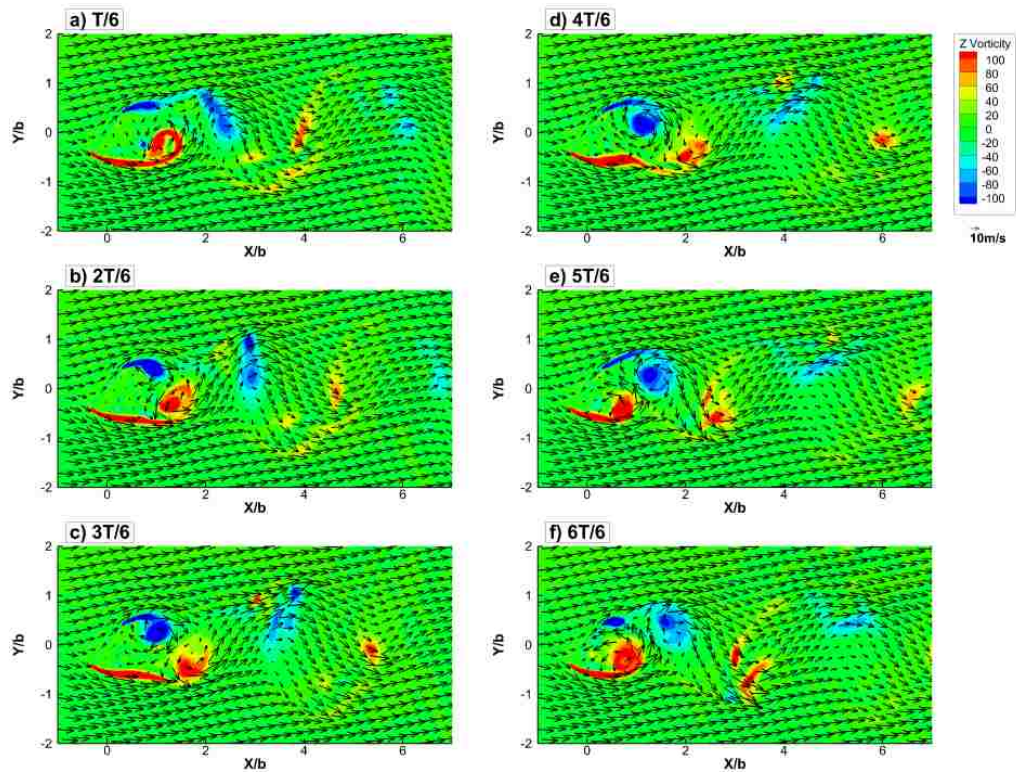


Figure 3.4: Instantaneous velocity vectors superimposed on the spanwise vorticity contours during a complete shedding period ( $T$ )

Figure 3.5 shows the instantaneous velocity vectors superimposed on the streamwise vorticity contours on the transverse cross-section ( $YZ$ -plane) at  $X/b = 1.0$  downstream from the centre of the inclined plate. The lines of spanwise vorticity at the levels of  $\pm 10 \text{ s}^{-1}$

<sup>1</sup> are also presented as a solid line ( $+10 \text{ s}^{-1}$ ) and dashed line ( $-10 \text{ s}^{-1}$ ) in the figure to identify the rollers and shear layers as they are observed in Figure 3.4. Several streamwise vortices with both clockwise and counter-clockwise sense of rotation are captured behind the plate and between the solid and dashed lines, which implies that these vortices are within the wake region. These vortex patches seem to be quite uniformly distributed between the solid and dashed lines in Figure 3.5a. With time, as indicated in Figure 3.5b-e, it is observed that the patches of streamwise vorticity oscillate within the wake region. Comparing with Figure 3.4, the streamwise vortices shift downward as the roller sheds from the leading edge in the second and third time frames of the period (Figure 3.5b,c) at this location ( $X/b = 1.0$ ), whereas the patches translate upward as the roller sheds from the trailing edge in the  $5T/6$  and  $6T/6$  time frames (Figure 3.5e,f). At this location, it is difficult to use two-dimensional analysis to identify which streamwise vortices are paired together since the flow in the wake is highly complex. The spanwise wavelength of  $1.0b$  in the mode B instability was reported by Williamson [26], while Yang et al. [33] reported values in the range from  $0.5b$  to  $1.0b$ . However, using only two-dimensional analysis, it is not easy to determine the spanwise wavelength by observing the patches of streamwise vortices or the wavy shapes of the spanwise vorticity contour lines (solid and dashed lines).



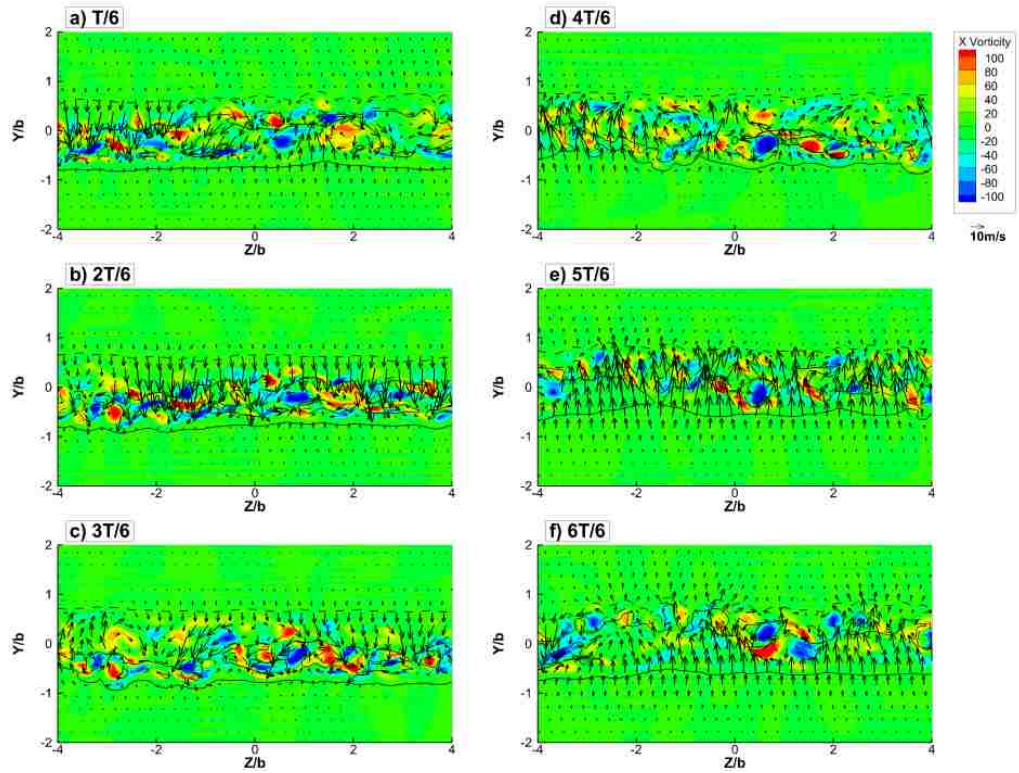


Figure 3.5: Instantaneous velocity vectors superimposed on streamwise vorticity contours on the transverse cross-section at  $X/b = 1.0$  downstream from the centre of the inclined plate over a full shedding period ( $T$ ). The contour lines of spanwise vorticity of  $\pm 10 \text{ s}^{-1}$  are shown as a solid line for counter-clockwise and as a dashed line for clockwise rotation.

Figure 3.6 shows instantaneous velocity vectors further downstream, on the transverse cross-section  $X/b = 3.0$ , superimposed on the streamwise vorticity contours. On this plane, the patches of streamwise vortices are translated even further upwards and downwards compared to those captured at  $X/b = 1.0$ . Similarly, vorticity patches are identified at the lower extreme in the first and last time frames (Figure 3.6a,f) and at the upper portion of the field-of-view in the third and fourth time frames (Figure 3.6c,d) as the braids of previously shed vortices pass this downstream plane ( $X/b = 3.0$ ). The lines of spanwise vorticity at the levels of  $\pm 10 \text{ s}^{-1}$  are also scattered, suggesting that the rollers are distorted at this distance from the bluff body where the spanwise vortices cannot be identified by the velocity vectors in Figure 3.4.

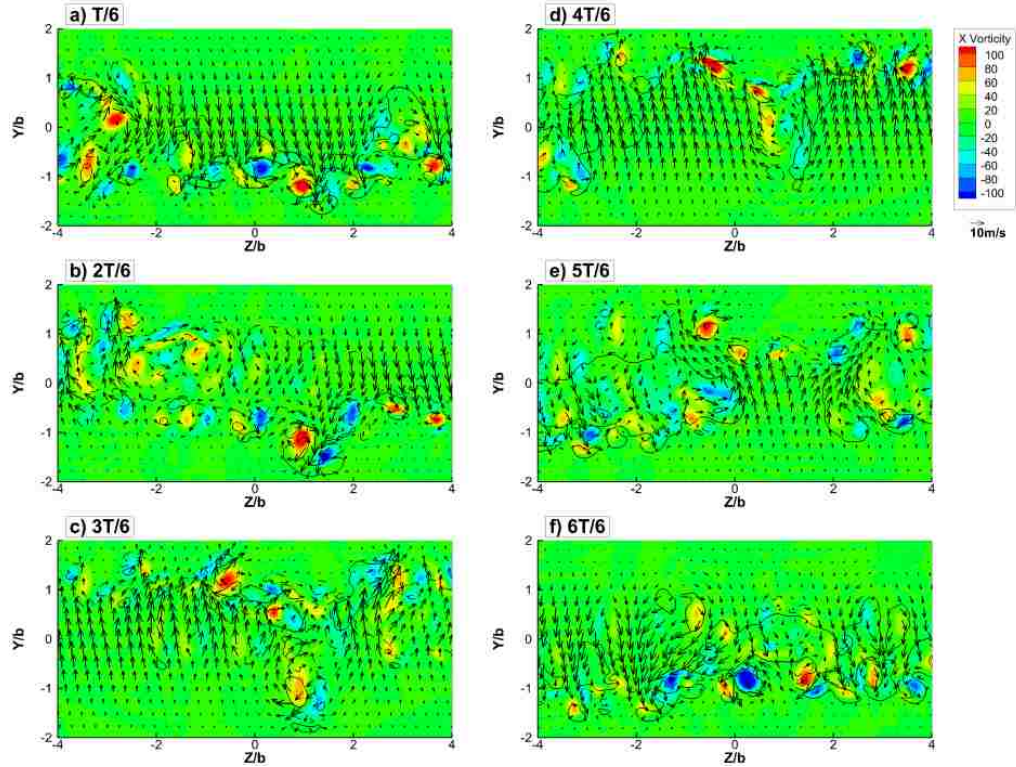


Figure 3.6: Instantaneous velocity vectors superimposed on streamwise vorticity contours on the transverse cross-section at  $X/b = 3.0$  downstream from the centre of the inclined plate over a full shedding period ( $T$ ). The contour lines of spanwise vorticity of  $\pm 10 \text{ s}^{-1}$  are shown as a solid line for counter-clockwise and as a dashed line for clockwise rotation.

From the above analysis of two-dimensional velocity vector fields and vorticity contour plots, the streamwise vortex structures are clearly identifiable within the wake region. Even though these structures follow the motion of the braids of previously shed spanwise vortices captured in the streamwise cross-section ( $XY$  plane), the structures appear scattered in the transverse cross-sections. It is difficult to connect the streamwise structures identified in the near wake at  $X/b = 1.0$  to those seen further downstream at  $X/b = 3.0$ . To fully understand the development of the streamwise vortex structures, a three-dimensional visualization is necessary.

### 3.4.2. Three-dimensional flow visualization

From the two-dimensional flow visualization, the three-dimensional nature of the flow and the relationship between the streamwise and spanwise vorticities are observed while the streamwise structures transit up and down as the spanwise vortices are generated in the wake. However, due to the complex flow pattern in transverse cross-sections in the wake, it is difficult to determine the wavelength of spanwise vortices and thereby confirm that the flow instability is in mode B.

Figure 3.7 presents the fluid structures developed around the bluff body at one time instance ( $T/6$ ) from various perspectives (Figure 3.7a-d) using the iso-surface of  $\lambda_2/\lambda_{2\min} = 0.01$  coloured with the spanwise vorticity contours where  $\lambda_{2\min}$  is the global minimum of  $\lambda_2$  in the computational domain at each instance. The value of  $\lambda_2/\lambda_{2\min}$  is selected to make the size of the iso-surface large enough to identify the major vortical structures. At this instance, a shear layer (labelled as Structure 1) is captured stretching from the leading edge and curling into the wake to form a roller (CCR1) which rotates counter-clockwise about the Z-axis. The von Kármán vortex street is captured by the rollers coloured with red (counter-clockwise rotation, CCR) and blue (clockwise rotation, CR), whereas a majority of the streamwise vortices (ribs, labelled as Structure 2) are identified in green colour. At turbulent flow conditions, two of the rollers (CR2 and CCR3) that were shed ahead of the instant shown in Figure 3.7 (located farther downstream) still maintain the shape of tubes but are somewhat distorted. Those rollers are captured with the spanwise vorticity contours in Figure 3.4a where the velocity vectors did not clearly present any eddies.

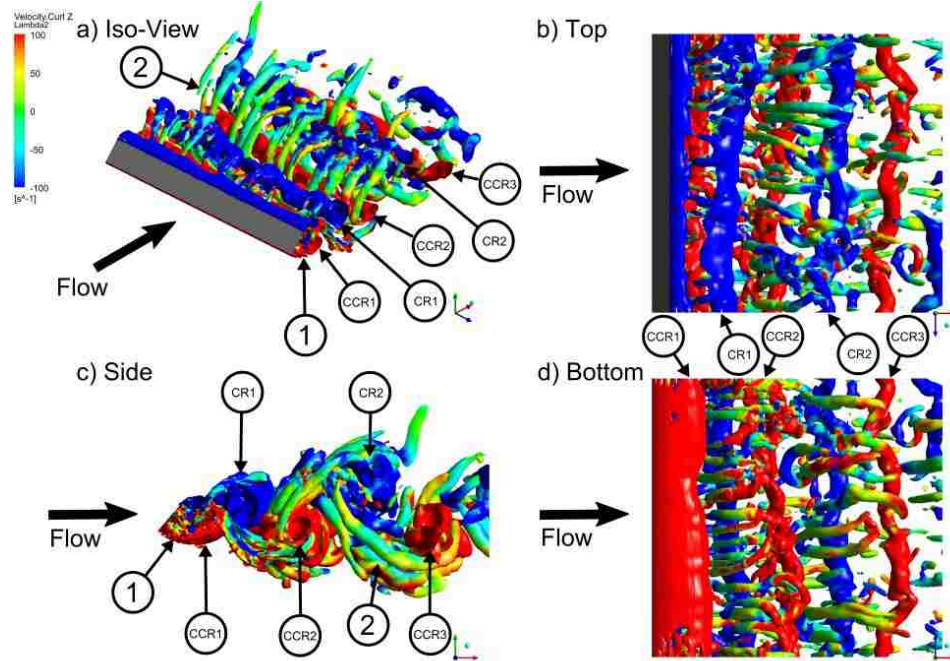


Figure 3.7: Instantaneous three-dimensional flow structures using the iso-surface of  $\lambda_2/\lambda_{2min} = 0.01$  coloured with the spanwise vorticity contours viewed from a) isometric, b) top, c) side and d) bottom, at time  $T/6$ . The arrow indicates direction of approaching flow: (1) shear layer, (2) streamwise vortices (ribs), (CR) clockwise rotating spanwise vortex, (CCR) counter-clockwise rotating spanwise vortex.

Even though pairs of streamwise vortices could not be identified in Figure 3.5, these structures are easily visualized in Figure 3.7b,d. To illustrate pairs of ribs, the iso-surface in Figure 3.7 is coloured by the streamwise vorticity contours in Figure 3.8. The spanwise wavelength of the streamwise vortices is determined by the distance between the streamwise vortex structures in counter-clockwise rotation about the X-axis. The spanwise wavelength has been reported to range from  $0.5b$  to  $2.8b$  in the work of Yang et al. [33] and  $1.0b$  in Williamson [26]. The wavelengths in the current study at two instances which are one shedding period apart are found to vary from  $0.68b$  to  $1.83b$  in this turbulent flow ( $Re = 1.57 \times 10^5$ ), which falls close to the range that has been previously reported. Even though the wavelengths vary at every period, they remain in the range between  $0.5b$  and  $2.8b$ .

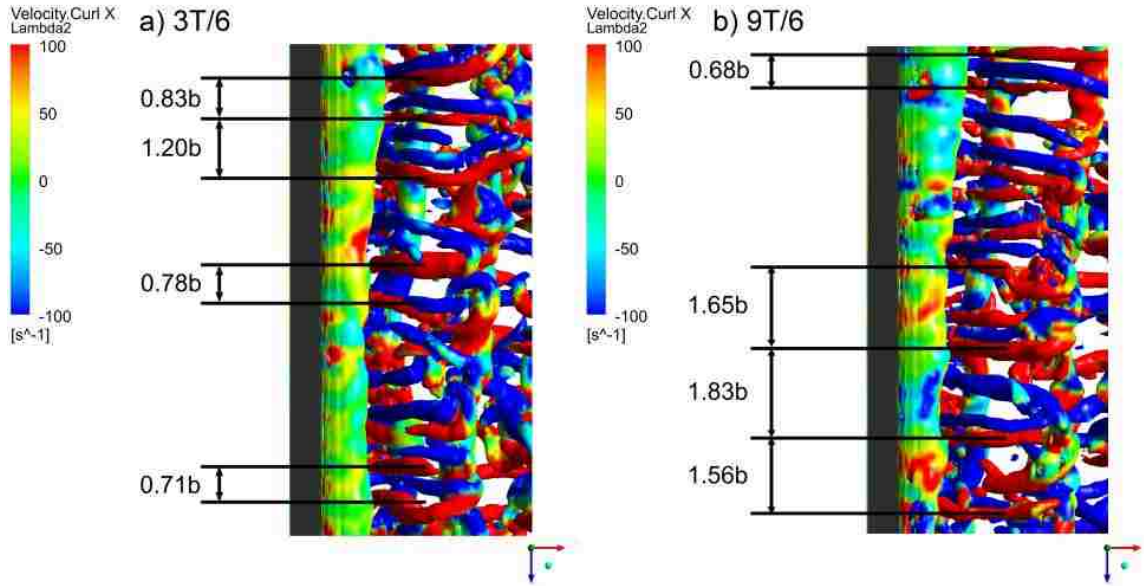


Figure 3.8: Instantaneous flow structures using the iso-surface of  $\lambda_2/\lambda_{2min} = 0.01$  coloured with the streamwise vorticity contours, viewed from the top at time a)  $3T/6$  and b)  $9T/6$ .

Figure 3.9 shows the flow structures around the bluff body at the time when a spanwise vortex is about to shed from a) the trailing edge and b) the leading edge. The roller developing from the trailing edge exhibits a wavy shape in the spanwise direction, whereas the shear layer stretching from the leading edge is much smoother until it starts to roll up. Close examination of the colour contours (streamwise vorticity) on the iso-surface shows small patches in the shear layer along the trailing edge. However, there are no patches observed in the shear layer at the leading edge. As Williamson [26] defined, the current case is in mode B (braid) instability since the flow is highly turbulent. The spanwise instability that is observed off the trailing edge is the result of the streamwise vortices (ribs) developed from the previously shed rollers, which are captured by red and blue colours in Figure 3.9. The reason for the difference between the shapes coming off the leading and trailing edges may be the flow asymmetry due to the inclination of the bluff body, but there is no clear evidence to describe the mechanism in Figure 3.9.

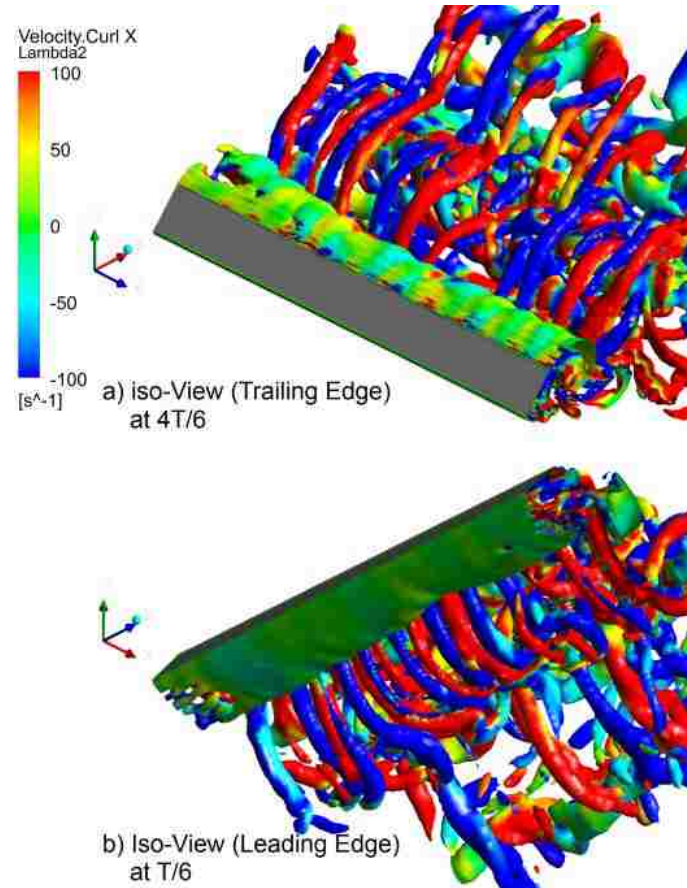


Figure 3.9: Instantaneous flow structures using the iso-surface of  $\lambda_2/\lambda_{2min} = 0.01$  coloured with the streamwise vorticity contours, in the isometric view of a) the trailing edge at time  $4T/6$ , and b) the leading edge at time  $T/6$ .

Figure 3.10 shows the iso-surface of  $\lambda_2/\lambda_{2min} = 0.01$  in a time sequence, coloured with the streamwise vorticity contours, clipped at  $Z/b = -2.3$ , viewed from the side. Gray solid lines represent the spanwise vorticity at  $\pm 250 \text{ s}^{-1}$  on the clipping plane and white dashed lines are drawn to highlight one of the streamwise vortices developing in the wake region. The streamwise vortices (ribs) are labelled as R1, R2, etc., in the order of their appearance. Similarly, the spanwise vortices (rollers) are labelled as CCR (counter-clockwise rotation) and CR (clockwise rotation). As discussed in the two-dimensional flow analysis, the ribs develop along the braids of previously shed spanwise vortices. The ribs are already developed within the wake immediately behind the bluff body. Focusing on the rib R3 in the wake region, which is highlighted by a white dashed line, the rib is

stretched towards the roller CR1 at the upper end and towards the roller CCR2 at the lower end. The rib rotates clockwise about the X-axis (blue) whereas the lower end of the rib rotates in counter-clockwise direction about the X-axis (red) as it is trapped by and bends toward the roller CCR2 (Figure 3.10a,b). This rib is trapped by both rollers and eventually breaks up into two ribs, R3 and R4 at time  $8T/8$  (Figure 3.10c). The new rib R3 is stretched along the shear layer braid of CR1 and CCR2 similar to the rib R1, and rib R4 develops along the braid of CCR2 and the newly developed roller CR2 at the trailing edge. We see that rib R3 develops in the wake, right next to the trailing edge, and does not extend to the space behind the leading edge. The spanwise vortex CR2 which starts to roll up at the trailing edge (Figure 3.10c) shows high streamwise vorticity (red) on its iso-surface, where rib R3 is rotating clockwise (blue) in the streamwise direction. This suggests that the ribs in the wake influence the instability of the rollers shedding from the trailing edge as well as the shear layer at the trailing edge. In contrast, due to the limited space and the strong shear flow at the leading edge, no rib extends into the space behind the leading edge. As a result, there is no wobbling in the shear layer at the leading edge until it starts to roll up while the roller attracts the ribs.

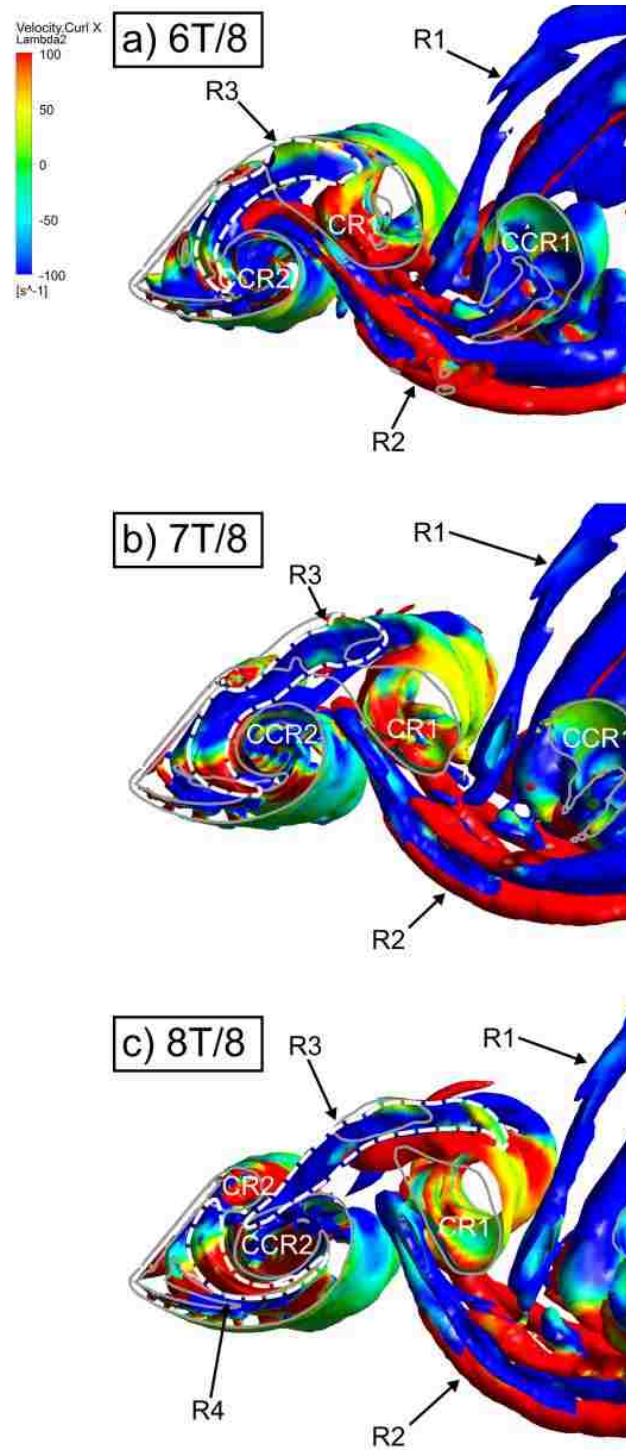


Figure 3.10: Vortical structure development in sequence in the near wake region using the iso-surface of  $\lambda_2/\lambda_{2\min} = 0.01$  coloured with streamwise vorticity contours, viewed from the side at times  $6T/8$ ,  $7T/8$  and  $8T/8$ . The iso-surface is clipped at  $Z/b = -2.3$  from the midspan of the plate to produce a clear view of the flow structures.



The instantaneous velocity vectors superposed on the streamwise vorticity contours in transverse cross-sections at the leading edge, centre and trailing edge of the inclined plate are illustrated in Figure 3.11. Again, the transverse vorticity lines at values of  $\pm 100 \text{ s}^{-1}$  are presented in the figure to represent the shear layers and rollers. Above the plate ( $Y/b > -0.382$  at the leading edge in Figure 3.11a,  $Y/b > 0.0$  at the centre in Figure 3.11b and  $Y/b > 0.382$  at the trailing edge of the plate in Figure 3.11c), the upward flow is obviously due to the flow along the inclined plate. Two dashed lines near the trailing edge represent the shear layer stretching from the edge (Figure 3.11c). Well-organized streamwise vorticity patches are observed within the shear layer. Even though no counter-rotating vorticity patches representing the ribs which are captured in Figure 3.10 are captured right next to the patches within the shear layer in the contour plot (Figure 3.11c), observation of velocity vectors in the spanwise direction near the trailing edge indicate a connection to the ribs developed parallel to the shear layer. This leads to the conclusion that the shear layer (which evolves into a braid) is perturbed by the wake behind the body. This observation also matches with the flow structure development illustrated in Figure 3.10 and with mode B reported by Williamson [26] (Figure 3.1). In comparison, such strong streamwise vortices are not captured in the transverse cross-sections at the leading edge and centre of the inclined plate since there is a little space for the wake to develop a strong lateral flow component. The solid lines in Figure 3.11 also present the evidence of a smooth shear layer at  $X/b = -0.322$  and  $0.0$  (Figure 3.11a,b) whereas the small disturbance is shown at  $X/b = 0.322$  (Figure 3.11c) as the roller traps the ribs while it develops.

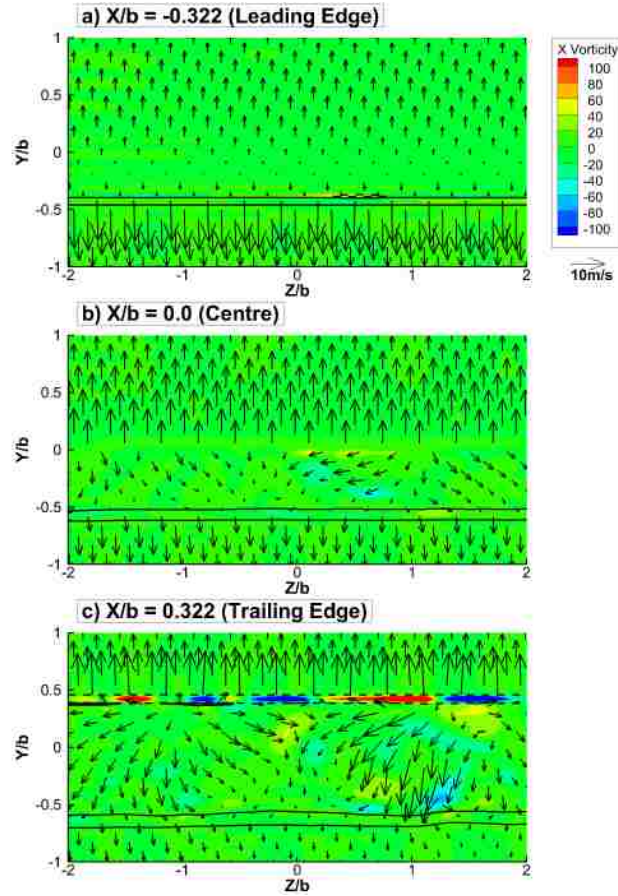


Figure 3.11: Instantaneous velocity vectors superimposed on streamwise vorticity contours on the transverse cross-section at the a) leading edge ( $X/b = -0.322$ ), b) centre of the plate ( $X/b = 0.0$ ) and c) trailing edge ( $X/b = 0.322$ ) at  $T/6$  of a shedding period. The contour lines of transverse vorticity are at levels  $\pm 100 \text{ s}^{-1}$ , where a solid line corresponds to the positive (counter-clockwise) value and a dashed line represents the negative (clockwise) value.

As observed in Figure 3.10, the streamwise vortices develop in the wake immediately after the plate; however, there is no sign of these vortices in Figure 3.11 other than the ones which developed within the shear layer at the trailing edge since the vortices develop parallel to the leeward of the inclined flat plate. To further understand the flow development adjacent to the inclined plate, cut planes normal to the body are generated (Figure 3.12). A new coordinate system is obtained by rotating the Cartesian X- and Y-axes through  $49.85$  degrees about the centre of the inclined plate ( $X/b = 0.0$ ). The axes parallel and normal to the plate are denoted as  $X_{\text{alt}}$  and  $Y_{\text{alt}}$  respectively. All variables are accordingly projected to this new coordinate system.

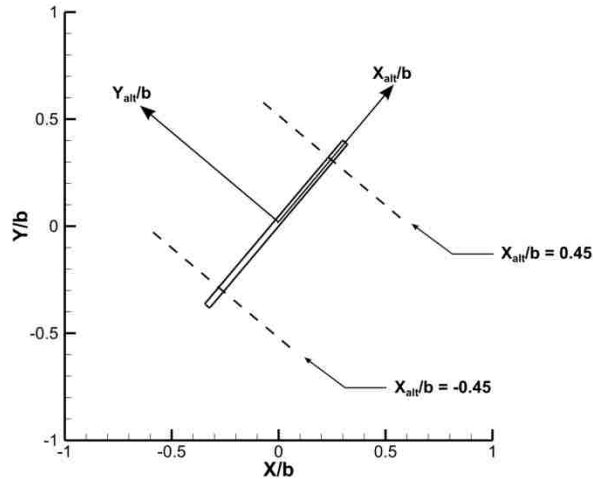


Figure 3.12: New coordinate system with axes parallel ( $X_{alt}$ ) and normal ( $Y_{alt}$ ) to the inclined plate, and locations of planes normal to the plate used in Figure 3.13 and 3.14.

Figure 3.13 displays the instantaneous velocity vector field superimposed on the contours of the vorticity parallel to the plate ( $X_{alt}$ -vorticity) on the cross-section normal to the plate at  $0.05b$  from the leading edge ( $X_{alt}/b = -0.45$  in Figure 3.12). Note that the  $X_{alt}$ -axis points into the plane in Figure 3.13; therefore, the positive contours of the  $X_{alt}$ -vorticity represent clockwise rotation, whereas negative vorticity indicates anti-clockwise rotation. It is also noted that windward of the inclined plate is in the positive  $Y_{alt}$  direction. The size of the wake region in this plane is found to be about  $0.5b$  from the leeward of the plate, using identification of vorticity contours and small magnitude velocity vectors. The strength of the vortices captured on this plane is small ( $\pm 10 \text{ s}^{-1}$ ), the patches of vortices are more organized since the flow is not significantly distorted near the leading edge region due to the small size of the wake region, as discussed in connection with Figure 3.10 and 3.11.

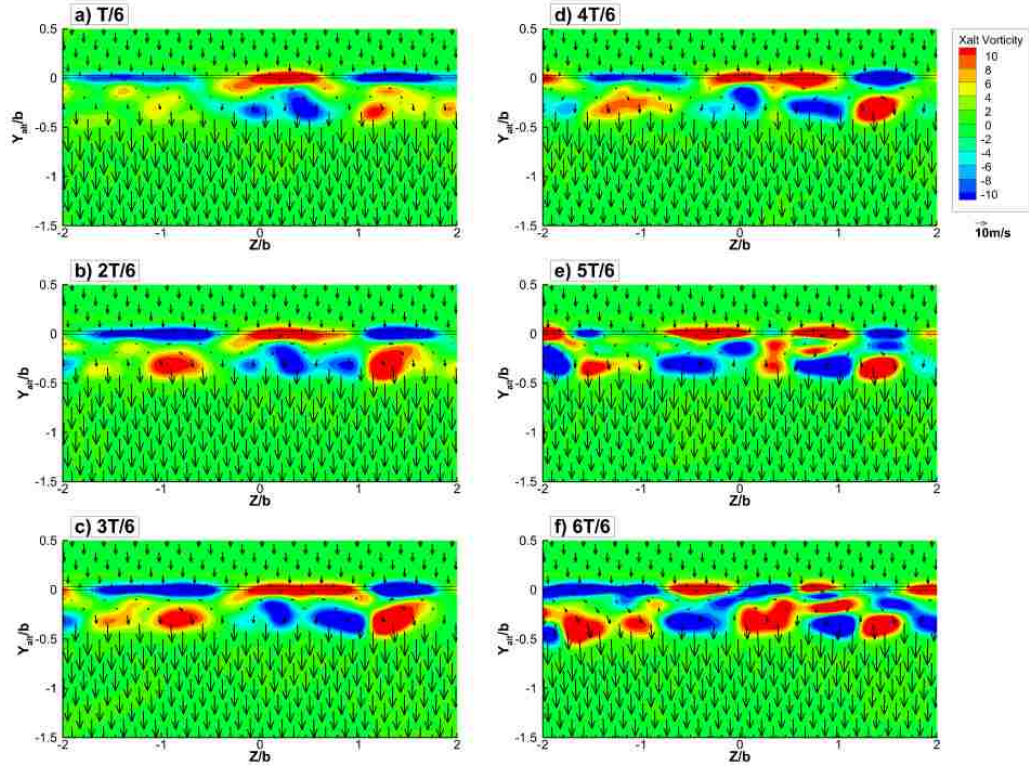


Figure 3.13: Instantaneous velocity vectors superimposed on  $X_{alt}$ -vorticity contours on the cross-section normal to the plate near the leading edge ( $X_{alt}/b = -0.45$ ) over the shedding period ( $T$ ). Solid lines near  $Y_{alt}/b = 0.0$  represent the cut section of the inclined plate.

Figure 3.14 shows the same instantaneous velocity vectors superimposed on the  $X_{alt}$ -vorticity contour plots on the plane normal to the inclined plate close to the trailing edge ( $X_{alt}/b = 0.45$  in Figure 3.12). Note that the range of  $X_{alt}$ -vorticity at this location is set to  $\pm 50 \text{ s}^{-1}$  for clarity of vortex identification. As observed in the previous discussion, the flow in the wake region is very complicated for this highly turbulent flow; thus, there is no clear periodic flow pattern observed in this cross-section. The velocity vectors adjacent to the leeward surface point towards the plate as the spanwise vortex develops around the trailing edge. Since the vortices captured near the trailing edge are stronger than those observed near the leading edge (Figure 3.13), the shear layer and roller developed from the trailing edge exhibits wobbling as observed in Figure 3.9. Also note that spanwise instability of the flow along the windward surface of the plate is considered

to contribute to the instability of the shear layer and rollers at the trailing edge. However, the vorticity contours in the windward side do not show significant strength compared to those in the wake region. Therefore, it can be concluded that the development of streamwise structures in the wake dominates the instability of the shear layer and rollers. The inclination of the flat plate induces the asymmetry of flow where the shear flow is dominant near the leading edge whereas the wake has significant influence near the trailing edge. Yet, spanwise vortices are the largest fluid structure in the wake, but the streamwise structures distort the spanwise vortices in the downstream region as observed in Figure 3.7.

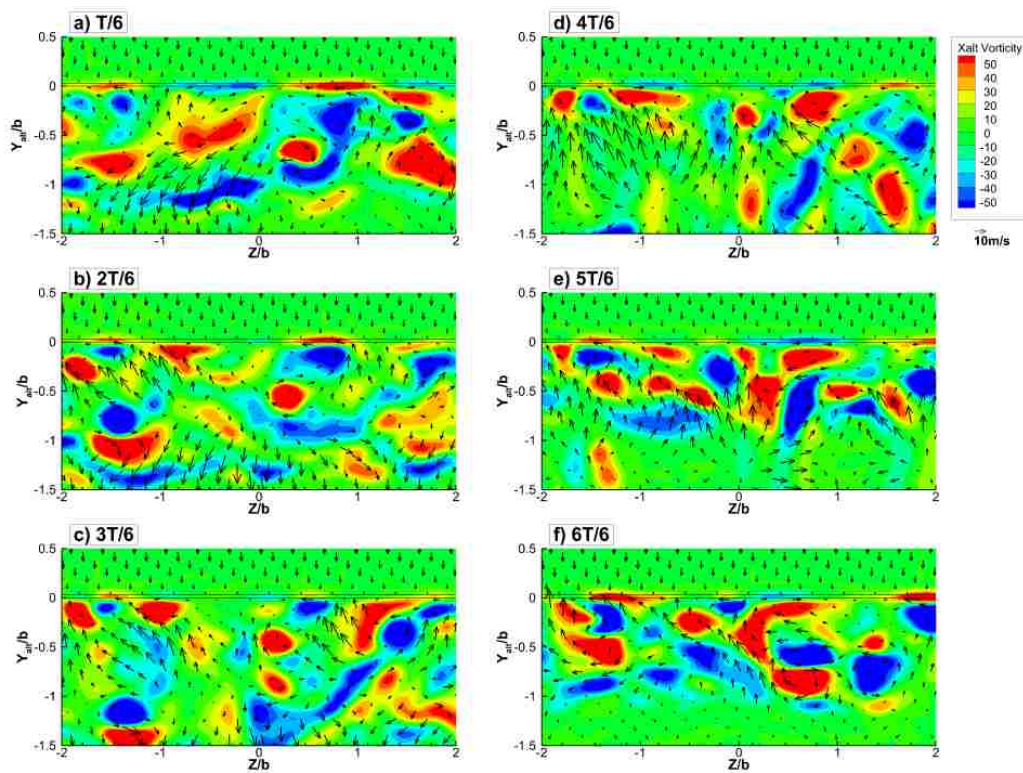


Figure 3.14: Instantaneous velocity vectors superimposed on  $X_{alt}$ -vorticity contours on the cross-section normal to the plate near the trailing edge ( $X_{alt}/b = 0.45$ ) over the shedding period ( $T$ ). Solid lines near  $Y_{alt}/b = 0.0$  represent the cut section of the inclined plate.

### 3.5. Conclusions

The classical flow past the infinitely long inclined plate is simulated, visualized in two- and three-dimensions, and the three-dimensional fluid structures that develop around the bluff body are analyzed. In the two-dimensional flow analysis, the streamwise (XY) plane in the midspan of the inclined plate captures the spanwise vortices that are periodically shed from the leading and trailing edges of the body. However, these vortices do not maintain their shapes farther downstream from the body. The streamwise vortical structures are examined in the transverse (YZ) section planes at  $X/b = 1.0$  and  $3.0$ . Near the bluff body ( $X/b = 1.0$ ), these structures are found to develop within the wake which is identified by the region between the shear layers at the leading and trailing edges. The fluid structures follow the upward and downward motions as they are trapped by the previously shed spanwise vortices. Even though there is obviously a relationship between the spanwise and streamwise vortex structures, it is difficult to stitch together the patches of each vorticity contour at different cross-section planes to visualize the fluid structures around the body. Therefore, three-dimensional flow visualization is necessary.

The three-dimensional fluid structures are visualized using the  $\lambda_2$ -criterion. This approach is able to visualize the spanwise vortices (rollers) shed from the edges of the body as well as the streamwise vortex structures (ribs) that develop along the braids of the spanwise vortices. It successfully captures the distortion of the spanwise vortices at downstream locations as seen in the streamwise two-dimensional cross-section planes. The streamwise structures can be easily identified by colouring the iso-surface with streamwise vorticity contours. The wavelength of these structures is found to range from  $0.68b$  to  $1.83b$ . The wobbling (spanwise instability) of the shear layer and roller at the

trailing edge is also captured by the iso-surfaces, whereas a smooth shear layer is observed at the leading edge. By taking a cut view to illustrate the flow structures inside the wake, it is shown that these streamwise vortex structures develop in the wake region and are trapped by the shed vortices. Since there is little available space near the leading edge, the shear layer at the leading edge experiences little disturbance, whereas the one at the trailing edge is significantly influenced by the wake. The differences between the flow near the leading and trailing edges are also identified by viewing the velocity vectors and vorticity contours on the transverse cross-sections near the edges and cross-sections normal to the inclined plate. The cross-sections normal to the plate illustrated weak and organized vortices along the plate near the leading edge whereas captured strong and scattered vortices near the trailing edge. The observations demonstrate the influence of streamwise vortices develop next to the plate on the shear layer at the trailing edge.

## **Chapter 4. Analysis of flow structures around an inclined plate near a wall**

### **4.1. Introduction**

Flow past bluff objects in close proximity to the ground are of interest to engineers. A typical example is a ground mounted solar panel. Since solar panels require open space to avoid obstructive shadows, they are usually located in open terrain where they may be subjected to strong wind loads which could damage the panels.

A number of studies have been conducted to establish the characteristics of flow past near-wall mounted bluff bodies. Bosch et al. [46] experimentally studied the flow past a square cylinder suspended horizontally at various gap heights ( $H$ ). Vortex shedding was observed for normalized gap heights ( $H/D$ ) greater than 0.5, where  $D$  is the cylinder height, while there was suppression of shedding at lower values. They also noticed an asymmetric flow behaviour due to the effect of the ground at the normalized gap height of 0.75 or smaller. Plots of the phase-averaged velocity vector fields and vorticity contours illustrated that the vortex shedding from the lower side of the cylinder first travelled streamwise then started to shift away from the wall at around three characteristic lengths ( $3D$ ) downstream of the body. The strength of the vortices shed from upper and lower sides of the cylinder was found to be the same near the body, but the lower one decayed rapidly compared to the upper. It was observed that the lower vortex trapped a clockwise vortex at the wall as Bosch and Rodi [47] had reported in their numerical study. Additionally, the decrease of shedding frequency and the expansion of a



recirculation zone as the gap to characteristic length ratio decreases were reported by Straatman and Martinuzzi [48] and Shi et al. [49], respectively.

Lee et al. [50] also carried out a two-dimensional simulation of flow behind a rectangular cylinder near the ground. The study was primarily focused on the effects of the aspect ratio of the cylinder and the gap height from the ground. A modified Shear-Stress Transport (SST)  $k-\omega$  turbulence model was employed for prediction of the separated flow region. The unsteady simulation was conducted with the cylinder aspect ratio ranging from 0.5 to 1.0 and the normalized gap height ranging from 0.3 to 2.0. Lift coefficient plots illustrated vortex shedding when the normalized gap height was greater than 0.6, while the shedding was suppressed for values less than 0.5 gap height. Two dominant shedding frequencies were found for normalized gap heights of 0.6 and 0.7, of which the lower frequency was caused by the additional flow separations on the ground.

Numerical investigations of the flow around a two-dimensional inclined plate near a wall were reported by Li et al. [39] and Lan et al. [51] at two different Reynolds numbers of 300 and 20000, respectively. These studies considered the flow approaching from  $180^\circ$  azimuthal angle, with the lower surface of the plate facing towards the upstream direction, with various inclination angles and gap to chord length ratios of 0.3 to 2.0. Using the SST  $k-\omega$  turbulence model, they found that a higher pressure coefficient was observed as the gap ratio increased, which was later confirmed by the results of Shademan et al. [11] using Detached Eddy Simulation.

Compared to the flow separation from two-dimensional bluff bodies, the single bluff body with finite length also experiences separations at its side edges and the flow around

the plate becomes highly three-dimensional. The early stage three-dimensional wake formation behind polygonal plates was studied by Higuchi et al. [52] in a low-speed water channel. Triangular, square, hexagonal and octagonal plates were examined by visualization of illuminated dye released from the side edges of the plates. Each shape produced a longitudinally non-uniform vortex which rolled up from each edge and formed a bow shape. Secondary hairpin vortices rotating opposite to the primary vortices formed at the corners of the triangular plate. On the other hand, a continuous but non-planar vortex loop was formed behind the square plate, deforming inward from the four corners and eventually taking a diamond-like shape. Similarly, the arched vortices stretching from each edge formed a vortex ring behind hexagonal and octagonal plates with the observation of apex shifting. The presence of more corners on the plate as the number of edges increased resulted in a shape of the vortex ring appearing closer to that of a round disk. It was also found that the time to lose its original structure that developed along the edges and to form a complete three-dimensional wake took longer as the number of sides increased.

Some studies have recently been conducted to understand the characteristics of flow past ground mounted bluff bodies that are representative of solar panels. Shademan and Hangan [2], Shademan and Hangan [53] analyzed the wind loading on inclined panels in terms of wind directions and inclination angles using steady Reynolds-Averaged Navier-Stokes (RANS) simulations for mean flow analysis. Their results show that the maximum loading occurs when the wind approaches the panel normally on to the front or back of the panel. Jubayer et al. [10] and Jubayer and Hangan [9] carried out further experimental and numerical studies on a single inclined plate near a wall. The experiments were

conducted in a boundary-layer wind tunnel facility with the model scale of 1:10 whereas the numerical study was set for full-scale in the atmospheric boundary layer environment using the SST  $k-\omega$  turbulence model for the unsteady RANS simulations. The wind load results of the experiments and the simulation matched with that of Abiola-Ogedengbe et al. [54] and showed the flow attachment on the windward surface and flow separation on the leeward side. However, they found that the SST  $k-\omega$  turbulence model was not able to capture the vortex shedding from the panel and recommended the use of Large Eddy Simulation (LES) or Detached Eddy Simulation (DES) instead.

Shademan et al. [11, 55] studied the wind loading on a single inclined plate due to the effects of ground clearance using RANS simulations and DES. DES was able to successfully capture the vortex shedding from the panel. It also indicated that the wind load on the inclined plate near the wall was reduced when the ground clearance was minimized. Moreover, the amplitude of the fluctuating force was found to increase as the gap increased, which could lead to damage. The mean flow streamlines depicted stretching of the recirculation bubble in the downstream direction and captured a separation bubble at the trailing edge for the small gap case. Using  $\lambda_2$ -criterion, they showed the formation of hairpin-like vortices in the wake. These vortices retain their shapes in the larger ground clearance case, whereas the vortices were distorted with patches of high shear stress on the ground in the small clearance case. At the same time, meandering structures were observed in the downstream region for the small gap.

It is clear from the literature that the structure of the flow around plates and bluff bodies has been discussed mainly from the point of view of the wind directions and plate tilt angles. It is also noted that the majority of studies have focused on mean flow

characteristics with little discussion on the effect of the ground on the formulation and development of fluid structures. As observed in the studies of flow around a bluff body near a wall, the small gap between the body and the wall has significant impact in the wake region. Once the finite bluff body is set near a wall, the flow from the sides of the body interacts with the flow from the top and bottom of the body and generates unique flow structures in the downstream. However, the interaction of the flow around the body and the formation of the flow structures in the wake region is not clearly understood. In order to identify the process of flow development around the body, a transient simulation study will be required to investigate the development of the flow. In an effort to further understand the flow features, the present computational fluid dynamics (CFD) simulation is considered in two stages: (1) at the start of the flow (early stage) and (2) when the flow reaches a fully turbulent and steady state condition (in the mean) of pressure along the flat plate. The computational domain is initialized with zero velocity at  $t = 0.0$  sec so that there is no flow disturbance around the bluff body at the start of the flow. This allows tracking the fluid structures that develop in the early stage and relate them to the flow observed in the stage of steady state condition in mean. Mean and instantaneous flow analyses at two gaps are undertaken, with one clearance below the previously reported critical condition and one above it. Several methods of analysis are used to study the effects of the wall. The fluid structures are also studied using the  $\lambda_2$ -criterion for three-dimensional flow visualization.

## 4.2. Methodology

### 4.2.1. Geometry setup

The cases analyzed in this study are similar to the work of Shademan et al. [11]. The dimensions of the inclined plate are presented in Figure 4.1. A 4.2 m long (L), 3.2 m wide (b) and 0.05 m thick plate is set to an angle of  $\phi = 135^\circ$  from the horizontal plane with respect to the upwind direction (Figure 4.1a). The gap (H) between the plate and wall is maintained at 0.5 m and 2.5 m for the two simulation cases. The projected height of the inclined plate onto the vertical plane,  $\Delta = b \cdot \sin(\pi - \phi)$ , is used to normalize all dimensions. Based on the results of Shademan and Hangan [2], Shademan and Hangan [53], this study uses a wind approaching the plate with zero yaw angle to represent the case of highest wind loading on the plate. As recommended by Franke et al. [42], all the dimensions of the computational domain are determined by ensuring that the area blockage ratio of the plate is less than 3% (Figure 4.1b). The design wind velocity at 10 m above the ground is selected as 25 m/s based on the 1-in-30-year hourly wind speeds at Windsor, Ontario, defined in the National Building Code [56], yielding a Reynolds number based on the projected height of the inclined flat plate,  $\Delta$ , of  $3.65 \times 10^6$ .

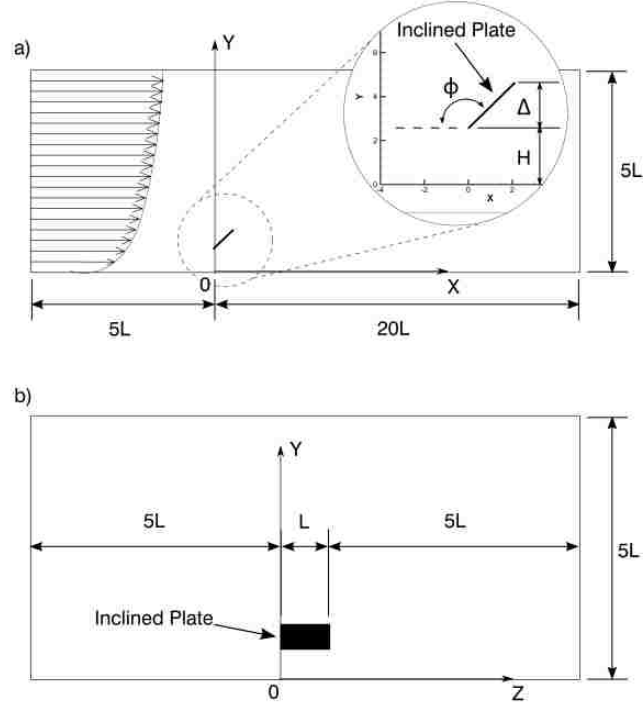


Figure 4.1: Dimensions of calculation domain, a) side view and b) view from the inlet

The approaching flow velocity profile at the inlet boundary is modelled using a power-law equation:

$$\frac{U(Y)}{U_g} = \left(\frac{Y}{y_g}\right)^\alpha \quad (49)$$

Here  $U_g$  is the geostrophic wind velocity,  $Y$  is the distance from the ground,  $y_g$  is the atmospheric boundary layer height in an open terrain and the exponent  $\alpha$  is dependent on the type of terrain. In the current simulations, an open terrain is considered to represent the environment where the inclined plate is installed, hence the values of  $y_g = 300$  m and  $\alpha = 0.16$  are used [57]. The calculated power-law inlet velocity and turbulence intensity profiles have been verified with the experimental data in ESDU 82026 [58] and ESDU 83045 [59] (Figure 4.2). The velocity and turbulence intensity profiles at the inlet boundary and the incident location (the location of the leading edge without the body) are plotted to confirm that the upstream flow is preserved while it approaches the bluff body.

The top and side walls of the calculation domain are set to be impermeable slip boundaries whereas the bottom and plate surfaces are treated as no-slip smooth wall boundaries. The downstream boundary is specified as an outlet flow where the velocity gradient normal to the boundary is zero.

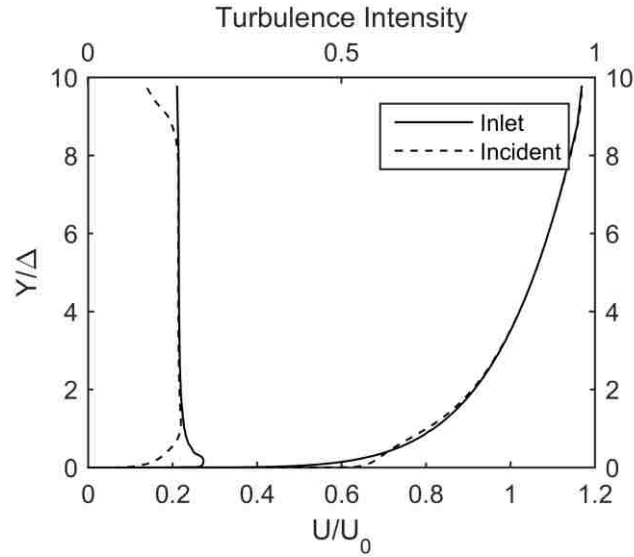


Figure 4.2: Velocity (—) and turbulence intensity (- - -) profiles at the inlet boundary

The CFD software ANSYS Fluent 15.0 is used to carry out the simulations. The regions adjacent to the plate and bottom wall are meshed with hexahedral cells which are clustered toward the physical boundaries to capture the high shear stresses in these regions. The grid size of the clustered regions is set to achieve a value of  $y^+ < 1$ , where  $y^+$  is defined as  $y^+ = (u_\tau \cdot y)/\nu$  and  $u_\tau = \sqrt{\tau_w/\rho}$ . In these expressions  $u_\tau$  is the friction velocity,  $y$  is the normal distance from the boundaries,  $\nu$  is the kinematic viscosity,  $\tau_w$  is the wall shear stress and  $\rho$  is the air density. Following the mesh setup requirements described above, the mesh is refined by 10% increments of the number of grid points in each direction until grid independence is determined by observing no significant change in drag and lift forces. Based on the grid independence study, 3.97 million cells are used

for the small ground clearance case and 4.69 million cells are used for the larger ground clearance.

#### **4.2.2. Governing equations**

To compute the transient flow around the inclined plate, the three-dimensional unsteady turbulent Navier-Stokes equations are solved [13]. The finite volume method is used to discretize the governing equations and a second-order upwind scheme is used for spatial discretization of the convective terms. Second-order implicit time marching is applied with a time-step size of 0.1 ms which ensures that the Courant number is close to unity ( $CFL \leq 1.0$ ). Pressure and velocity are coupled using the SIMPLE algorithm.

The primary objective of this research is to capture the flow structure details which were not observable in previous studies. Based on existing literature, DES has been shown to be an appropriate choice for the turbulence modeling for this type of flow [43, 44]. DES is a hybrid of LES and RANS, where one model compensates for the weakness of the other to yield good predictions in high Reynolds number boundary layer flow and flows with large separation [17]. Details of the governing equations are available in Chapter 2.

Shademan et al. [11] validated the above-mentioned models and numerical formulations with data from wind tunnel experiments on flow past an infinitely long flat plate conducted by Fage and Johansen [12]. For the validation case, the predicted mean pressure coefficient distribution at the centre of the front and back of the plate showed good agreement with the experimental results. The power spectra were also calculated based on the Fast Fourier Transformation (FFT) of the pressure over the sampling period. A Strouhal number of 0.140 was obtained, which is close to that of 0.147 reported by



Fage and Johansen [12]. This result confirms that the numerical modeling was properly set to capture the unsteady flow features around the bluff body. Further details on the model validation have been discussed by Shademan et al. [11] and avoided here for brevity.

### **4.3. Mean flow analysis**

In this section, a quantitative evaluation of the flow is carried out by analysing the mean streamwise, depthwise and spanwise velocity profiles at multiple stations downstream of the plate. Time-average values are obtained by sampling for three seconds after the flow has achieved a fully developed condition. Sectional streamlines based on mean velocities on the central plane and on different planes parallel and normal to the plate are plotted, and colour contoured with vorticity normal to each plane. Three-dimensional analysis using the  $\lambda_2$ -criterion is performed to identify and investigate the fluid structures around the bluff body. The three-dimensional analysis is divided into two subsections: early stage development of flow and fully developed flow. From this point onwards, the two cases in this study are identified by the ratio of the gap height (H) to the characteristic length ( $\Delta$ : projected height of the inclined plate), which takes values  $H/\Delta = 0.22$  and  $1.11$  for gap heights  $H = 0.5$  m and  $2.5$  m, respectively.

The mean field for the fully developed flow is first presented to provide an overview of the flow characteristics. Figure 4.3 show the mean streamwise velocity,  $\bar{U}$ , depthwise velocity,  $\bar{V}$ , and spanwise velocity,  $\bar{W}$ , normalized by the velocity of the approaching flow at the height of the leading edge,  $U_0$ , measured on the central plane at various downstream locations from the leading edge ( $X/\Delta = 0$ ) of the inclined plate, at  $X/\Delta = 0.5, 1.5, 2.5$  and  $3.5$ . To facilitate comparisons between the small and large ground clearance

cases, the Y-direction is divided into two regions and each is normalized separately: the gap region ( $0 \leq Y \leq H$ ) is normalized by the gap height, H, whereas the upper region ( $Y \geq H$ ) is normalized by the projected height of the solar panel,  $\Delta$ . The new normalized Y-axis is labelled as  $Y^*$ . The leading and trailing edge of the plate are matched at  $Y^* = 1.0$  and 2.0, respectively.

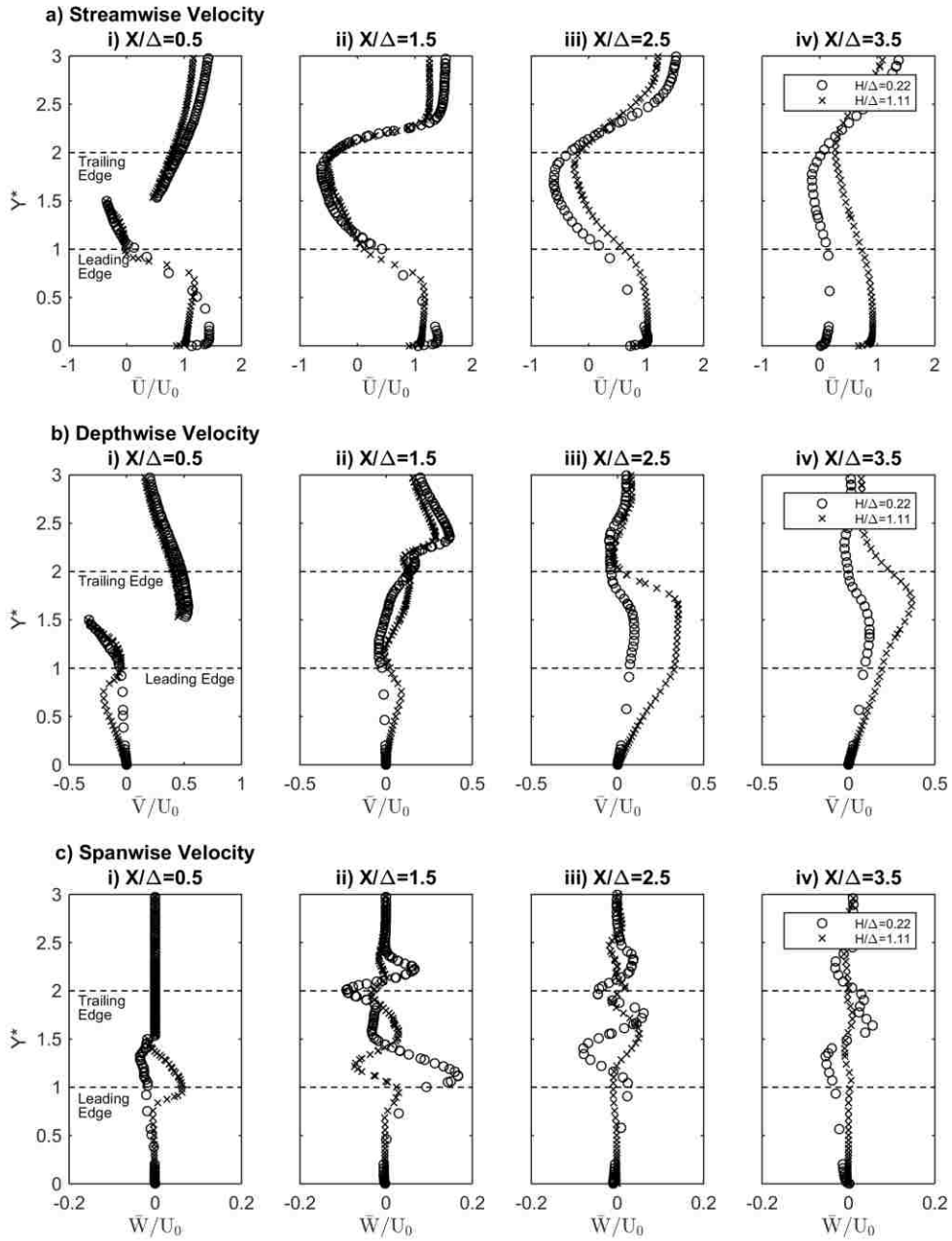


Figure 4.3: Velocity profiles at locations  $X/\Delta = 0.5, 1.5, 2.5$  and  $3.5$ . a) streamwise; b) depthwise; c) spanwise velocity

As shown in Figure 4.3a, the location of the peak streamwise velocity in the gap region is dependent on the gap height. The peak streamwise velocity in the small gap case ( $H/\Delta = 0.22$ ) is identified close to the wall, whereas the peak in the larger gap case ( $H/\Delta = 1.11$ )

is found close to the plate. For instance, at  $X/\Delta = 0.5$ , the peak occurs at  $Y^* = 0.13$  for  $H/\Delta = 0.22$  and at  $Y^* = 0.62$  for  $H/\Delta = 1.11$ . A similar trend in maximum streamwise velocity location was also observed in studies of the flow past a rectangular cylinder near a wall by Kim et al. [60], Kim et al. [61] and Lee et al. [50]. They identified the maximum velocity in the space between the obstacle and the wall at  $Y/H \approx 0.3$  for  $H/\Delta = 0.3$  and  $Y/H \approx 0.6$  for  $H/\Delta = 1.0$ . Figure 4.3a also illustrates that the maximum streamwise velocity in the small gap case continuously drops with increasing downstream distance and the peak shifts upwards to  $Y^* \approx 0.57$  at  $X/\Delta = 3.5$ . On the other hand, the peak of the velocity profiles shifts towards the wall with increasing streamwise distance in the larger gap case, while there is a slight increase in magnitude at  $X/\Delta = 1.5$  then a decrease further downstream. This slight increase in magnitude is due to the wake region stretching downwards because of initial strong downwash observed in depthwise velocity profiles (Figure 4.3b).

In the upper region ( $Y^* \geq 1.0$ ), the velocity profiles show a similar pattern for both gaps and at each downstream station. The profiles in the wake region immediately behind the plate also show a gradual decrease in velocity with increasing vertical and horizontal distances. The streamwise velocities are negative through most of the wake region behind the inclined plate. As expected, above the trailing edge, the velocity once again becomes positive. For the case  $H/\Delta = 1.11$ , at  $X/\Delta = 3.5$  the streamwise velocity is positive throughout the section indicating that these measurements are outside of the wake region. It is clear that the size of the wake region in the small gap case is elongated in the downstream direction compared with the larger clearance case.

The depthwise component in Figure 4.3b clearly show that the larger gap case has a strong downwash (negative  $\bar{V}/U_0$ ) beneath the inclined plate (at  $X/\Delta = 0.5$ ) compare to the small gap case, which experiences only a slight downwash. Further downstream the flow transitions to an upwash with increasing  $X/\Delta$  up to  $X/\Delta = 2.5$  beyond which it decreases for the large gap. These transitions match with the slight increasing streamwise velocity at  $X/\Delta = 1.5$  and decreasing of the velocity further downstream. For the small gap case there is little change in depthwise velocity in the gap region with a minor increase in upwash with increasing  $X/\Delta$ . Similar to the streamwise velocity profiles, gradual transitions along the vertical axis are identified in the depthwise velocity profiles, which correspond to locations being within or outside the wake region. The difference in the size of the separated wake regions is also noted from the difference in the depthwise velocity profiles at  $X/\Delta = 2.5$  and  $3.5$ , which is also captured in the mean streamtraces (Figure 4.4).

The spanwise velocity profiles at the four stations are presented in Figure 4.3c. The maximum spanwise velocity is about one-fifth to one-tenth of the other components of velocities;  $|\bar{W}/U_0|_{\text{Max}} \approx 0.15$  for  $H/\Delta = 0.22$  whereas  $|\bar{W}/U_0|_{\text{Max}} \approx 0.08$  for  $H/\Delta = 1.11$  at  $X/\Delta = 1.5$ . In general, the mean spanwise velocity on the central plane is expected to be near zero [62] as observed near the wall and above the plate ( $Y^* > 1.5$ ) at  $X/\Delta = 0.5$ . In the gap region, it is observed that the variation starts near the leading edge of the plate for the larger gap case, for example  $Y^* \approx 0.75$  at  $X/\Delta = 0.5$ , whereas changes in the spanwise velocity begin to occur near the wall for the small gap case ( $Y^* \approx 0.4$  at  $X/\Delta = 0.5$ ). The changes in the spanwise velocity profiles along the vertical axis are due to the sections cutting through the wake region. The near-zero spanwise velocity is recorded throughout

the section at  $X/\Delta = 3.5$  for  $H/\Delta = 1.11$  as the station is outside of the wake region. It is interesting to realize that the trend in the velocity profiles for  $H/\Delta = 1.11$  observed at a particular station seems to occur at the subsequent station for  $H/\Delta = 0.22$ . For instance, the profile for  $H/\Delta = 1.11$  at  $X/\Delta = 1.5$  gradually shifts to positive near the leading edge of the plate, switches over to negative and reaches a peak around  $Y^* = 1.2$ , then shifts back to positive again at  $Y^* \approx 1.6$ , and eventually gets weaker as it moves away from the wall. Even though the magnitude is different, the trend matches with the profile for  $H/\Delta = 0.22$  at  $X/\Delta = 2.5$ . One should recall that the wake region is extended for  $H/\Delta = 0.22$  as seen in streamwise velocity profiles, which may result in the pattern in the spanwise velocity profiles to appear at a later section. It should be also noted that the velocity in the approaching flow at the height of the plate leading edge for the small gap case is lower as it is in the lower part of the boundary layer. Further details are provided in the forthcoming sections.

Some important observations can be drawn from the mean velocity profiles: (1) the large peaks tend to appear near the leading and trailing edges of the inclined plate, (2) more changes in the profiles tend to occur in the developed wake region ( $X/\Delta = 1.5$  and  $2.5$ ), (3) the spanwise velocity gradually decays above the trailing edge. Major variations in the spanwise velocity profiles are noticed behind the plate in both gap cases since these locations are in the wake region. The flow in the gap region is influenced by the wall especially in the smaller gap case.

In the small gap case, the presence of a strong streamwise velocity but small depthwise velocity provides for a wall-jet like flow in the gap region. In contrast, there is a strong upwash/downwash behind the inclined plate in the larger gap case which indicates that

the wake region is expanded depthwise. Thus, the flow underneath the inclined plate is strongly influenced by the wall for  $H/\Delta = 0.22$ . The numerical work of Lee et al. [50] suggested that there is a wall-jet like flow for  $H/\Delta = 0.5$  but the flow with  $H/\Delta = 0.6$  is different. A similar state seems to occur in the present flow field for the inclined plate where a wall-jet like flow is formed beneath the plate for the smaller gap and a strong upwash is observed for the larger gap.

Sectional streamlines based on mean velocities, superimposed with mean pressure contours, are shown in Figure 4.4. In this figure, X- and Y-direction are normalized by the projected height,  $\Delta$ . These plots show the presence of two large recirculation regions at the top and bottom edges of the inclined plate, having different sizes for each gap case. The lower recirculation region has a length of about  $3.6\Delta$  in the X-direction for  $H/\Delta = 0.22$  compared to  $2.8\Delta$  for  $H/\Delta = 1.11$ . The elongation of the region is due to the wall-jet like flow in the gap region for the small gap case as observed in Figure 4.3. However, it can be noted that the core of the top and bottom vortices are located around  $X/\Delta = 1.8$ . Moreover, there is also the formation of a separation region on the ground at  $X/\Delta = 3.8$  for  $H/\Delta = 0.22$ , which is a unique feature only observed for the small gap case. The pressure difference between the front and back of the plate is found to be greater for  $H/\Delta = 1.11$  than  $H/\Delta = 0.22$ , indicating that the bluff body is subjected to a larger wind load if it is positioned further from the wall. It is worth noting that the plate with  $H/\Delta = 1.11$  gap is also subjected to a higher incident velocity than the plate with  $H/\Delta = 0.22$  gap due to the atmospheric boundary layer.

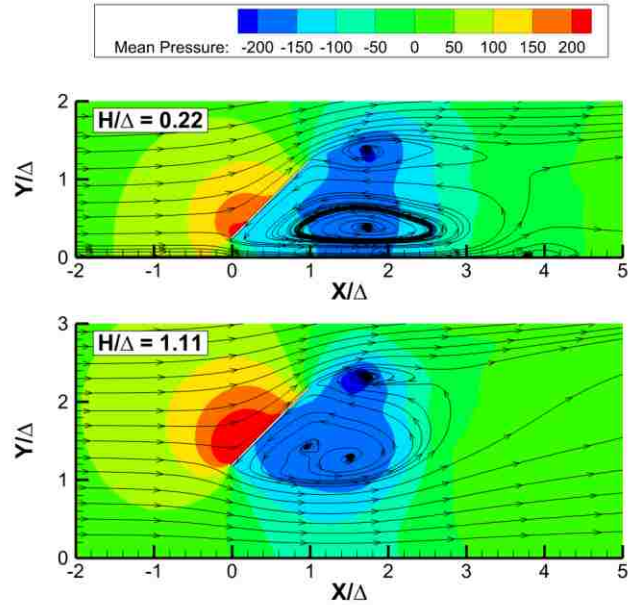


Figure 4.4: Mean velocity flow streamtraces on the central plane, superimposed with mean pressure (Pa) contours ( $H/\Delta=0.22$  and  $H/\Delta=1.11$ )

The streamtraces on YZ planes, superimposed with X-vorticity contours, are presented in Figure 4.5. The left column represents the flow with the smaller gap while the right column is for the larger gap. It should be noted that the positive X-axis is directed into the graphs; therefore, the positive X-vorticity (red) is in the clockwise direction whereas the negative vorticity (blue) is in the counter-clockwise direction. The flow pattern and vorticity patches under the bluff body at  $X/\Delta = 0.5$  (Figure 4.5a,e) are similar in both cases since the air above the inclined plate is pushed upward along the windward surface of the plate while the flow in the gap region is directed downwards due to flow separation. The streamtrace pattern extending from the side edges of the plate ( $Z/\Delta \approx 0.0$  and  $2.0$ ) appear parallel to the wall for the small gap case (Figure 4.5a), whereas it curls towards the wall for the larger gap case (Figure 4.5e). As seen in streamwise flow traces (Figure 4.4), larger space in the gap region produces strong downwash which draws surrounding fluid downwards, whereas the small gap region has limited space and tends to develop



into a wall-jet like flow in the streamwise direction. In Figure 4.5b,f, the vorticity patterns at  $X/\Delta = 1.5$  are similar near the top edges of the plate in both cases. However, the wall has a significant influence on the flow beneath the bottom edge of the inclined plate in the lower gap case. The flow in the near-wall region behind the plate is chaotic, similar to that observed in the spanwise velocity profile (Figure 4.3c), depicted by different sizes of vortices. Note that the range of the vorticity contours used in this figure is  $\pm 5.0 \text{ s}^{-1}$  which is one tenth compared to the vorticity magnitude contours on the XY planes [11]. The vortex directly behind the panel (white dashed-circle in Figure 4.5b,f) causes much of the variations observed earlier in Figure 4.3c. The locations of the peaks in the spanwise velocity profiles can be matched at the valleys of the vorticity contour patches. In Figure 4.5c,d,g,h, a pair of vortices is captured above the trailing edge of the plate for the larger gap and is symmetrically located about the central plane. This pair comes from the corner vortices and are traces of the legs of a hairpin-like vortex which was found in the earlier study [11]. On the other hand, this pair of vortices is not clearly visible in the small gap case.

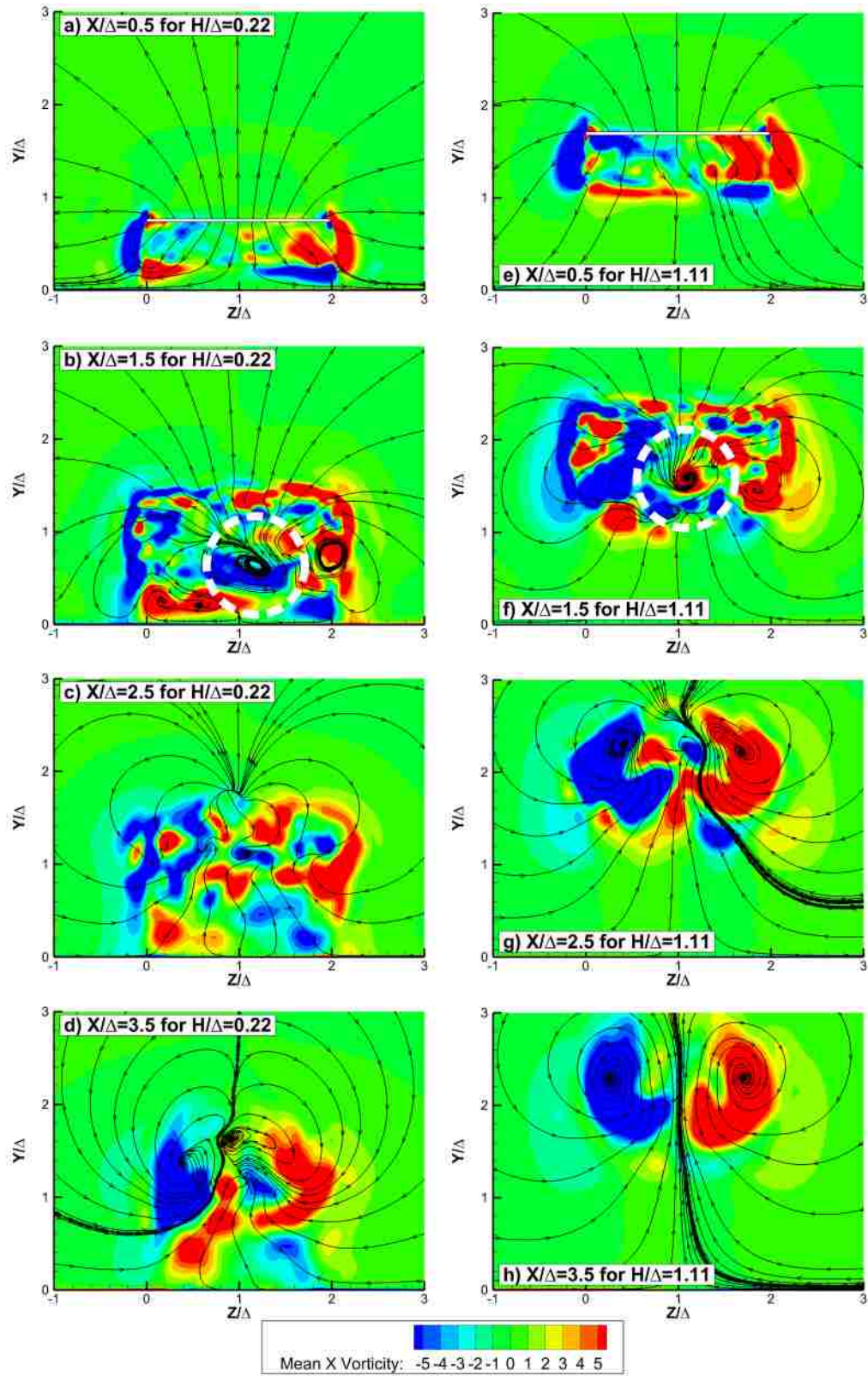


Figure 4.5: Streamtraces superimposed with X-vorticity contours on YZ planes at  $X/\Delta=0.5, 1.5, 2.5$  and  $3.5$  for  $H/\Delta=0.22$  (left) and  $H/\Delta=1.11$  (right)

In order to further investigate the flow field and evaluate the effect of the wall on the flow structures, the mean streamtraces and vorticity patterns are analyzed on various planes parallel ( $X$ -alternate or  $X_{Alt}$ ) and perpendicular ( $Y$ -alternate or  $Y_{Alt}$ ) to the inclined plate. These planes with the bluff body, shown in dashed line, are presented in Figure 4.6.

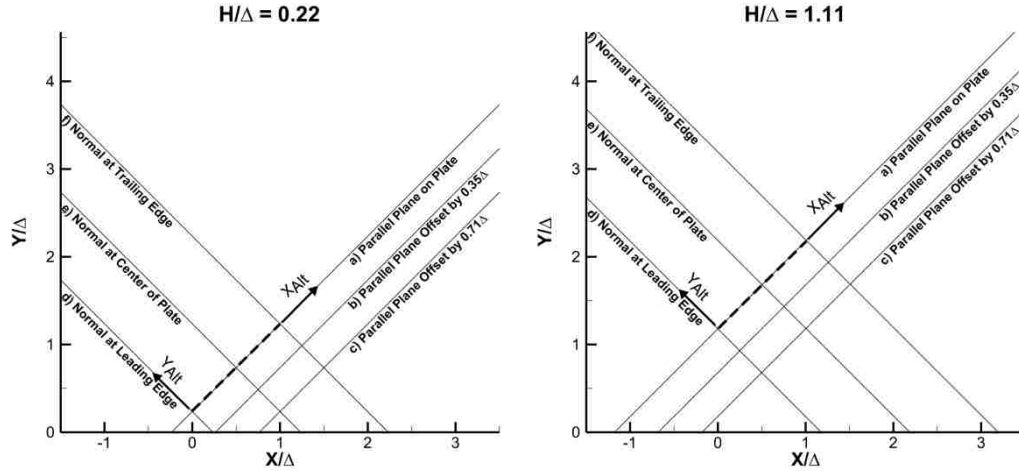


Figure 4.6: Definitions of axes and section planes parallel and normal to the inclined plate

Figure 4.7 and 4.8 present the results of projected streamtraces and vorticities onto the parallel and normal planes to the inclined plate. As defined in Figure 4.6, the leading edge of the plate is positioned at zero in the  $X_{Alt}/\Delta$  and  $Y_{Alt}/\Delta$  reference frame. It is noted that the colour contours of vorticity about the  $X_{Alt}$ -axis on the plane normal to the bluff body (Figure 4.8) is viewed from the negative  $X_{Alt}$ ; therefore, the positive vorticity (red) is in the clockwise direction and the negative vorticity (blue) is in the counter-clockwise direction. The contours on the parallel planes, however, are observed from the positive  $Y_{Alt}$ -axis and thus the vorticity is positive (red) if the flow is in the counter-clockwise direction and negative (blue) for the clockwise direction.

The flow patterns in the planes parallel and normal to the inclined plate show almost symmetry about the centre of the plate compared to that in the  $YZ$  planes. In Figure

4.7a,d, in which the parallel plane cutting through the bluff body, the streamtraces show similar flow patterns in both cases and the patches of vorticity contours are inflated towards the bottom corners on this sectional plane. In Figure 4.7b,e, the trends of the streamtraces and direction of flow near the top and bottom edges are an indication of the borders of the wake region behind the plate. For  $H/\Delta = 0.22$  (Figure 4.7b), the streamtraces show downward flow along the back of the inclined plate on this plane cutting through the wake region. The streamtraces continue to move outward from the bluff body near the bottom edge of the plate and merge with the shear flow at the sides. Similarly, the downward flow along the leeward of the plate is observed for  $H/\Delta = 1.11$  (Figure 4.7e) but the streamtraces curl inwards near the bottom edge. This difference of inward and outward flow near the bottom edge seems to be connected with the observations in Figure 4.5a,e, in which the streamtraces from the side edges are parallel to the wall for  $H/\Delta = 0.22$ , whereas the streamtraces are curled downwards for  $H/\Delta = 1.11$ . The bottom tips of vorticity contours at the side extend towards the centre line of the panel ( $Z/\Delta \approx 1.0$ ) as the streamtraces are curled inwards near the bottom edge for  $H/\Delta = 1.11$ , whereas a large area of weak vorticity is detected along the bottom edge for  $H/\Delta = 0.22$  indicative of the wall-jet like flow in the gap. In Figure 4.7c,f, two vortices near the top corners are identified for both cases. These may be considered as part of the corner vortices or part of the pair of vortices captured in Figure 4.5d,h.

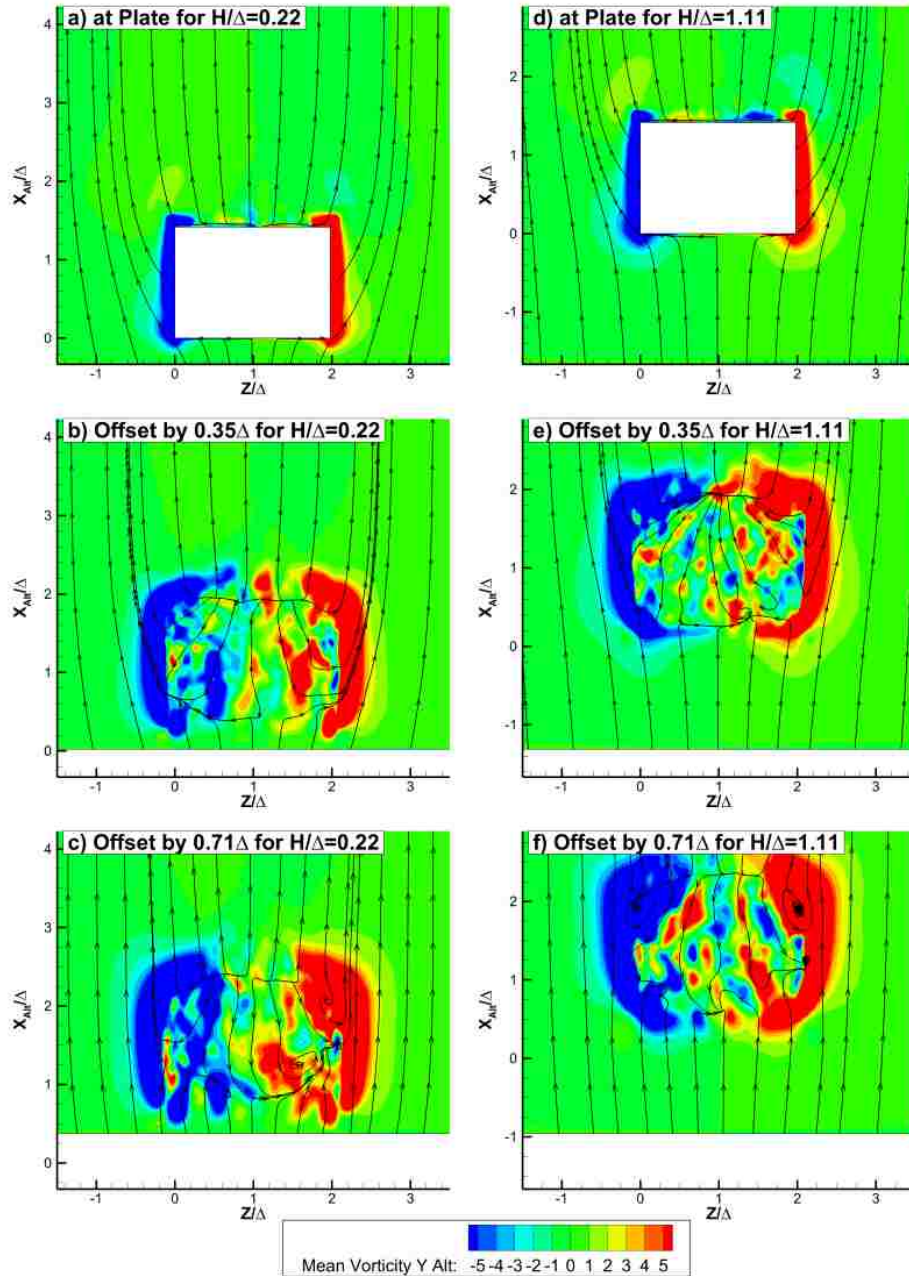


Figure 4.7: Streamtraces and vorticity contours on planes parallel to inclined plate for  $H/\Delta=0.22$  (left) and  $H/\Delta=1.11$  (right)

The streamtraces in the normal plane at the leading edge do not show any flow disturbance since it does not cut through the wake region (Figure 4.8a,d). The stagnation point on the windward surface and the separations of the flow at the side edges are clearly identified in the plots on the normal planes (Figure 4.8b,c,e,f). There is no significant

difference detected in lateral size of the wake region, unlike the elongation observed in the downstream due to the wall-jet like flow in the gap region for  $H/\Delta = 0.22$ . However, the size of the vorticity patches extending from the side edges is found to be larger for  $H/\Delta = 1.11$ . Small vorticity patches are spotted behind the plate for  $H/\Delta = 0.22$  (Figure 4.8c) whereas the two large patches are attached to the back of the bluff body for  $H/\Delta = 1.11$  (Figure 4.8f). The small scattered vortices may be the result of the flow disturbances due to the wall.

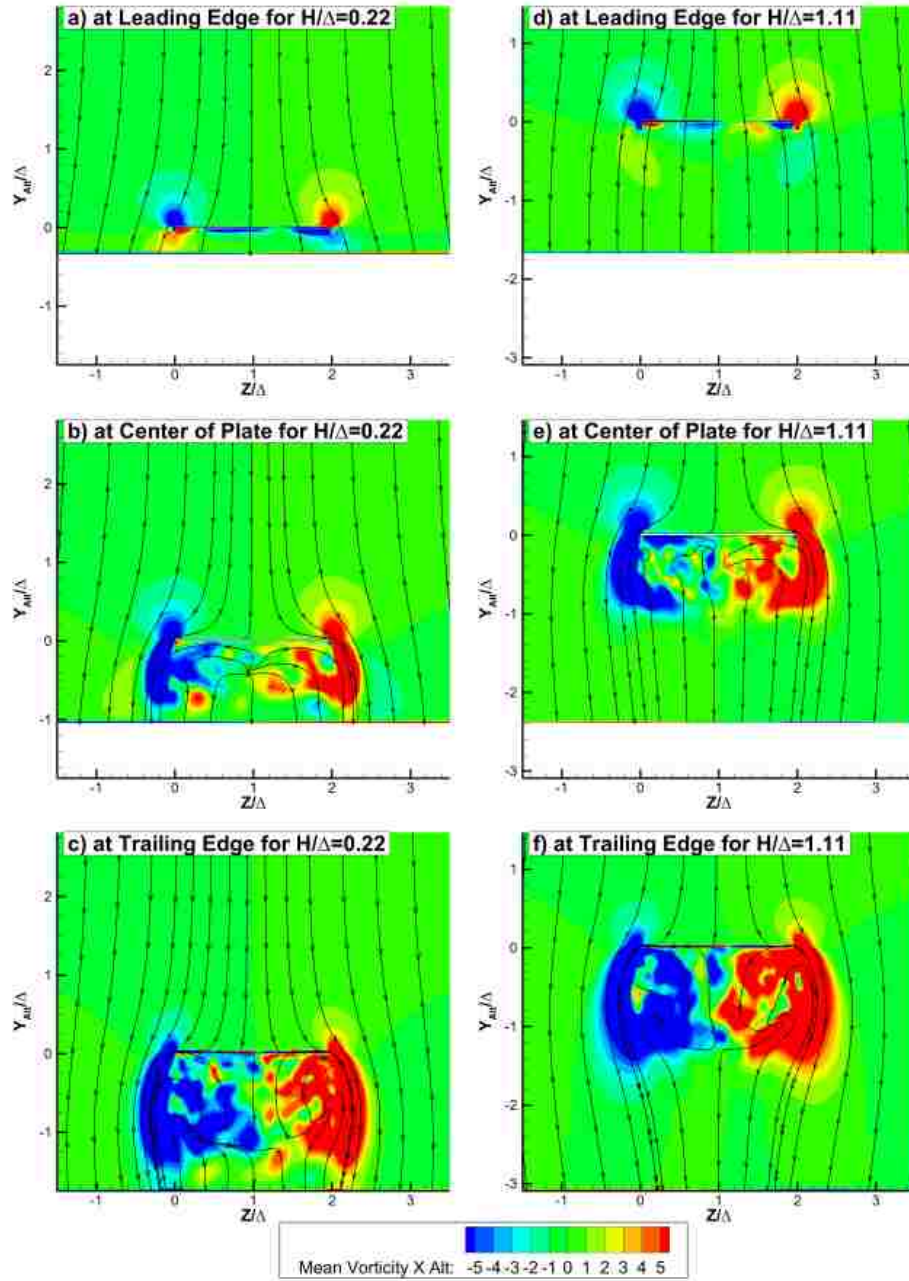


Figure 4.8: Streamtraces and vorticity contours on planes normal to inclined plate for  $H/\Delta=0.22$  (left) and  $H/\Delta=1.11$  (right)

## 4.4. Transient flow structure analysis

### 4.4.1. Transient flow analysis on the central plane

The mean flow characteristics illustrate the influence of the wall for the small gap case. The flow develops into a wall-jet like flow in the gap region, stretching the wake region in the downstream direction and showing the presence of a weak upwash.

In this section, the instantaneous flow development during early stages of the flow is first discussed. For simplicity, the flow field in the central plane is analyzed using the velocity vector plot superimposed with  $Z$ -vorticity. Selected instances of flow in the early development stage are shown in Figure 4.9a–c for  $H/\Delta = 0.22$  and Figure 4.9d–f for  $H/\Delta = 1.11$ . The insets in these figures illustrate the flow field in the near-wall region.

There are two vortices shed from the leading and trailing edges of the inclined plate. For the smaller gap case, Figure 4.9a ( $t = 0.1$  s) shows that the vortex departing from the leading edge touches the wall and generates a counter-rotating flow as indicated by the negative  $Z$ -vorticity patch. In the two later time steps ( $t = 0.13$  s and  $0.16$  s, insets in Figure 4.9a), the patch (blue) is ejected into the back of the bluff body. The counter-rotating sheared vortex on the wall was also reported by Bosch et al. [46]. Similar events occur repeatedly as the vortices shed from the leading edge travel farther downstream. After the bottom shed vortices reach a certain distance in the downstream direction, the counter-rotating vortices (blue) no longer rise upward but are pushed downstream along the wall (Figure 4.9b). These patches are very similar to the traces of meandering vortices captured by Shademan et al. [11]. The shed vortex from the bottom edge continues stretching downstream up to  $X/\Delta \approx 3.0$  (Figure 4.9c) where the upwash flow near the wall



is observed in the mean normal velocity profile (Figure 4.3b). For  $t > 2.0$  s, the weak bottom vortices are shed periodically and the associated counter-rotating vortex patches are also pushed downstream, and the flow is considered to have reached a fully developed state around the body.

For the larger gap, the vortex at the leading edge shifts downwards but does not interact directly with the wall (Figure 4.9d–f). Unlike the smaller gap case, this vortex gets trapped and is not shed into the downstream flow. A strong upwash is observed after the recirculation region ( $1.5 < X/\Delta < 2.0$ ) in the larger gap case (Figure 4.9e), whereas a weak backward flow is captured in the small gap case (Figure 4.9b). Due to the lack of a strong upward flow, the bottom shear layer is almost parallel to the wall at  $t = 2.26$  s for  $H/\Delta = 0.22$  (Figure 4.9c) but has a downward bow shape at a similar time for  $H/\Delta = 1.11$  (Figure 4.9f). The vortices shed from the trailing edge are pushed higher for  $H/\Delta = 1.11$  due to this strong upward flow (Figure 4.9e,f), whereas the trailing edge vortices do not rise much for  $H/\Delta = 0.22$  (Figure 4.9b,c). These observations are concomitant with the results for the mean flow characteristics.

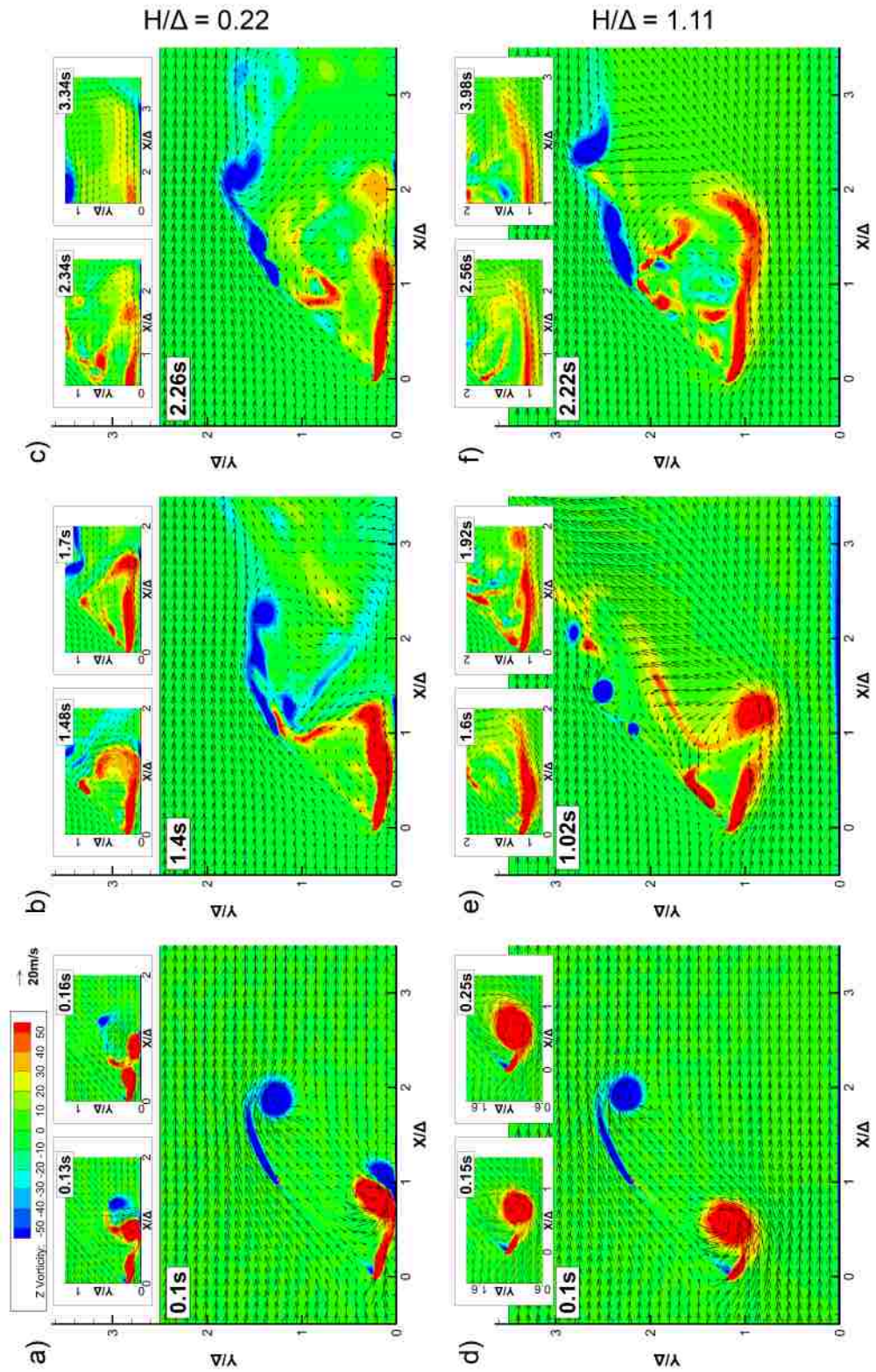


Figure 4.9: Instantaneous velocity vector field superimposed with Z-vorticity at early flow development stage: (a-c)  $H/\Delta = 0.22$ , and (d-f)  $H/\Delta = 1.11$

#### 4.4.2. Three-dimensional transient flow analysis

In this section, we focus on the development of the flow structures and explore the differences in three-dimensional structures between the two gap cases. To understand the difference in development of the flows, the flow field is analyzed from the start of the motion and the evolution of vortices is tracked around the bluff body. The analysis presented up to this point clearly indicates that the flow behind the inclined plate is highly complex with formation of vortices of different sizes around the plate. To illustrate these vortices, iso-surfaces of  $\lambda_2$  are generated with the  $\lambda_2/\lambda_{2\min}$  value of 0.01. The iso-surfaces are coloured by the Y-vorticity contour.

##### 4.4.2.1. Early stage flow development

Figure 4.10 illustrates the fluid structures around the inclined plate for  $H/\Delta = 0.22$  from four different views, where the elapsed time is 0.16 s after the start of the flow. This time instance was arbitrarily chosen in order to provide a representative description of the structures generated. There are four main structures identified in these figures and labelled as Structures 1 through 4. Structure 1 is a hairpin-like vortex, which was also observed by Shademan et al. [11]. There is a similar inverted hairpin like vortex formed at the bottom of the plate, which is labelled as Structure 2. This structure detaches from the leading edge and is convected downstream. A pair of vortex tubes (labelled as Structure 3) extends vertically upwards from the wall and bends around Structure 2. This is a unique feature only observed in the small gap case, which will be discussed in more detail later in this section. Lastly, there are vortex tubes which are corner vortices, stretching from the top corners of the inclined plate and wrapping around the hairpin-like

vortices (Structure 4). In the previous study, Structures 2, 3 and 4 were not clearly identified in the fully developed stage.

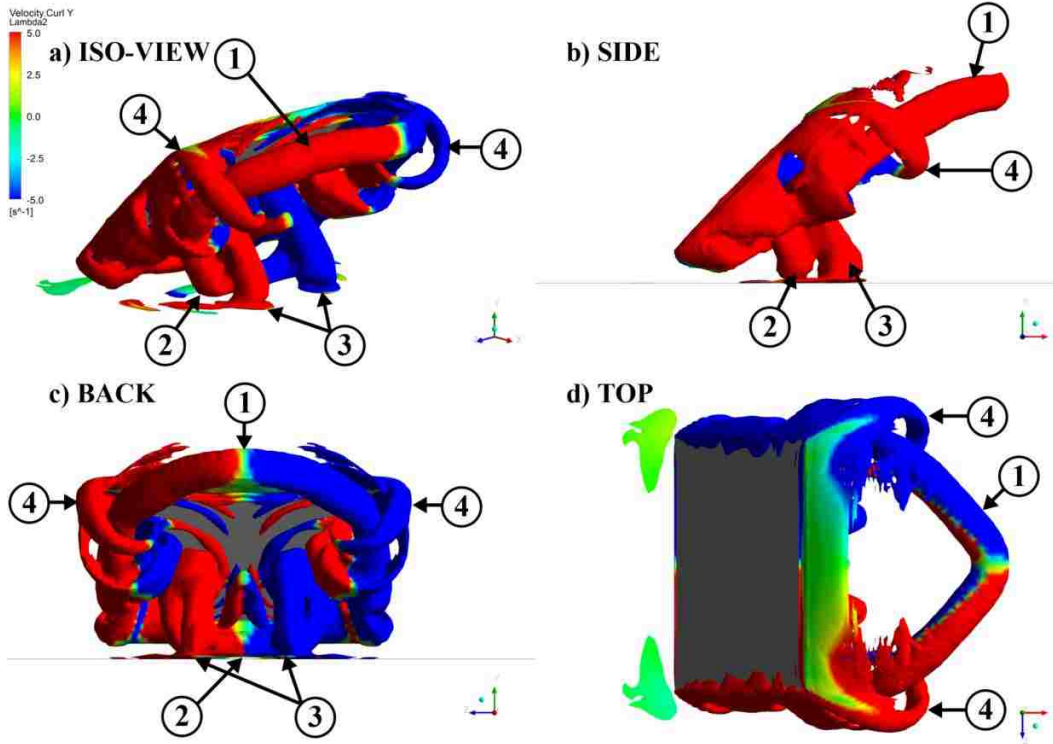


Figure 4.10: Identification of flow structures around the inclined plate with  $H/\Delta = 0.22$  gap after 0.16 s: (1) hairpin-like vortex, (2) inverted hairpin-like vortex developed at the leading edge, (3) a pair of vortices extending from the wall, and (4) corner vortices

Figure 4.11 shows the history of the flow development for each gap (left:  $H/\Delta = 0.22$ , right:  $H/\Delta = 1.11$ ). At  $t = 0.05$  s (Figure 4.11a), both cases show the formation of vortex tubes at all four edges of the inclined plate, similar to that observed in the study by Higuchi et al. [52]. Downstream, these vortices further grow and deform into a bow shape. One may recall that the counter-rotating vortex (see blue patch in Figure 4.9a) which develops on the wall (labelled as 3' in Figure 4.11a) interacts with the vortex shed from the leading edge (Structure 2 in Figure 4.11a). Structure 3' along the wall shows red and blue colours at both ends, indicate flow rotating inwards to the wake region. As Structure 2 approaches the wall, it interacts with the wall vortex and lifts the vortex

upwards. Simultaneously, the flow separating from the side edges of the inclined plate further interacts with Structure 3'. As the fluid structures interact with each other, Structure 3' is split into three pieces: two end pieces (indicated as 3'' in the inset at  $t = 0.09$  s) and a middle section. The end pieces eventually become a pair of vortex tubes identified as Structure 3 in Figure 4.10 and also observed at  $t = 0.15$  s in Figure 4.11b for the smaller gap case. The central portion of Structure 3', on the other hand, gets bent as it is trapped by the bottom vortex and the central portion of Structure 3' is finally ejected into the wake region as observed in Figure 4.9a. It is also noticed that the hairpin-like vortex at the trailing edge merges with the corner vortices from the sides and forms a top-half vortex ring, whereas the inverted hairpin-like vortex does not become a part of the ring. At  $t = 0.55$  and  $1.55$  s, the hairpin-like vortices and bottom vortex tubes are clearly observed and are shed periodically in the larger gap case (Structures 1.1 through 1.4 and 2.1 through 2.2). On the other hand, distorted vortices that form behind the plate are captured in the small gap case. The ligaments of vortices stretching on the wall in the streamwise direction at  $t = 1.55$  s are captured only in the small gap case. These ligaments have near zero vorticity about the Y-axis (mostly shown as green patches), which indicates that the ligaments are captured due to the rotation either about the X- or Z-axis. To determine the orientation of the ligaments of vortices, the iso-surfaces of  $\lambda_2$  coloured by X-vorticity component are presented in Figure 4.12. As expected, the ligaments are displayed in red and blue colours which imply that the dominant flow orientation of these ligaments is about the X-axis. From this figure, it can also be noted that the orientation of the ligaments is opposite to the legs of the hairpin-like vortex. For instance, the left (in positive Z-axis) leg of the hairpin-like vortex is coloured in red,

meaning the leg is rotating counter-clockwise about the X-axis, whereas the ligament below the left leg is coloured in blue, indicating clockwise rotation about the X-axis. As a result, it can be said that the ligaments and legs of the hairpin-like vortex are a pair. One of the reasons that the ligaments of vortices form on the wall is because the hairpin-like vortices do not stretch upward in the small gap case. This is due to the wall-jet like flow in the gap region that weakens the upwash and the legs of the hairpin-like vortices extend almost parallel to the wall. Thus the ligaments are developed on the wall as the legs of the hairpin-like vortex get close to the wall. In the larger gap case, in contrast, the hairpin-like vortices stretch upward as a result of a strong upwash.

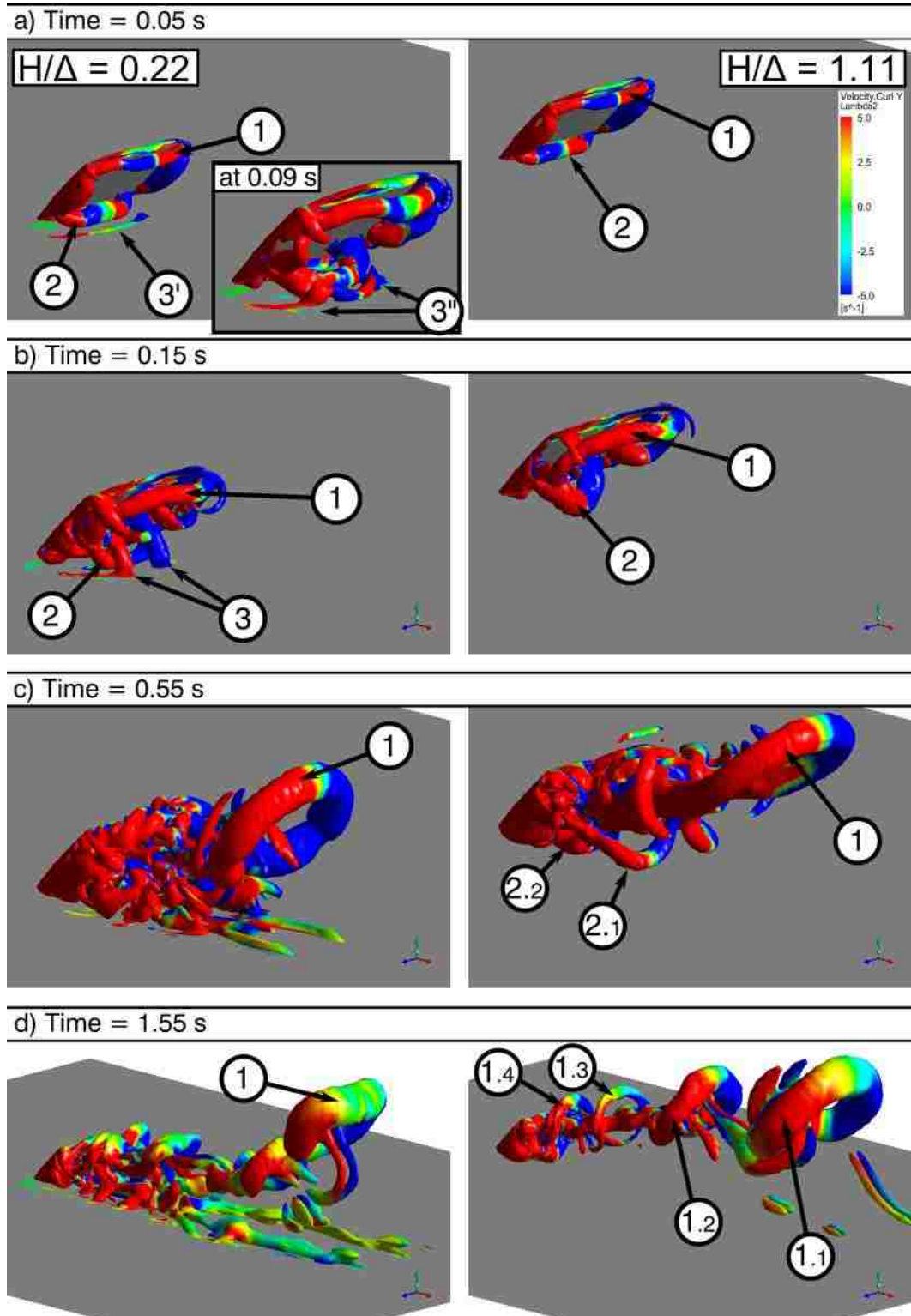


Figure 4.11: Early stage flow structures development around the inclined plate for  $H/\Delta = 0.22$  (left) and  $H/\Delta = 1.11$  (right)

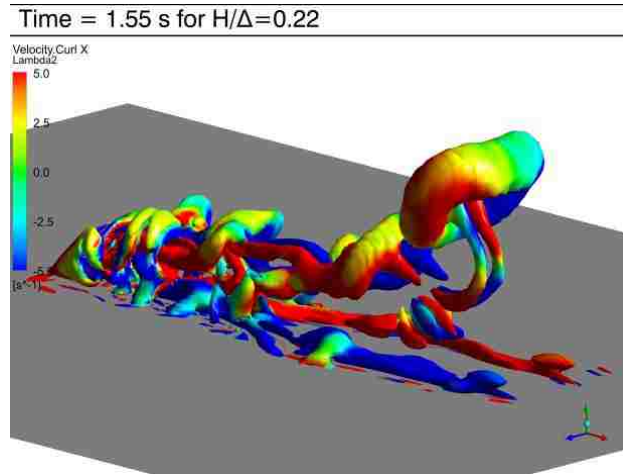


Figure 4.12: Iso-surfaces of  $\lambda_2$  at  $t = 1.55$  s for  $H/\Delta = 0.22$ , with the contours of X-vorticity on the surfaces

Shademan et al. [11] plotted the vorticity magnitude contours on the horizontal plane at  $Y/\Delta = 0.05$  to illustrate patches of shear flow and the presence of meandering structures. To further explore the role of these structures, the image from the bottom view is filtered to remove the structures above the gap by setting a gray colour plane at  $Y/\Delta = 0.22$  (the height of the leading edge for  $H/\Delta = 0.22$ ) so that only the structures within the gap region will be visible (Figure 4.13, right column). It is noted that the positive Y-axis extends into the paper in these figures. Thus, the positive Y-vorticity is in the clockwise direction. At  $t = 2.0$  s, the ligaments identified in the early stage ( $t = 0.55$  s and  $1.55$  s in Figure 4.11), shown to the right of the dashed line in Figure 4.13a, are symmetric and the small vortex tubes, similar to the vertical vortex tubes labelled as Structure 3 in Figure 4.13, are captured behind the inclined plate (L1, R1, etc. in Figure 4.13). These pairs of vortices start to lose their symmetrical feature farther downstream at  $t = 2.4$  s (Figure 4.13b). Therefore, the source of the meandering footprints observed by Shademan et al. [11] is likely the result of the same mechanism as the pair of vertical vortex tubes shed from the body. Eventually, by examining the meandering vortices at  $t = 2.6$  s, it appears that the flow has reached a fully developed and periodic stage (Figure 4.13c).



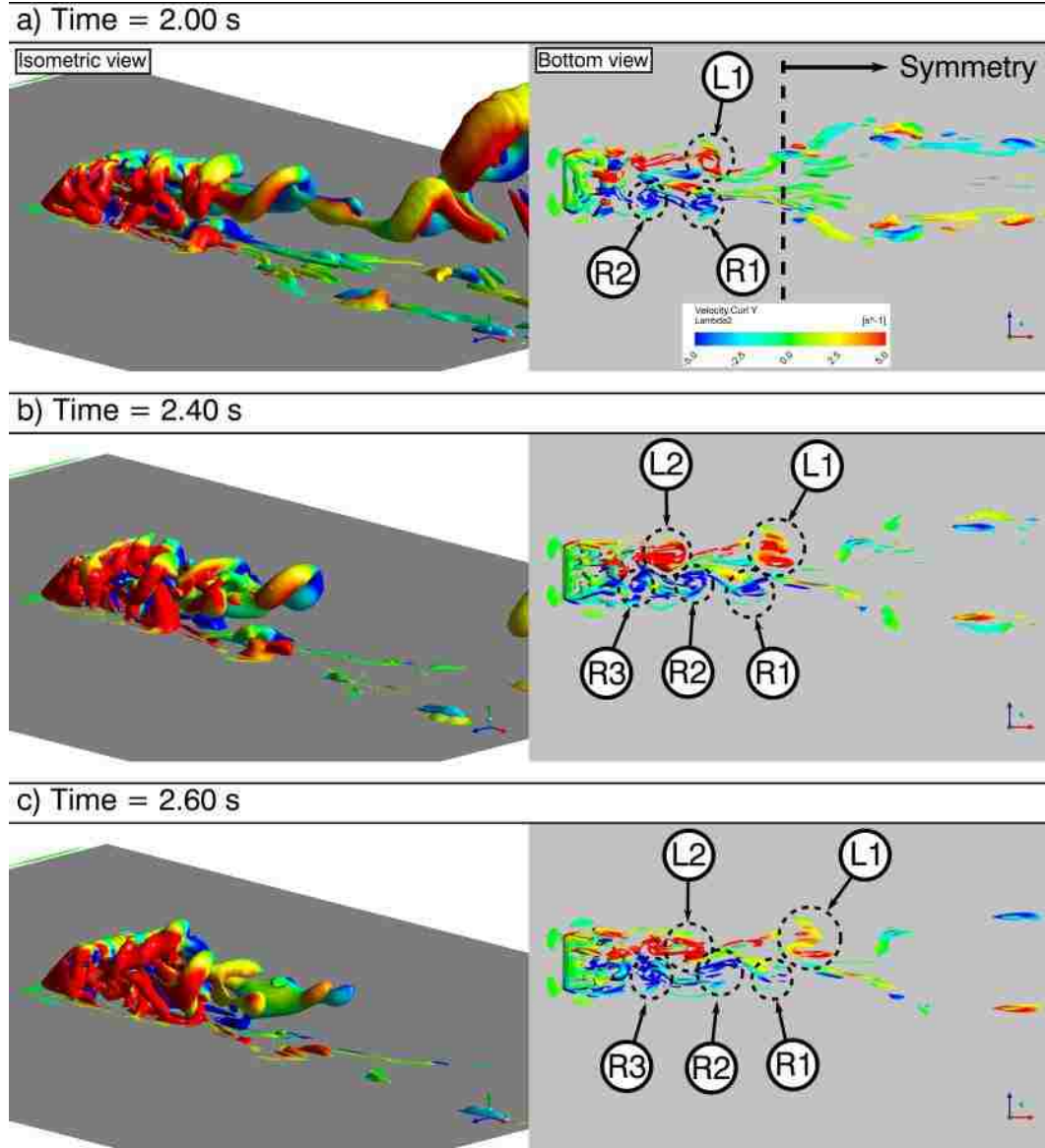


Figure 4.13: Iso-view of the iso-surfaces of  $\lambda_2$  with the contours of Y-vorticity on the left, and a bottom view of the same structures with the filtering plane set at  $Y/\Delta = 0.22$  on the right ( $H/\Delta = 0.22$ )

#### 4.4.2.2. Steady state condition in the mean

After confirming the flow has achieved a stage of steady state condition in the mean, the iso-surfaces of  $\lambda_2$  at  $t = 5.6$  s are presented in Figure 4.14. As observed in the developing stage, the flow structures in the larger gap case continue to maintain symmetry about the central plane, whereas the structures in the small gap case are completely distorted. The tip vortices that were captured by Jubayer and Hangan [9] using the spanwise vorticity

iso-surface are not identified by the transient flow development using the  $\lambda_2$ -criterion, which may be due to the difference in inclination angle of the plate. The same bottom view of the  $\lambda_2$  iso-surface illustrated in Figure 4.13 is presented in Figure 4.15a at  $t = 5.6$  s, and the Y-vorticity contours are illustrated on the plane at  $Y/\Delta = 0.05$  for the same instance (Figure 4.15b). In Figure 4.15b, it is clearly seen that the meandering nature is captured. However, some of the structures farther downstream are not captured by the  $\lambda_2$ -criterion with  $\lambda_2/\lambda_{2min}$  of 0.01, as highlighted by the dashed circle in Figure 4.15a. Nevertheless, they are still identifiable in the Y-vorticity contour plot in Figure 4.15b. These structures can be made visible using lower  $\lambda_2/\lambda_{2min}$  value (e.g.  $\lambda_2/\lambda_{2min} = 0.005$ ) but lowering the value of  $\lambda_2/\lambda_{2min}$  introduces excessive structures around the bluff body and disturbs the visibility of the main structures.

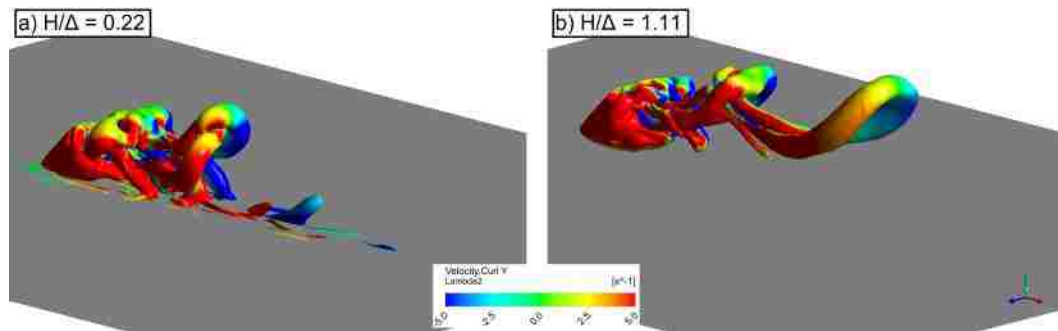


Figure 4.14: Iso-surfaces of  $\lambda_2$  at  $t = 5.60$  s with the contours of Y-vorticity on these surfaces for  $H/\Delta=0.22$  (left) and  $H/\Delta=1.11$  (right)

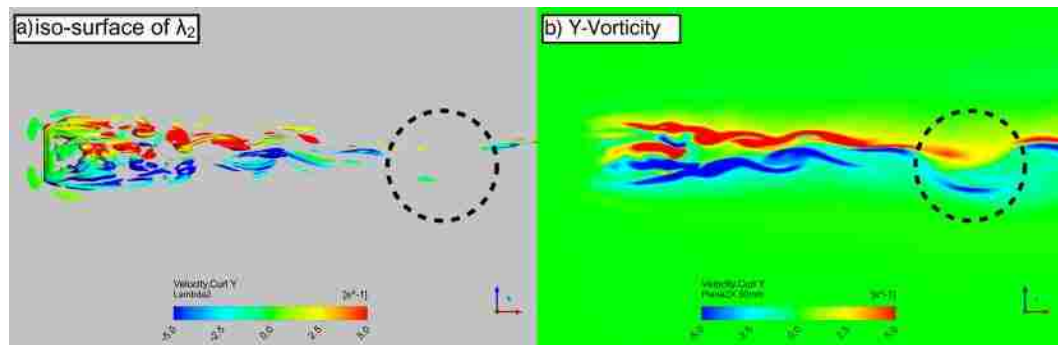


Figure 4.15: Bottom view of iso-surfaces of  $\lambda_2$  with Y-vorticity contours on its surfaces (left) and the same view of Y-vorticity contours on XZ plane at  $Y/\Delta = 0.05$  (right) after  $t = 5.60$  s in the  $H/\Delta=0.22$  gap case

## 4.5. Conclusions

The effect of the gap between an inclined plate and a wall is investigated numerically. DES is used to simulate the unsteady flow passing over the bluff body set at two different gaps. The simulation domain is initialized with a zero velocity flow field so that flow development at the early stage can be captured. The flow field in different planes were analysed to visualize the structures formed around the plate.

Mean streamwise velocity profiles show a wall-jet like flow underneath the plate at a small gap clearance of  $H/\Delta = 0.22$  with a weak upwash in the downstream due to the wall effect. Two-dimensional streamtrace plots indicate that the wake region is extended in the streamwise direction. On the other hand, the flow past the plate at  $H/\Delta = 1.11$  shows the presence of a strong upwash behind the bluff body. As a result, the wake is smaller. The effect of upwash is also seen in the three-dimensional flow visualization.

Transient flow structure development is investigated using velocity vectors and vorticity contours on the central plane. These flow parameters show the interaction of the vortex shed from the leading edge of the inclined plate near the wall. During the flow developing stage the counter-rotating vortex generated by the shedding vortex is observed at the wall and is trapped into the wake region by the shedding vortex as it develops. Once the flow reaches the steady state condition in the mean the counter-rotating vortex eventually stays on the wall as the shedding vortex stretches into the downstream. The shear layer at the leading edge appears parallel to the wall for  $H/\Delta = 0.22$  due to the wall-jet like flow in the gap region, whereas the layer arches downward due to strong downwash and upwash for  $H/\Delta = 1.11$ .

The iso-surfaces of  $\lambda_2$  are capable of elucidating the hairpin-like vortex in the downstream region at the early stage of flow development in both cases; however, the legs of the hairpin-like vortex for  $H/\Delta = 0.22$  are almost parallel to the wall whereas those for  $H/\Delta = 1.11$  are stretched upwards. This provides further evidence of the low lift force on the inclined plate in the smaller gap case which was discussed by Shademan et al. [11].

There are three other flow structures in addition to the hairpin-like vortex formed at the early stage of flow development: an inverse hairpin-like vortex tube developed at the bottom leading edge, a pair of vortices extending vertically up from the wall, and corner vortices. The pair of vortices are a unique structure which can only be detected in the  $H/\Delta = 0.22$  case. This pair of vortices is generated by the combination of the vortex shed from the bottom leading edge and flow separating from the side edges of the plate. Over the period of flow development, these vortices travel downstream in parallel but start to be misaligned from each other, eventually creating a meandering pattern.

At the steady state condition in the mean, the three-dimensional flow structures captured by the iso-surface of  $\lambda_2$  show clear distortion of the flow for the small clearance case whereas the symmetry of the structures is maintained for the large gap. In the far downstream, the meandering patterns are not identified by the iso-surface of  $\lambda_2$ . Nevertheless, the Y-vorticity contours on the plane near the wall are able to picture the footprints. The  $\lambda_2$ -criterion is capable of capturing the flow structures at a certain level but it may lose track of weak vortices. However, selecting a higher  $\lambda_2$  value (closer to zero since  $\lambda_2$  is negative) may introduce superfluous flow structure in the domain of the interest.

## **Chapter 5. Analysis of flow structures around a stand-alone solar panel**

### **5.1. Introduction**

The study of flow past a finite inclined flat plate near a wall often focuses on the effect of the gap between the bluff body and wall. The formation of a wall-jet like flow in the gap promotes expansion of the wake in the downstream, which reduces the wind load on the body. The wall-jet like flow also generates meandering vortical structures along the wall. The mechanism that drives the meandering structures along the wall is the interaction of the wall with the inverted hairpin-like vortices shed from the leading edge and the flow separating from the side edges of the body. In real-life application of stand-alone solar panels and/or an experimental setup, a supporting structure is present underneath the bluff body; thus the overall flow field is expected to get distorted by the support.

One of the stand-alone solar panels studied by Shademan and Hangan [2], Shademan and Hangan [53] has an adjustable rack system supporting the solar panel. The supporting frame was extended from the side edges of the solar panel, which was included in the simulations. These studies focused on the wind loading for different inclination angles of the panel and different wind directions using steady Reynolds-Averaged Navier-Stokes (RANS) simulations. However, the influence of the frame structure on the flow around the body was not considered in their work.

Abiola-Ogedengbe et al. [54] conducted experiments to measure the pressure distribution along a large stand-alone solar panel which was supported by three legs positioned at the

centre and near the edges. An experimental and numerical study of flow past the same geometry was also conducted by Jubayer et al. [10] and Jubayer and Hangan [9]. The fields-of-view for particle image velocimetry (PIV) measurements was set between two legs and shifted along the windward and leeward of the solar panel for four different approaching flow directions. The flow around the supports and their contribution (if any) to the pressure distribution was not analyzed in these studies.

Aly and Bitsuamlak [63] studied the scale effects on wind loads along a stand-alone solar panel with fixed trapezoidal supports. The mean velocity contours were presented, but there was no discussion about the influence of the supporting structures.

The majority of studies on flow past a stand-alone solar panel have focused on forces acting on the body and discussions on supporting structures have been largely avoided, at least partially due to the limitations of experimental facilities. In numerical studies, the supporting structures have been simplified or removed due to the complexity of modeling the actual geometry. The field-of-view of interest in the subsequent flow analysis was taken far enough away from the supporting structures to justify neglecting the flow disturbance due to the supports. As seen in the work of Shademan et al. [11], the characteristics of the flow field behind the panel have a major impact on the wind load acting on the inclined flat plate. Therefore, it is reasonable to expect that the supporting structure would also influence the forces on the body if it creates any changes in the flow behind the panel. To further investigate the influence of the supporting structure and its interaction with the gap flow between the solar panel and wall, numerical simulations of a finite inclined flat plate with a circular cylinder post is studied in this chapter. Similar to the previous chapters, mean flow characteristics are analyzed and compared with the case

without a supporting structure. Then, the early stage development of the transient three-dimensional fluid structures are studied by identifying the vortical structures using the  $\lambda_2$ -criterion.

## **5.2. Methodology**

### **5.2.1. Geometry setup**

The geometry tested in this chapter includes a cylindrical support for the finite inclined flat panel near a wall that was analyzed in Chapter 4. The dimensions of the inclined flat plate are the same as that of Shademan et al. [11]. Figure 5.1 shows the dimensions of the flat plate: 4.2 m long (L), 3.2 m wide (b) and 0.05 m thick plate set to an angle of  $\phi = 135^\circ$  from the horizontal plane with respect to the upwind direction (Figure 5.1a). The circular cylinder support for this study has a 0.15 m diameter (D), which is the size typically used in a general top of pole mount for the above size stand-alone solar panel [64]. The gap heights (H) are the same as in Chapter 4, i.e., 0.5 m and 2.5 m. In this study, all the dimensions are normalized by the projected height of the inclined plate,  $\Delta = b \cdot \sin(\pi - \phi)$ , and as a result the normalized gap heights are identified as  $H/\Delta = 0.22$  and 1.11 for gap heights  $H = 0.5$  m and 2.5 m, respectively. The computational domain is chosen to match the recommendation of Franke et al. [42], which requires that the area blockage ratio of the plate should be less than 3% (Figure 5.1b).

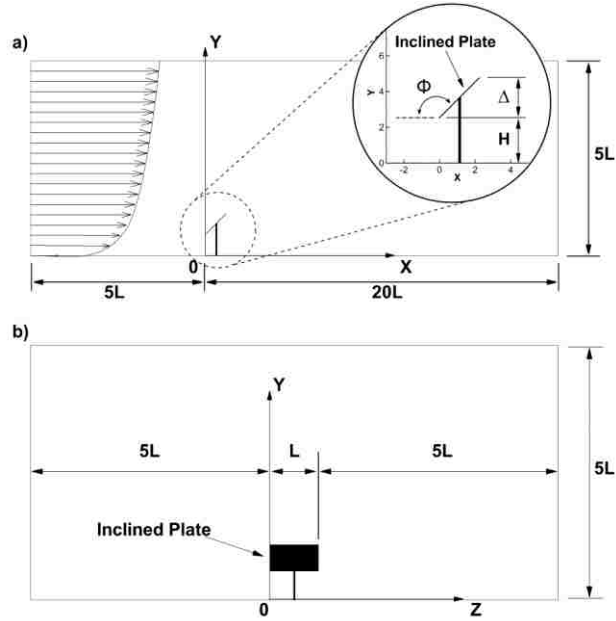


Figure 5.1: Dimensions of calculation domain, a) side view and b) view from the inlet

As in Chapter 4, the approaching flow velocity profile at the inlet boundary is fit to a power-law equation:

$$\frac{U(Y)}{U_g} = \left(\frac{Y}{y_g}\right)^\alpha \quad (50)$$

where  $U_g$  is the geostrophic wind velocity,  $Y$  is the distance from the ground,  $y_g$  is the atmospheric boundary layer height in an open terrain ( $y_g = 300$  m) and the exponent  $\alpha$  is dependent on the type of terrain ( $\alpha = 0.16$ ) [57]. The design wind velocity at 10 m above the ground is set to 25 m/s based on the 1-in-30-year hourly wind speeds at Windsor, Ontario, defined in the National Building Code [56]. The reader is referred to Section 4.2.1 in Chapter 4 for verification of the inlet velocity profile. In addition to the boundary conditions listed in Chapter 4, the cylindrical post is a no-slip wall. The commercial CFD software ANSYS Fluent 15.0 is used to conduct the numerical studies of the current problem.



The mesh employed in Chapter 4 is further refined in the regions surrounding the flat plate and post using hexahedral cells. The mesh is clustered towards the plate, post and bottom wall to capture the high shear stresses in these boundary layer regions. The first grid size next to the boundaries is set to ensure that  $y^+ < 1$ , where  $y^+$  is the non-dimensional normal wall distance defined as  $y^+ = (u_\tau \cdot y)/\nu$  with friction velocity,  $u_\tau$ , as  $u_\tau = \sqrt{\tau_w/\rho}$ . In these expressions,  $y$  is the normal distance from the nearest boundary,  $\nu$  is the kinematic viscosity,  $\tau_w$  is the wall shear stress and  $\rho$  is the air density. This grid clustering produces 5.92 million cells for the small gap case and 6.79 million cells for the larger ground clearance.

### **5.2.2. Governing equations**

The system of governing equations used in the current chapter is the same as in Chapter 3 and 4. Transient Navier-Stokes equations are solved using the finite volume method and a second-order upwind scheme is used for discretization of the convective derivatives [13]. Time discretization is second-order implicit time marching. The time-step size is set to 0.1 ms so that the Courant number remains close to unity ( $CFL < 1.0$ ). The SIMPLE algorithm is used for pressure and velocity coupling. Detached Eddy Simulation (DES) is also used for the turbulence model in this study [17, 43, 44]. Further details of the governing equations are discussed in Chapter 2.

### **5.3. Mean flow analysis**

In this section, the mean flow properties are compared for the inclined flat plates with and without a supporting structure. Time-averaged flow variables are quantified by taking three-second sampling after the flow achieves a steady state condition in the mean of pressure on the flat plate. The three components of mean flow velocity are plotted at

multiple stations in the downstream:  $X/\Delta = 0.5, 1.5, 2.5$  and  $3.5$ , where  $X/\Delta = 0.0$  is the leading edge of the plate and  $X/\Delta = 1.0$  is the trailing edge. An  $XY$  plane at the midspan of the plate is used to present the mean pressure field superimposed with the streamtraces of the mean flow field. Transverse cross-sections are also generated to show the space evolution of the streamwise vortical structures using streamwise vorticity contours and streamtraces on the sections.

Figure 5.2, 5.3 and 5.4 show the mean streamwise velocity,  $\bar{U}$ , depthwise velocity,  $\bar{V}$ , and spanwise velocity,  $\bar{W}$ , normalized by the velocity of the approaching flow at the height of the leading edge,  $U_0$ . Since the gap heights are different for each case, it is difficult to compare the flow in the gap region if the lengths are normalized by a single characteristic length, such as  $\Delta$ . Therefore, the wall normal ( $Y$ ) direction is split into two regions based on the characteristic length: namely the gap and upper regions. The gap region ( $0.0 \leq Y \leq H$ ) is normalized by the gap height,  $H$ , whereas the upper region ( $Y \geq H$ ) is normalized by the projected height of the solar panel,  $\Delta$ . For convenience, the newly defined wall normal coordinate is labelled as  $Y^*$ . In this new coordinate, the leading and trailing edge of the plate are identified at  $Y^* = 1.0$  and  $2.0$ , respectively. In the figures, the small gap cases ( $H/\Delta = 0.22$ ) are labelled with a circle ( $\circ$ ) without the post and with a diamond ( $\diamond$ ) with the post. The large gap cases ( $H/\Delta = 1.11$ ) are identified with a cross ( $\times$ ) for no post and with a square ( $\square$ ) with the post. Note that the post is located at  $X/\Delta = 0.5$  in the current study; thus, there is no data available from the wall up to the windward surface ( $0.0 < Y^* < 1.5$ ) of the plate for the case with post.

For  $H/\Delta = 0.22$ , as observed in the previous chapter, a wall-jet like flow formed in the gap region as the peak of streamwise velocity is identified near the wall (Figure 4.3a)

while weak depthwise velocity is captured in Figure 5.2b. There is a small upward shift in the streamwise velocity profile above the trailing edge ( $Y^* > 2.0$ ) from  $X/\Delta = 1.5$  through 3.5 compared to the case without the post. Meanwhile, a slight reduction in the streamwise velocity is observed in the gap region at the same stations (Figure 5.2a,ii-iv). Even though the differences are small, the flow at the central plane is blocked by the post; therefore, the flow loses momentum in the gap region which results in a slightly weaker wall-jet like flow. Recall that, without the post, the wake was stretched downstream due to the strong wall-jet like flow as discussed in the previous chapter. With the post, the weaker wall-jet has less influence to the wake, producing a wider wake in the depthwise direction. The variations of spanwise velocity at multiple stations appear differently as they cut through the wake. Specifically, there is a small spanwise flow observed in the gap region ( $0.0 < Y^* < 1.0$ ) for the case with post which can be the result of flow distortion due to the post. Larger variations are captured in the wake region ( $1.0 < Y^* < 2.0$ ); however, the prediction of spanwise velocity profiles in the wake is difficult since the flow is highly chaotic in the region.

In the streamwise velocity plots for  $H/\Delta = 1.11$  (Figure 5.3a), similar trends observed in the small gap cases are again captured in this large gap case. Larger deviation in depthwise velocity is observed around  $Y^* = 2.0$  at  $X/\Delta = 2.5$  and 3.5 (Figure 5.3b,iii,iv). The downward shear flow from the leading edge (Figure 5.3b,i) is blocked by the post at the central section and the wake does not get pulled downward as in the case without the post. In the spanwise velocity plots (Figure 5.3c), there is no difference observed in the gap region for both large gap cases with and without the post, whereas small variations are captured in the wake region past the post. The magnitudes of spanwise velocity

variations along the wall normal direction are rather small compared to that of the small gap case. It should be highlighted that the spanwise velocity profile for the large gap case without post at the downstream location  $X/\Delta = 3.5$  shows almost zero velocity along the Y-axis, which indicates that the station is well outside of the wake. However, the large gap case with post shows small variation of  $\bar{W}/U_0$  at  $Y^* = 1.5$  where the difference in depthwise velocity is observed. This result suggests that this location is still influenced by the wake for the case of the large gap with post.

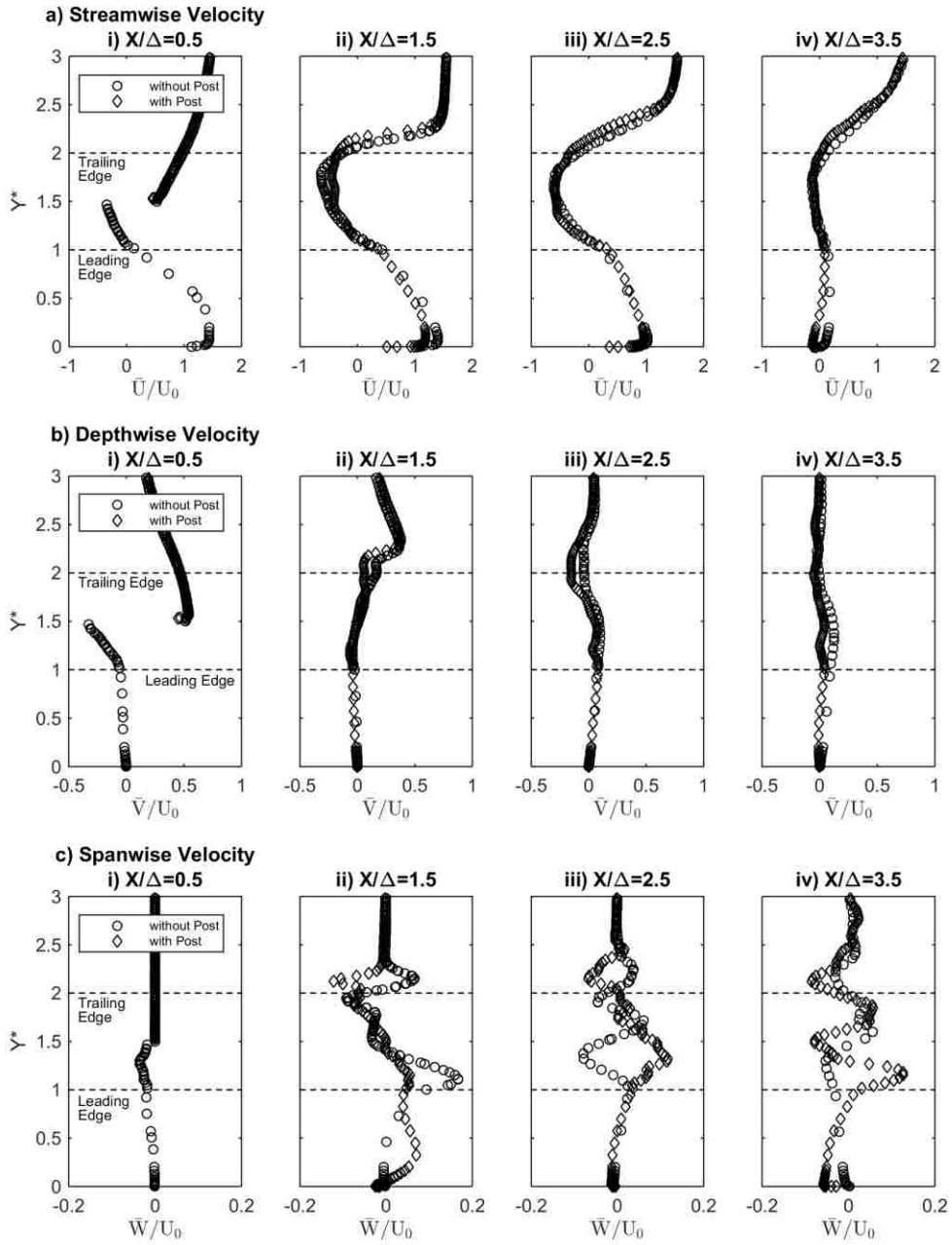


Figure 5.2: Velocity profiles at locations  $X/\Delta = 0.5, 1.5, 2.5$  and  $3.5$ , a) streamwise; b) depthwise; c) spanwise velocity, for  $H/\Delta = 0.22$

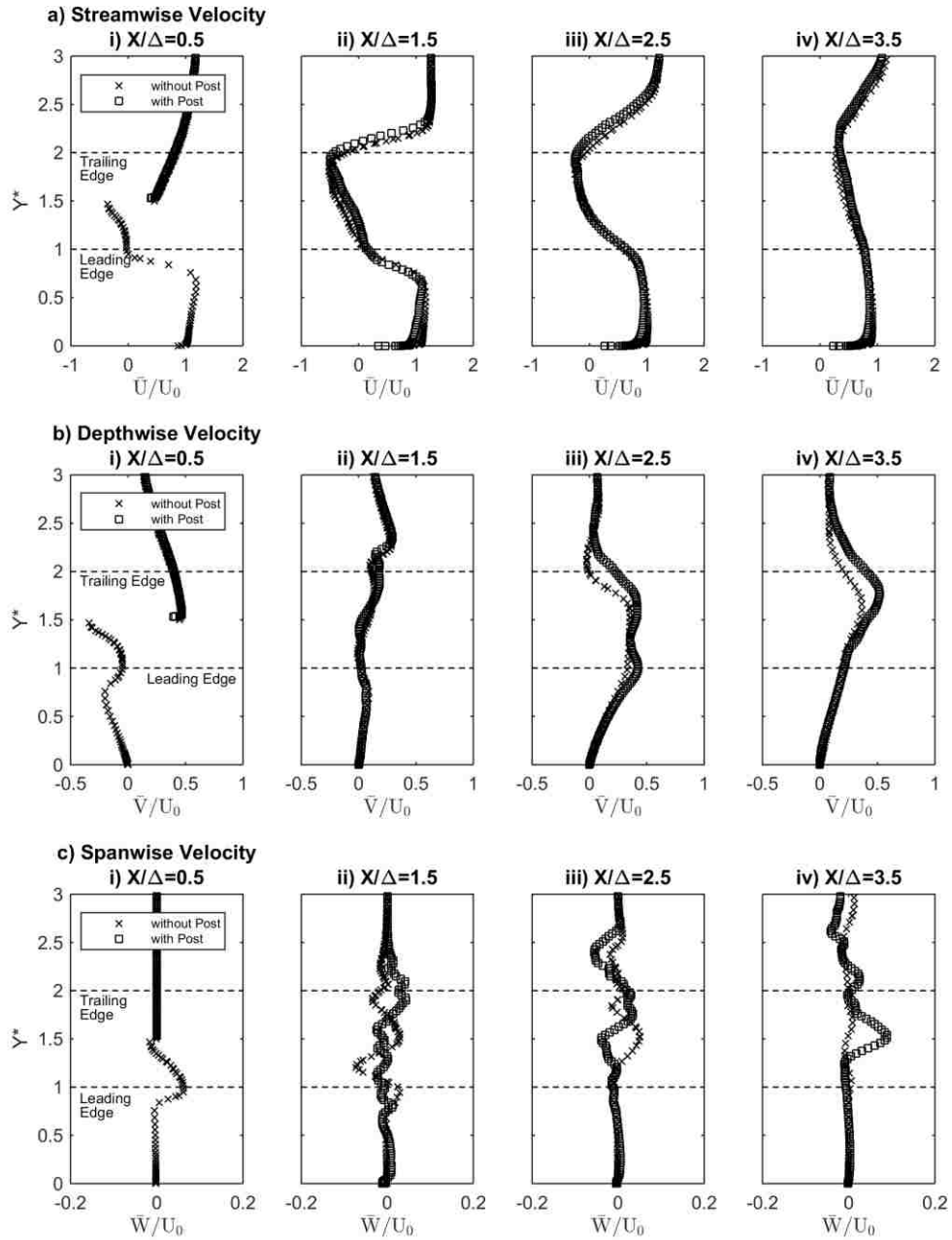


Figure 5.3: Velocity profiles at locations  $X/\Delta = 0.5, 1.5, 2.5$  and  $3.5$ , a) streamwise; b) depthwise; c) spanwise velocity, for  $H/\Delta = 1.11$

Further investigation of the flow near the post is presented in Figure 5.4. In these plots, the small gap case ( $H/\Delta = 0.22$ ) is shown with a diamond ( $\diamond$ ) and the large gap case ( $H/\Delta = 1.11$ ) with a square ( $\square$ ). The locations for these profiles are (i) the leading edge ( $X/\Delta =$

0.0), (ii) 1.5D upstream of the post ( $X/\Delta = 0.4D$ ), (iii) 1.5D downstream of the post ( $X/\Delta = 0.6D$ ) and (iv) the trailing edge ( $X/\Delta = 1.0$ ). As the flow approaches the post, the flow first separates from the leading edge and accelerates into the gap region (Figure 5.4a,i and b,i). The peak of the streamwise velocity profile is shifted towards the wall in the gap region, as was observed in Figure 5.2a, while the wall-jet like flow develops and a nearly zero depthwise velocity is captured upstream of the post (Figure 5.4a,ii and b,ii). On the other hand, downward flow is observed for the large gap case since the shear layer stretches towards the wall. Obviously, the spanwise velocity for both cases is zero in the upstream of the post (Figure 5.4c,i,ii). Behind the post, the streamwise velocity near the wall becomes zero while the peak shifts towards the leading edge since it is close to the recirculation bubble (Figure 5.4a,iii). In Figure 5.4b,iii the negative depthwise velocity is shown in the gap region for the small gap case since the recirculation bubble protrudes close to the wall, while the small variation is captured near the leading edge for the large gap case because the recirculation bubble cannot extend to the gap region. Therefore, the large variation is captured in the spanwise velocity profile for the small gap case (Figure 5.4c,iii). Further downstream, the flow recovers its characteristics that were observed in Figure 5.2 and 5.3.

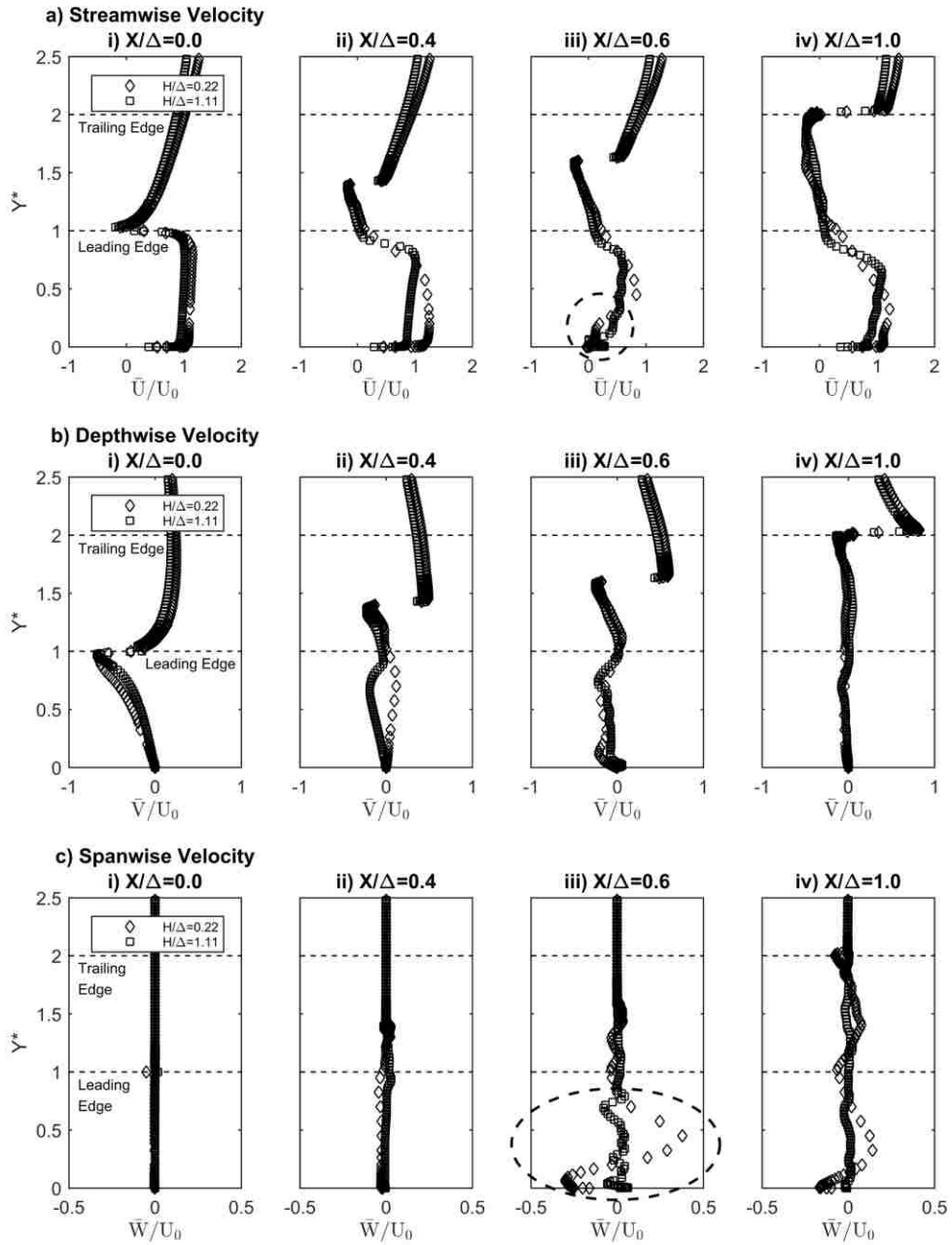


Figure 5.4: Velocity profiles at locations  $X/\Delta = 0.0, 0.4D, 0.6D$  and  $1.0$ , a) streamwise; b) depthwise; c) spanwise velocity, for  $H/\Delta = 0.22$  and  $1.11$

Figure 5.5 shows the streamtraces based on the mean velocities superimposed on the mean pressure contours on an  $XY$  plane at the midspan of the inclined flat plate. The mean pressure contours for the small gap case show that there is a shift at the lower



region ( $0.2 < Y/\Delta < 0.5$ ) of the low mean pressure band ( $-200 < P_{\text{mean}} < -150$  Pa), where the band is observed in the range from  $X/\Delta = 1.0$  to  $2.0$  at around  $Y/\Delta = 0.5$  for no post case (Figure 5.5b), whereas the band has shifted downstream by  $0.5\Delta$  for the case with post (Figure 5.5a). Similarly, there is a small expansion in the downstream for  $H/\Delta = 1.11$  with the post case (Figure 5.5c) compared to the case without post (Figure 5.5d). The slight shift in velocity profiles observed in Figure 5.2 and 5.3 can be identified by the streamtraces near the trailing edge. A small separation region near the wall at  $X/\Delta = 3.8$  seen in Figure 5.5b is also captured in Figure 5.5a, although the separation region is shifted upstream by  $0.3\Delta$ . No other significant difference is observed on this plane since the presence of the post does not have much effect on the streamwise and depthwise velocities.

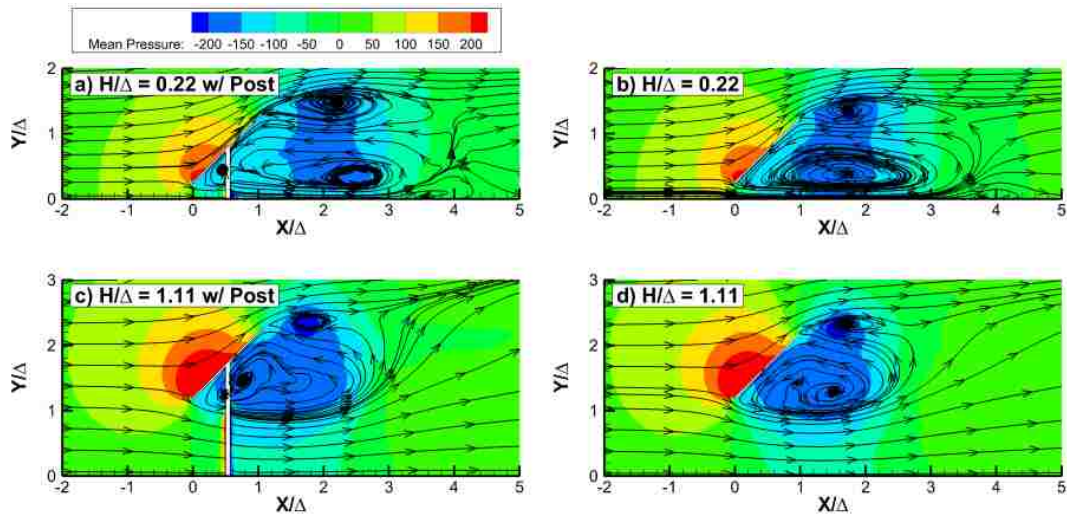


Figure 5.5: Mean velocity flow streamtraces on the central plane, superimposed with mean pressure (Pa) contours for a)  $H/\Delta = 0.22$  with post, b)  $H/\Delta = 0.22$  without post, c)  $H/\Delta = 1.11$  with post and d)  $H/\Delta = 1.11$  without post

The streamtraces on  $YZ$  planes are presented in Figure 5.6, superimposed with mean streamwise ( $X$ ) vorticity contours, at multiple downstream stations for the small gap  $H/\Delta = 0.22$ . The left column is the case with post and the right column is the case without post.

Note that the positive X-axis is directed into the plots; thus, the clockwise rotation is presented as positive X-vorticity (red) and the counter-clockwise rotation corresponds to negative vorticity (blue). A cross-section at  $X/\Delta = 0.5$ , where the plane cuts through the post, is illustrated in Figure 5.6a and the same section for the case without post is shown in Figure 5.6e. Clearly, the supporting structure generates streamwise vortices around it. The size of these vortices adjacent to the post is about the size of the wake in the vertical direction. At  $X/\Delta = 1.5$  the flow pattern is complex as indicated by the small vortex patches observed in the wake (Figure 5.6b,f). A large peak in spanwise velocity that was observed at  $Y^* \approx 1.0$  (equivalent to  $Y/\Delta \approx 0.22$ ) for the small gap case without post in Figure 5.2c,ii is found at the valley of two vortices around  $Z/\Delta = 1.0$  (Figure 5.6f), whereas the peak does not appear in the case with post due to the absence of the paired vortices (Figure 5.6b). Even though the vortex observed at the centre of the wake in the case without post (Figure 5.6f) is not captured in the case with post (Figure 5.6b), the vortices that develop from the top and side edges of the flat plate and the two patches near the wall are still present. In both cases the pair of vortices is captured in Figure 5.6c,d,g,h above the trailing edge ( $Y/\Delta \approx 1.22$ ), which was found to be the traces of the legs of hairpin-like vortex in Chapter 4. The flow at this location still remains complex as it is in the wake. In Figure 5.6c, two vortices are captured by the streamtraces in the midspan of the wake at  $X/\Delta = 2.5$  for the case with post, whereas no such structure is found in the case without post. Similar to Figure 5.2c,ii, peaks are identified in Figure 5.2c,iii,iv as the midspan stations cut through the valleys of streamwise vortices in Figure 5.6c,d,g,h.

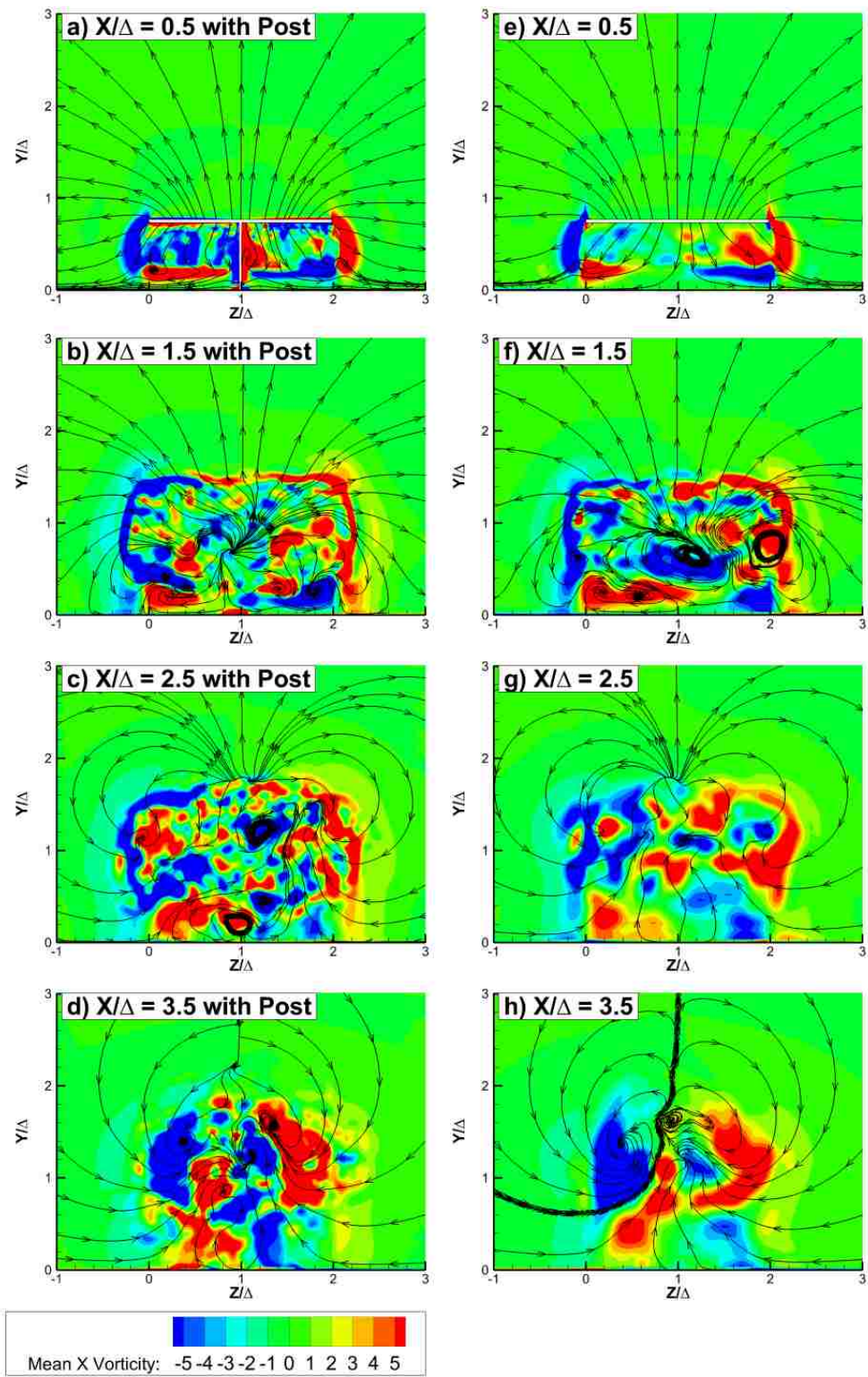


Figure 5.6: Streamtraces superimposed with X-vorticity contours on YZ planes at  $X/\Delta = 0.5, 1.5, 2.5$  and  $3.5$  for  $H/\Delta = 0.22$  with post (left) and  $H/\Delta = 0.22$  without post (right)

Similarly, the streamtraces on YZ planes for  $H/\Delta = 1.11$ , superimposed with mean streamwise (X) vorticity contours, at the same downstream locations, are presented in Figure 5.7. Large streamwise vorticity patches are found in the wake adjacent to the post, whereas the small scale contour patches are seen along the post at the lower side. In Figure 5.7b, there are two weak (red) patches observed in the gap region ( $Y/\Delta \approx 0.0$  and  $1.0$ ) at  $X/\Delta = 1.5$ , which are structures extended from the large patches observed in the wake and the small upstream vortices along the wall. Overall, the streamtraces show symmetric patterns about the midspan of the plate as a result of the small variations observed in the spanwise velocity profiles (Figure 5.3c). Therefore, the supporting structure has minimal influence in the downstream for the large gap case since a wall-jet like flow does not develop in the gap region for this case.

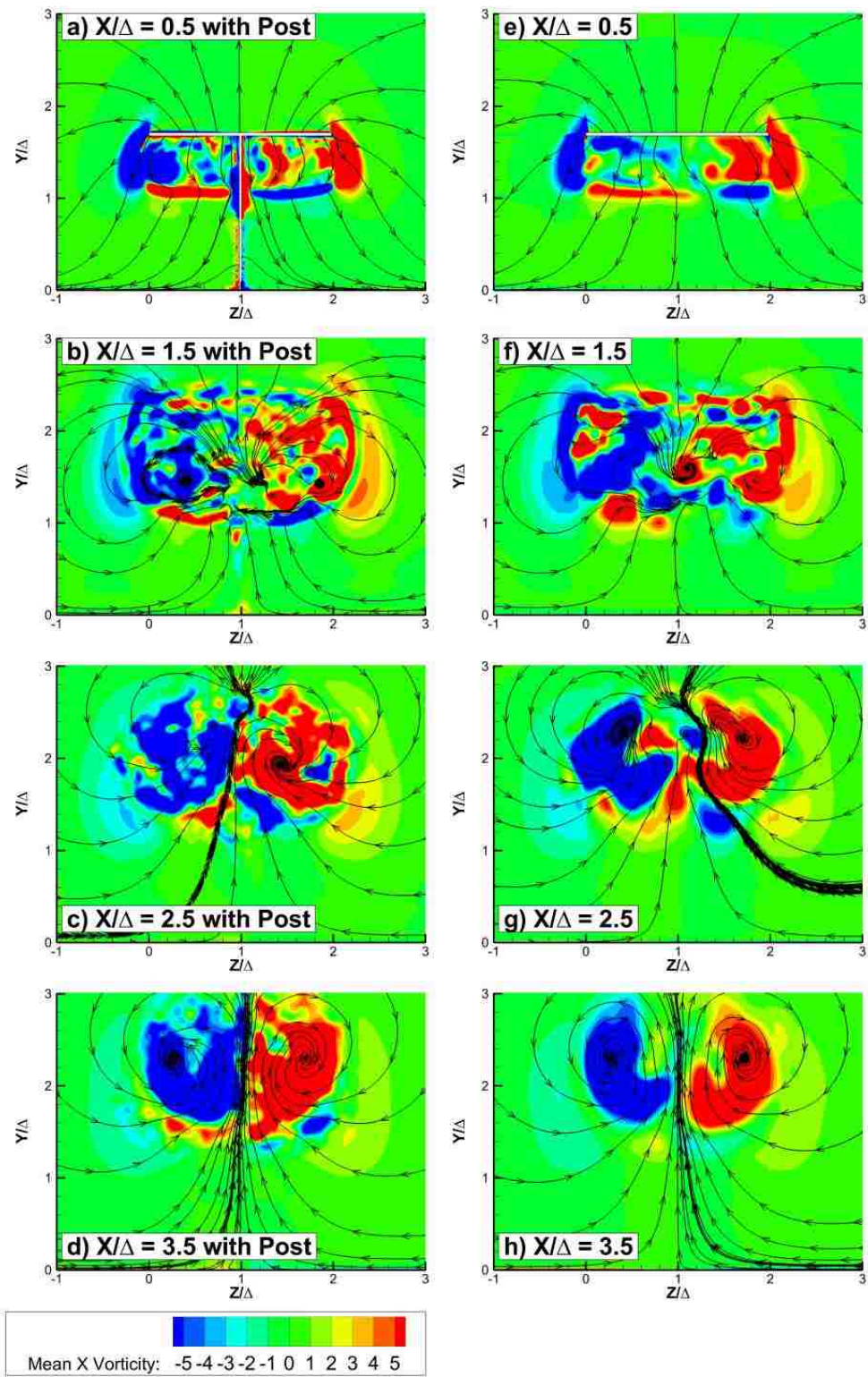


Figure 5.7: Streamtraces superimposed with X-vorticity contours on YZ planes at  $X/\Delta = 0.5, 1.5, 2.5$  and  $3.5$  for  $H/\Delta = 1.11$  with post (left) and  $H/\Delta = 1.11$  without post (right)

## 5.4. Three-dimensional transient flow analysis

As observed in the two-dimensional analysis, the selected post size has shown only a small influence on the wake in the mean flow field. However, there are traces of small vortical structures that develop along the post and are stretched into the downstream, as observed in the transverse sections in the downstream. To further understand the interaction of the flow and the supporting structure, a transient three-dimensional CFD analysis is used to capture the flow structures using the iso-surfaces of  $\lambda_2$  obtained from the  $\lambda_2$ -criterion, developed by Jeong and Hussain [23]. The derivation of the method is available in Chapter 2. Similar to the previous chapter, early stage flow development is first analyzed to capture the formation of unique structures around the bluff bodies with the post. The development of these fluid structures is compared to the case without post and the role of the post in their evolution over time is discussed. Especially in the small gap case, close investigations near the wall are conducted to visualize the interaction of the flow in the gap with the post. In this section, the iso-surfaces of  $\lambda_2/\lambda_{2\min}$  value of 0.001 are selected to visualize the fluid structures. This value is one tenth of that selected in the previous chapter since the minimum  $\lambda_2$  is found to be much larger in the current study; therefore, the value is adjusted so that the same iso-surface of  $\lambda_2$  value is presented in this section. The iso-surfaces are coloured by the Y-vorticity.

### 5.4.1. Early stage flow development

Recall the fluid structures identified in Figure 4.10 in Chapter 4, four unique fluid structures are formed around the inclined flat plate for  $H/\Delta = 0.22$  at a time of 0.16 s after the start of the flow: (1) a hairpin-like vortex, (2) an inverted hairpin-like vortex, (3) a pair of vortex tubes extended vertically and (4) corner vortices. The structure (3), a pair

of vortex tubes, was only captured in the small gap case since it developed while the flow interacted with wall.

In Figure 5.8, the history of the flow development for the small gap cases with post (left) and without post (right) are presented for comparison. At  $t = 0.05$  s, three out of the above four structures, excluding Structure 4, are still captured in the case with post. The inverted hairpin-like vortex (Structure 2 in Figure 5.8a) bends towards the leading edge as the flow is blocked by the post. Meanwhile, the counter-rotating vortex on the wall (Structure 3' in Figure 5.8a) also appears as the invert hairpin-like vortex reaches to the wall. It merges with the structure that develops along the post and together they are lifted upward as they get trapped by Structure 2 (Structure 3'' in inset at  $t = 0.09$  s). At  $t = 0.15$  s (Figure 5.8b), a pair of vortex tubes (Structure 3) develop vertically upward, bend around Structure 2 and stretch towards the leeward of the plate. There is no significant difference in the formation of these structures up to this instant. The hairpin-like vortex is clearly observed at  $t = 0.55$  s while the structures in the wake and near the wall are rather small and chaotic for the case with post (Figure 5.8c). There is a pair of vortices that stretch vertically and bend into the hairpin-like vortex (Structure 5). This pair of vortices is not the same as Structure 3 since the pair develops around the hairpin-like vortex and is trapped within the vortex. Later in the development, the ligaments which are captured along the wall in the case without post become discrete and scattered (Structure 6).

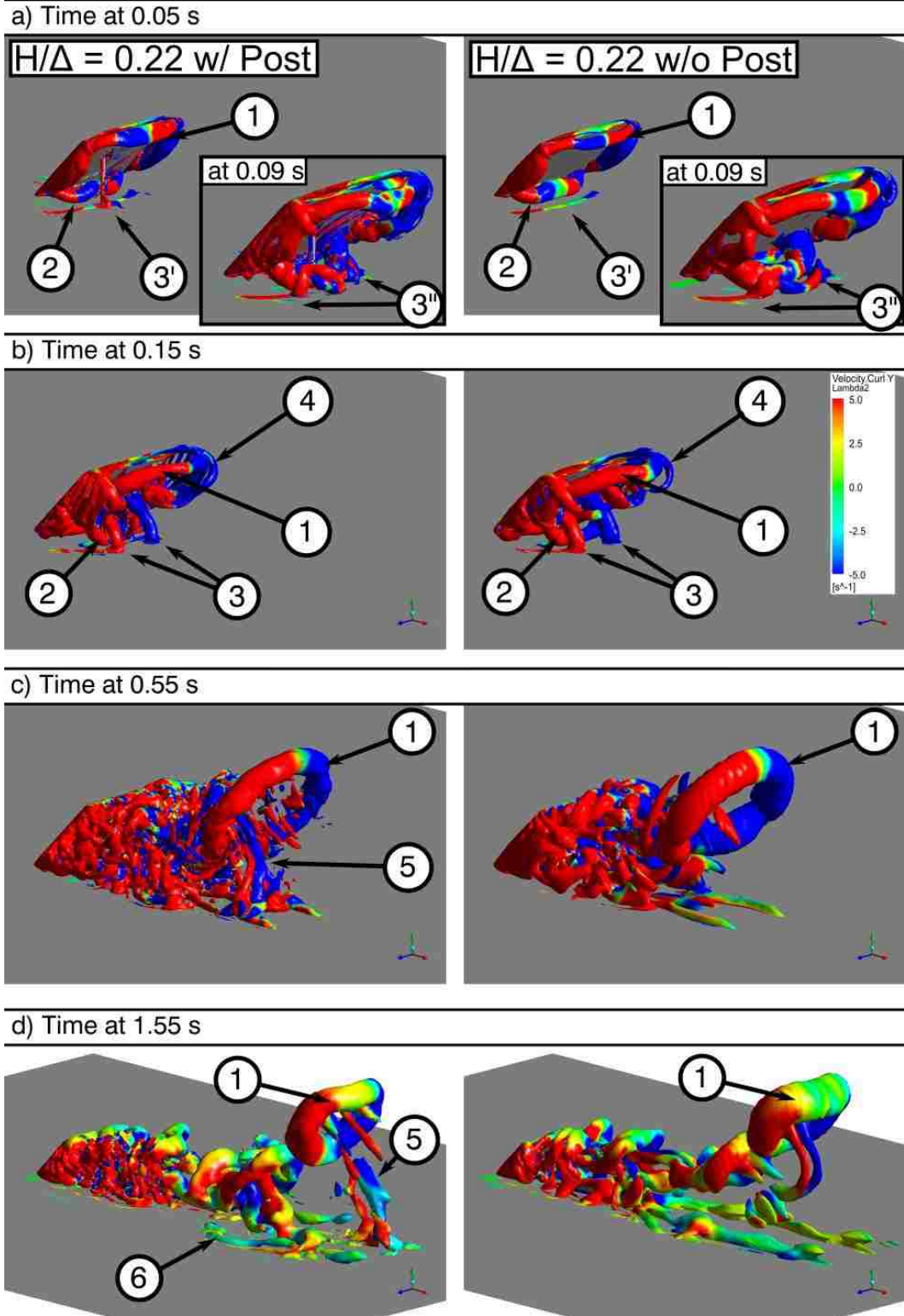


Figure 5.8: Early stage development of flow structures around the inclined plate for  $H/\Delta = 0.22$  with post (left) and without post (right)



Similarly, the history of fluid structures developed around the inclined flat plate with a large gap near the wall is presented in Figure 5.9. As observed in Chapter 4, three vortical structures, excluding the pair of vortices, are formed in the large gap case (Figure 5.9b). Since the inverted hairpin-like vortex bends toward the leeward of the plate while it develops along the leading edge (Figure 5.9a), the penetration of the vortex tube is shorter compared to the case without the post at  $t = 0.15$  s (Figure 5.9b). The inverted hairpin-like vortex is not clearly captured at  $t = 0.55$  s where the overall fluid structures are complicated in the case with post compared to without post. At the bottom of the post, the approaching flow interacts with the post and wall, where it develops ligament of a vortex tube (Structure 7) in the streamwise direction as observed in Figure 5.7a. The ligament of the vortex tube further stretches into the downstream where the colour of the structure is shown in green, indicating that the structure rotates about the streamwise (X) direction. Meanwhile, there are small scale streamwise vortical structures formed along the post, as illustrated in Figure 5.9c and d. These structures are not identified in the small gap case since the wake is close to the wall. To further understand the fluid structure development near the wall, the three-dimensional fluid structures are viewed from a different orientation.

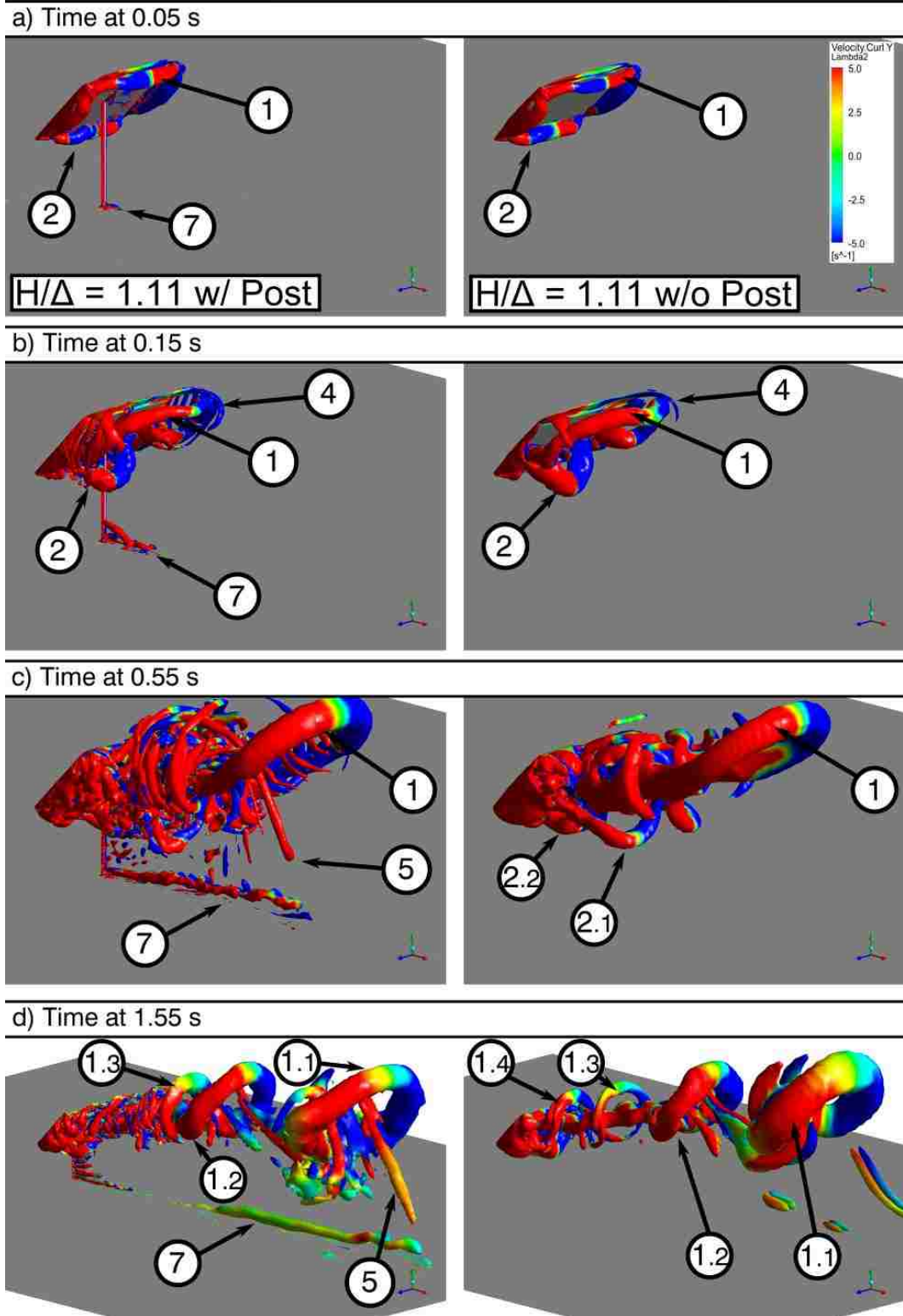


Figure 5.9: Early stage development of flow structures around the inclined plate for  $H/\Delta = 1.11$  with post (left) and without post (right)

In order to check the flow development near the wall, the iso-surface of  $\lambda_2$  is viewed from the bottom (negative Y) with a non-transparent (gray) horizontal plane set at the height of the leading edge ( $Y/\Delta = 0.22$ ) to screen out the structures above the leading edge (Figure 5.10). The left hand column shows the structures developed near the wall for the small gap case with post and on the right hand side shows the case without post. At  $t = 2.0$  s (Figure 5.10a), the symmetric distribution of flow structures observed in the downstream for the case without post is replaced by an asymmetry pattern for the case with post. The meandering vortex structures found in the downstream in Chapter 4 are identified with labels L and R in Figure 5.10 for the case with post. There are also structures (coloured in red and blue) which extend from the post similar to those observed in the large gap case with post (Figure 5.9c,d). However, unlike the large gap case, the contour patches extending from the post merge with the meandering vortices L2 and R2 (Figure 5.10b,c). Nevertheless, since the scale of the vortices developed from the post is small, these vortices do not seem to have a large influence on the meandering structures.

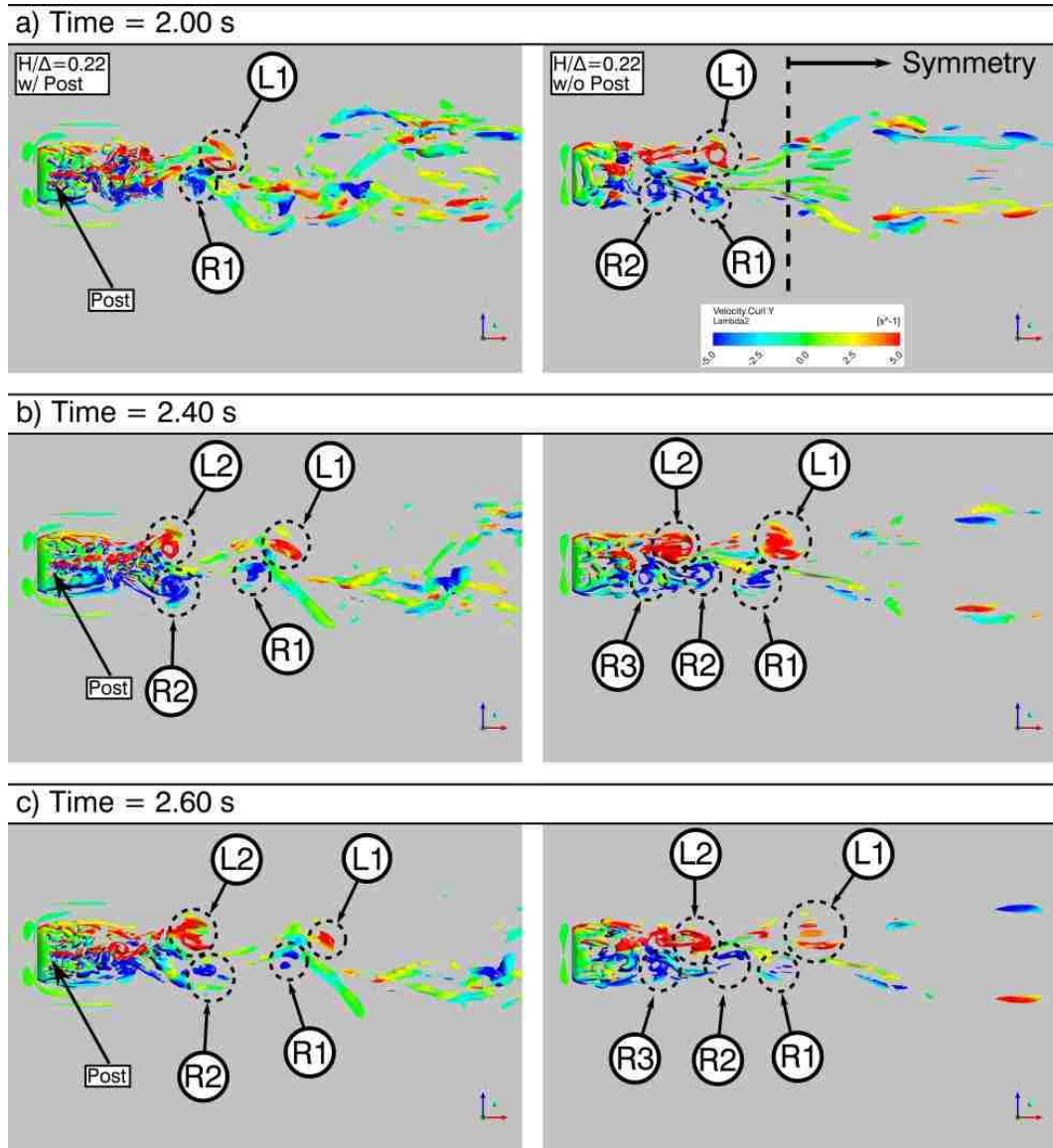


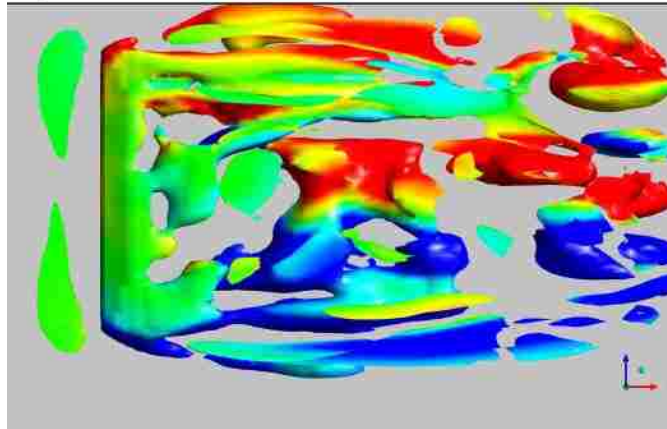
Figure 5.10: Bottom view of the same structures with the filtering plane set at  $Y/\Delta = 0.22$  for  $H/\Delta = 0.22$  with post (left) and without post (right)

#### 5.4.2. Steady state condition in the mean

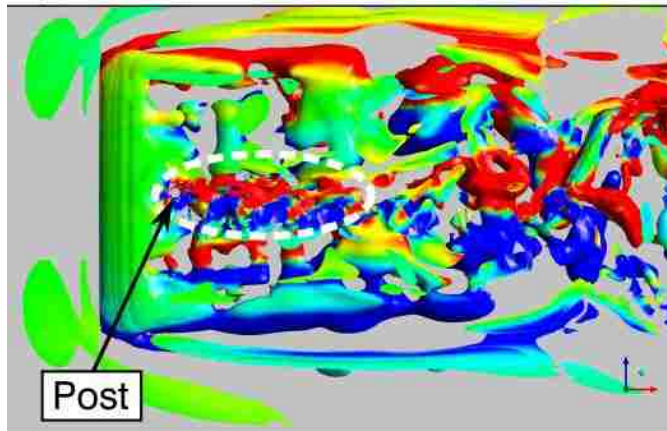
A closer examination of the structures formed around the post after the flow has achieved a steady state condition in the mean is presented in Figure 5.11, showing the iso-surfaces of  $\lambda_2$  at  $t = 5.6$  s with a gray non-transparent horizontal plate placed at the height of the leading edge. The top figure (Figure 5.11a) shows the case without the post for the small gap, the middle figure (Figure 5.11b) captures the structures for the case with post for the

small gap, and the bottom figure (Figure 5.11c) presents the case with post for the large gap. As observed in Figure 5.10b,c, the structures extending from the post are captured within the white dashed circle in Figure 5.11b. Compared to the structures extending from the post for the large gap case, these structures are shorter for the small gap as they merge with larger scale vortices developed by the interaction of the wall and the flow that separates from the leading and side edges (e.g. Structure 3 in Figure 5.8). Downstream of the dashed region, the small scale vortices extending from the post spread wider as they are trapped by the large scale vortices developed from the side edges of the plate.

a)  $H/\Delta=0.22$  w/o Post



b)  $H/\Delta=0.22$  w/ Post



c)  $H/\Delta=1.11$  w/ Post

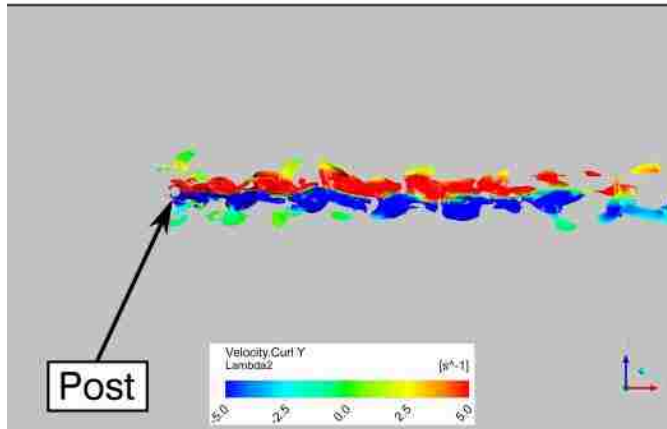


Figure 5.11: Iso-surfaces of  $\lambda_2$  at  $t = 5.60$  s with colour contours of Y-vorticity on these surfaces for  $H/\Delta=0.22$  (left) and  $H/\Delta=1.11$  (right)

## 5.5. Conclusions

The numerical investigation of flow past a stand-alone solar panel set near a wall at two different elevations ( $H/\Delta = 0.22$  and  $1.11$ ) is presented in this chapter. A cylindrical supporting structure is added to the geometry modelled in Chapter 4. Mean flow characteristics are analyzed and the three-dimensional fluid structures, visualized by the iso-surface of  $\lambda_2$  calculated from the  $\lambda_2$ -criterion, are investigated and compared with the case without post.

The mean velocity profiles show the development of a wall-jet like flow in the gap region for the small gap case ( $H/\Delta = 0.22$ ), while the strong downwash separation is identified for the large gap case ( $H/\Delta = 1.11$ ). There is no significant difference observed in the profiles between the cases with and without the post. It can be concluded that the post used for these simulations (0.15 m diameter) does not generate much disturbance in the downstream. The velocity profiles adjacent to the post show that the approaching flow is not affected by the presence of the post, whereas the flow downstream of the cylinder is largely influenced by the recirculation bubble that forms behind the plate. These observations are also captured in the two-dimensional streamtraces superimposed on the mean pressure contours plotted on the vertical plane at the midspan of the inclined flat plate. A slight difference in the size of the wake is seen in this plot. The transverse sectional planes are also presented with the streamtraces superimposed on the mean streamwise vorticity. Streamwise vorticity patches along the post in the wake and near the wall are found in the cross-section plane at  $X/\Delta = 0.5$ . Small patches at the same locations are observed in the plane at  $X/\Delta = 1.5$ , which represent streamwise vortical

structures stretching from the post. However, there is no significant difference in the two-dimensional mean flow field for the cases with and without post.

The early stage transient three-dimensional flow development shows four unique fluid structures in the small gap case with post. There is a small disturbance in these fluid structures at the beginning of their development, while the fluid structures become complex at a later stage for both cases. Streamwise vortical tubes first form at the junction of the post and the wall, then these tubes also develop along the post. These streamwise vortical structures stretch into the downstream but do not interact with the wake and other fluid structures such as hairpin-like vortices or inverted hairpin-like vortices. The bottom view with a filter placed at the height of leading edge captures the fluid structures forming along the wall in an asymmetric pattern for the case with post, whereas a symmetric flow pattern is observed in the case without post. Close examination of the fluid structures around the post shows that the streamwise vortical structures extending from the post merge with the large scale vortices formed by the wake for the small gap case.

From the above observations it can be concluded that the selected post does not have a large impact on the main fluid structures that develop around the bluff body, but it promotes the generation of small scale vortical structures around it. As a result, the wind load acting on the stand-alone solar panel will not change significantly. From an optimal design perspective, further investigations with different sizes of post are recommended to determine the point at which the flow interacts with the three objects, the inclined flat plate, post and wall, in such a way to minimizing the wind load on the inclined flat plate.



## Chapter 6. Conclusions and recommendations

The overall objective of this study was to analyze the unsteady flow development around bluff bodies. The CFD simulations were conducted using the DES turbulence model. The study consisted of three phases: (1) flow past an infinitely long inclined flat plate, (2) flow past a finite inclined plate near a wall, and (3) flow past a stand-alone solar panel supported by a cylindrical post.

### 6.1. Conclusions

The DES simulations of the classical flow past an infinitely long inclined flat plate at high Reynolds number captured the regular von Kármán vortices shed from the body. The vortex shedding frequency based on velocity measurement in the downstream and the mean pressure distribution on the plate were successfully validated with experimental results. It was shown that the shed vortices quickly dissipated in the downstream. As expected from wake transition studies, streamwise vortices were identified in the transverse cross-section planes in the downstream beyond the wake region. Streamwise vortices in the transverse section near the body were also captured within the wake and exhibited oscillatory behaviour, being trapped by the spanwise vortices shed periodically from the body. Although the above 2-D sectional planes showed the interaction of spanwise and streamwise vortices, they did not fully illustrate the development and interactions of these structures. Thus, three-dimensional flow visualization using  $\lambda_2$ -criterion was introduced to further process the data.

The iso-surface of  $\lambda_2$  showed that the distortion of the spanwise vortices in the far downstream was the mechanism that produced the rapid dissipation of the vortices that

were observed in the midspan cross-section. The streamwise vortices were formed along the braids of previously shed spanwise vortices. The spanwise wavelength of streamwise vortices was found to range from 0.7 to 1.8 times of the flat plate width, which matched with the mode B instability reported by other researchers. Wobbling as a result of the spanwise instability was also observed in the shear layer and spanwise vortices at the trailing edge, whereas the shear layer at the leading edge was smooth. Examining the details inside the wake region illustrated the development of streamwise vortices right behind the inclined flat plate which had a large influence to the shear layer and spanwise vortices as they formed. Meanwhile, since there was little available space near the leading edge to develop the streamwise vortices, the shear flow from the leading edge was dominant and promoted the development of a smooth shear layer.

These observations demonstrate that a typical two-dimensional flow model (for an infinitely long body) fails to predict the three-dimensionality in the wake. What appears to be dissipation of vortices in the two-dimensional analysis is the effect of the small scale streamwise vortices on the large scale spanwise vortices as they distort in the downstream.

Flow past a finite inclined flat plate near a wall was also investigated for two different gap heights between the wall and the plate. For the small gap case, a wall-jet like flow in the gap region with a weak upward flow was captured in the mean streamwise and depthwise velocity profiles. A strong downwash was observed in the large gap case as the flow separated from the leading edge, but this was immediately followed by an upwash. The results using streamtraces and pressure contours illustrated an expansion of the wake for the small gap case and a reduction in wake size for the large gap case. The same

observations were presented in the streamtraces superimposed on the mean pressure contour in the midspan cross-section. Since the wake was expanded, the low pressure field was shifted downstream so that the wind load on the plate was reduced.

The transient flow development was illustrated by the instantaneous velocity vectors and spanwise vorticity contours on the midspan cross-section. For small gap case, the vortex shed from the leading edge interacted with the wall and generated a counter-rotating vortex. The counter-rotating vortex was trapped into the wake by the shed vortex while it developed. When the flow achieved the steady state condition in the mean, the counter-rotating vortex travelled along the wall. As the wall-like jet formed at the gap, the shear layer at the leading edge appeared parallel to the wall for the small gap case, whereas the shear-layer took an arc shape for the large gap case.

At the early stage of flow development, the iso-surface of  $\lambda_2$  was able to capture four unique fluid structures around the bluff body for the small gap case: (1) a hairpin-like vortex, (2) an inverted hairpin-like vortex, (3) a vortex pair extended vertically from the wall and (4) corner vortices. The vortex pair developed due to the interaction of an inverted hair-pin vortex with the wall. The vortex pair was found to be part of the counter-rotating vortex that was seen in the transient velocity vector plots and spanwise vorticity contours on the midspan cross-section. Later, the pair was identified as the source of meandering structures along the wall in the downstream. As the wake stretched due to the wall-jet like flow, the legs of the hairpin-like vortex were found to be almost parallel to the wall for the small gap case. The same structure was identified for the large gap case, but it curled upwards because of the strong upwash. Since the flow with large gap did not interact with the wall, the vortex pair was not captured in this case.

Once the flow was steady in the mean, distorted flow structures were identified for the small gap case, whereas the symmetric flow structures were maintained for the large gap case. In summary, two-dimensional cross-sectional analysis and three-dimensional flow visualization using the iso-surface of  $\lambda_2$  was able to present the mechanisms of fluid structure development around the inclined plate near the wall.

Building on the fundamental studies discussed above, flow past a realistic geometry for a top mounted stand-alone solar panel was simulated to determine the role of the supporting structure (post) with the wall effect. Similar to the case without the post, the mean velocity profiles showed the presence of a wall-like jet in the gap region for the small gap case, whereas the strong downwash and upwash were captured for the large gap case. In the downstream, there was no significant difference observed compared to the case without post. The mean velocity profiles adjacent to the post showed that the flow past the post was influenced by the recirculation bubble that developed behind the plate. These observations were confirmed by examining the streamtrace plots superimposed on the mean pressure contours in the midspan cross-section. In the transverse cross-sections at the post, additional streamwise vortices were found along the post. Large vortices were identified in the wake and small vortices were captured at the corner of the post and the wall. Similar vorticity contour patches were observed in the downstream transverse cross-section, indicating development of streamwise structures along the post.

The transient three-dimensional visualization using  $\lambda_2$ -criterion was able to capture the four unique structures which were identified in the case without post. At the early stage development, the supporting structure generated only small disturbances on the fluid

structures. However, the structures became more complex as the flow reached the steady state condition in the mean for both cases. In the case of large gap case, the streamwise vortices were initially identified at the corner junction of the post and the wall. Later, these vortices appeared along the post but did not interact with the wake. The same structure at the corner junction was captured in the small gap case. The streamwise structures were found to merge into large vortical structures in the wake. The meandering structures were again observed in the small gap case. It was found that the influence of post (for the size selected in this study) on the flow developed around the bluff body was rather small, and as a result, the presence of the supporting structure did not change the wind load acting on the plate.

## **6.2. Recommendations**

This study has shown that DES is able to capture the transient three-dimensional fluid structures that develop around the inclined flat plate. The  $\lambda_2$ -criterion is a valuable tool to identify both small to large vortical structures in the wake. However, the iso-surface of a single  $\lambda_2$  value could miss weaker vortices around the body and in the downstream. It is not known how these weaker vortices might interact with the main body or with objects located in the downstream region. It could be informative to explore different kinds of vortex core identification criteria to further identify the unique fluid structures in the flow. Further studies are also needed to optimize the gap spacing and investigate the effects of other parameters such as yaw angle and plate aspect ratio on the wind load. Analysis of the flow development is further explored by conducting the phase-averaging and quantifying the characteristics of the flow past the inclined bluff bodies. Additionally, the flow past an infinitely long inclined flat plate (studied in Chapter 3) set near a wall can be

simulated to analyze the effect of the wall without the flow separation from the side edges of the plate. Alternatively, the finite length inclined flat plate can be subjected to the freestream to show the flow development from the side edges. The effect of aspect ratio on the unique fluid structures observed in Chapter 4 is also of interest.

## References

- [1] Blackwell, R., Solar Power Surging to Forefront of Canadian Energy. *The Globe and Mail*, July 26, 2014, accessed November 10, 2014, <http://www.theglobeandmail.com/report-on-business/solar-power-surging-to-forefront-of-canadian-energy/article19786759/>.
- [2] Shademan, M., and Hangan, H., 2009, Wind Loading on Solar Panels at Different Inclination Angles, 11th Americas Conference on Wind Engineering, San Juan, Puerto Rico, June 22-26.
- [3] Stathopoulos, T., Zisis, I., and Xypnitou, E., 2012, Wind Loads on Solar Collectors: A Review. Structures Congress 2012, pp. 1169-1179.
- [4] Shademan, M., Barron, R.M., and Balachandar, R., 2014, Unsteady Wind Loading of Solar Panels in Arrayed Configuration. Proc. The Canadian Society for Mechanical Engineering International Congress 2014, June 1-4, p. 5.
- [5] Jubayer, C.M., and Hangan, H., 2016, A Numerical Approach to the Investigation of Wind Loading on an Array of Ground Mounted Solar Photovoltaic (PV) Panels. *J. Wind Eng. Ind. Aerodyn.*, 153, pp. 60-70.
- [6] Warsido, W.P., Bitsuamlak, G.T., Barata, J., and Gan Chowdhury, A., 2014, Influence of Spacing Parameters on the Wind Loading of Solar Array. *J. Fluid Struct.*, 48, pp. 295-315.
- [7] Yu, Y., 2012, Numerical Simulation of Wind Load on Roof Mounted Solar Panels. M.A.Sc. Thesis, Department of Mechanical, Automotive and Materials Engineering, University of Windsor, Windsor.

- [8] Pratt, R.N., and Kopp, G.A., 2013, Velocity Measurements around Low-Profile, Tilted, Solar Arrays Mounted on Large Flat-Roofs, for Wall Normal Wind Directions. *J. Wind Eng. Ind. Aerodyn.*, 123, Part A, pp. 226-238.
- [9] Jubayer, C.M., and Hangan, H., 2014, Numerical Simulation of Wind Effects on a Stand-Alone Ground Mounted Photovoltaic (PV) System. *J. Wind Eng. Ind. Aerodyn.*, 134, pp. 56-64.
- [10] Jubayer, C.M., Hangan, H.M., and Siddiqui, K., 2014, Numerical and Experimental Investigations of Wind Flow around Ground Mounted Solar Panels, XIII Conference of the Italian Association for Wind Engineering, Genova, Italy, June 22-25, p. 10.
- [11] Shademan, M., Balachandar, R., and Barron, R.M., 2014, Detached Eddy Simulation of Flow Past an Isolated Inclined Solar Panel. *J. Fluid Struct.*, 50, pp. 217-230.
- [12] Fage, A., and Johansen, F.C., 1927, On the Flow of Air Behind an Inclined Flat Plate of Infinite Span. *Proceedings of the Royal Society of London A: Mathematical, Physical and Engineering Sciences*, 116(773), pp. 170-197.
- [13] Versteeg, H.K., and Malalasekera, W., 2007, An Introduction to Computational Fluid Dynamics: The Finite Volume Method. Pearson Education Limited, UK.
- [14] Wilcox, D.C., 1994, Turbulence Modeling for CFD. DCW Industries Inc., La Canada, CA.
- [15] Spalart, P.R., 2000, Strategies for Turbulence Modelling and Simulations. *Int. J. Heat Fluid Flow*, 21(3), pp. 252-263.



- [16] Menter, F.R., Kuntz, M., and Langtry, R., 2003, Ten Years of Industrial Experience with the SST Turbulence Model. *Turbulence, Heat and Mass Transfer 4: Proceedings of the 4th International Symposium on Turbulence, Heat and Mass Transfer*, K. Hanjalic, Y. Nagano, and M. Tummers, eds., Begell House, Inc., Antalya, Turkey, pp. 625-632.
- [17] Spalart, P.R., 2009, Detached-Eddy Simulation. *Annu. Rev. Fluid Mech.*, 41(1), pp. 181-202.
- [18] Spalart, P., 2006, Topics in Detached-Eddy Simulation. *Computational Fluid Dynamics 2004*, C. Groth, and D. Zingg, eds., Springer Berlin Heidelberg, pp. 3-12.
- [19] ANSYS, 2013, ANSYS Fluent Theory Guide. ANSYS Inc., Canonsburg, PA.
- [20] Chakraborty, P., Balachandar, S., and Adrian, R.J., 2005, On the Relationships between Local Vortex Identification Schemes. *J. Fluid Mech.*, 535, pp. 189-214.
- [21] Hunt, J.C.R., Wray, A.A., and Moin, P., 1988, Eddies, Streams, and Convergence Zones in Turbulent Flows, *Proceedings of the 1988 Summer Program*, pp. 193-208.
- [22] Chong, M.S., Perry, A.E., and Cantwell, B.J., 1990, A General Classification of Three - Dimensional Flow Fields. *Physics of Fluids A: Fluid Dynamics (1989-1993)*, 2(5), pp. 765-777.
- [23] Jeong, J., and Hussain, F., 1995, On the Identification of a Vortex. *J. Fluid Mech.*, 285, pp. 69-94.

- [24] Roshko, A., 1954 On the Development of Turbulent Wakes from Vortex Streets. Report 1191, National Advisory Committee for Aeronautics, Washington D.C., USA, p. 25.
- [25] Williamson, C.H.K., 1996, Vortex Dynamics in the Cylinder Wake. *Annu. Rev. Fluid Mech.*, 28(1), pp. 477-539.
- [26] Williamson, C.H.K., 1996, Three-Dimensional Wake Transition. *J. Fluid Mech.*, 328, pp. 345-407.
- [27] Zhang, H.Q., Fey, U., Noack, B.R., König, M., and Eckelmann, H., 1995, On the Transition of the Cylinder Wake. *Phys. Fluids*, 7(4), pp. 779-794.
- [28] Mittal, R., and Balachandar, S., 1995, Generation of Streamwise Vortical Structures in Bluff Body Wakes. *Phys. Rev. Lett.*, 75(7), pp. 1300-1303.
- [29] Robichaux, J., Balachandar, S., and Vanka, S.P., 1999, Three-Dimensional Floquet Instability of the Wake of Square Cylinder. *Phys. Fluids*, 11(3), pp. 560-578.
- [30] Blackburn, H.M., and Lopez, J.M., 2003, On Three-Dimensional Quasiperiodic Floquet Instabilities of Two-Dimensional Bluff Body Wakes. *Phys. Fluids*, 15(8), pp. L57-L60.
- [31] Sheard, G.J., Fitzgerald, M.J., and Ryan, K., 2009, Cylinders with Square Cross-Section: Wake Instabilities with Incidence Angle Variation. *J. Fluid Mech.*, 630, pp. 43-69.
- [32] Choi, C.-B., and Yang, K.-S., 2014, Three-Dimensional Instability in Flow Past a Rectangular Cylinder Ranging from a Normal Flat Plate to a Square Cylinder. *Phys. Fluids*, 26(6), p. 061702.

- [33] Yang, D., Narasimhamurthy, V.D., Pettersen, B., and Andersson, H.I., 2012, Three-Dimensional Wake Transition Behind an Inclined Flat Plate. *Phys. Fluids*, 24(9), p. 094107.
- [34] Lloyd, T.P., and James, M., 2016, Large Eddy Simulations of a Circular Cylinder at Reynolds Numbers Surrounding the Drag Crisis. *Applied Ocean Research*, 59, pp. 676-686.
- [35] Lysenko, D.A., Ertesvåg, I.S., and Rian, K.E., 2014, Large-Eddy Simulation of the Flow over a Circular Cylinder at Reynolds Number  $2 \times 10^4$ . *Flow, Turbulence and Combustion*, 92(3), pp. 673-698.
- [36] Narasimhamurthy, V.D., and Andersson, H.I., 2009, Numerical Simulation of the Turbulent Wake Behind a Normal Flat Plate. *Int. J. Heat Fluid Flow*, 30(6), pp. 1037-1043.
- [37] Rajani, B.N., Kandasamy, A., and Majumdar, S., 2016, LES of Flow Past Circular Cylinder at  $Re = 3900$ . *Journal of Applied Fluid Mechanics*, 9(3), pp. 1421-1435.
- [38] Tian, X., Ong, M.C., Yang, J., and Myrhaug, D., 2014, Large-Eddy Simulation of the Flow Normal to a Flat Plate Including Corner Effects at a High Reynolds Number. *J. Fluid Struct.*, 49, pp. 149-169.
- [39] Li, Z., Lan, C., and Ma, Y., 2012, Effects on Dust Emission from an Inclined Flat Solar Panel. Proc. ASME 2012 International Mechanical Engineering Congress and Exposition, November 9-15, pp. 619-624.
- [40] Tsuchiya, M., Tomabechi, T., Hongo, T., and Ueda, H., 2002, Wind Effects on Snowdrift on Stepped Flat Roofs. *J. Wind Eng. Ind. Aerodyn.*, 90(12), pp. 1881-1892.

- [41] Tominaga, Y., Okaze, T., and Mochida, A., 2011, CFD Modeling of Snowdrift around a Building: An Overview of Models and Evaluation of a New Approach. *Build. Environ.*, 46(4), pp. 899-910.
- [42] Franke, J., Hellsten, A., Schlünzen, H., and Carissimo, B., 2007 Best Practice Guideline for the CFD Simulation of Flows in the Urban Environment. COST Action 732, Quality Assurance and Improvement of Microscale Meteorological Models, Brussels, Belgium, p. 52.
- [43] Nasif, G., Barron, R.M., and Balachandar, R., 2014, DES Evaluation of near Wake Characteristics in a Shallow Flow. *J. Fluid Struct.*, 45(1), pp. 153-163.
- [44] Nasif, G., Balachandar, R., and Barron, R.M., 2015, Characteristics of Flow Structures in the Wake of a Bed-Mounted Bluff Body in Shallow Open Channels. *ASME J. Fluids Eng.*, 137(10), p. 101207.
- [45] Spalart, P.R., 2006, Topics in Detached-Eddy Simulation. Computational Fluid Dynamics 2004: Proceedings of the 3rd International Conference on Computational Fluid Dynamics, ICCFD3, Toronto, 12–16 July 2004, C. Groth, and D. W. Zingg, eds., Springer Berlin Heidelberg, Berlin, Heidelberg, pp. 3-12.
- [46] Bosch, G., Kappler, M., and Rodi, W., 1996, Experiments on the Flow Past a Square Cylinder Placed near a Wall. *Exp. Therm Fluid Sci.*, 13(3), pp. 292-305.
- [47] Bosch, G., and Rodi, W., 1996, Simulation of Vortex Shedding Past a Square Cylinder near a Wall. *Int. J. Heat Fluid Flow*, 17(3), pp. 267-275.
- [48] Straatman, A.G., and Martinuzzi, R.J., 2003, An Examination of the Effect of Boundary Layer Thickness on Vortex Shedding from a Square Cylinder near a Wall. *J. Wind Eng. Ind. Aerodyn.*, 91(8), pp. 1023-1037.

- [49] Shi, L.L., Liu, Y.Z., and Sung, H.J., 2010, On the Wake with and without Vortex Shedding Suppression Behind a Two-Dimensional Square Cylinder in Proximity to a Plane Wall. *J. Wind Eng. Ind. Aerodyn.*, 98(10–11), pp. 492-503.
- [50] Lee, B.-S., Kim, T.-Y., and Lee, D.-H., 2005, Control of Vortex Shedding Behind a Rectangular Cylinder near the Ground. *Numerical Heat Transfer, Part A: Applications*, 47(8), pp. 787-804.
- [51] Lan, C., Jia, L., Li, Z., and Ma, Y., 2013, Wall Effect on Separated Flow around an Inclined Flat Plate at High Incidence. Proc. ASME 2013 International Mechanical Engineering Congress and Exposition, November 15-21, p. 5.
- [52] Higuchi, H., Anderson, R.W., and Zhang, J., 1996, Three-Dimensional Wake Formations Behind a Family of Regular Polygonal Plates. *AIAA J.*, 34(6), pp. 1138-1145.
- [53] Shademan, M., and Hangan, H., 2010, Wind Loading on Solar Panels at Different Azimuthal and Inclination Angles, The 5th International Symposium on Computational Wind Engineering, Chapel Hill, North Carolina, USA, May 23-27, p. 8.
- [54] Abiola-Ogedengbe, A., Hangan, H., and Siddiqui, K., 2015, Experimental Investigation of Wind Effects on a Standalone Photovoltaic (PV) Module. *Renewable Energy*, 78, pp. 657-665.
- [55] Shademan, M., Barron, R.M., Balachandar, R., and Hangan, H., 2014, Numerical Simulation of Wind Loading on Ground-Mounted Solar Panels at Different Flow Configurations. *CaJCE*, 41(8), pp. 728-738.

- [56] Canadian Commission on Building and Fire Codes, 2005, National Building Code of Canada 2005 Volume 2. National Research Council of Canada, Ottawa, Ontario, Canada.
- [57] American Society of Civil Engineers (ASCE). Minimum Design Loads for Buildings and Other Structures. ASCE/SEI 7-05. American Society of Civil Engineers. Reston, Virginia. 2005.
- [58] Engineering Sciences Data Unit (ESDU). Strong Winds in the Atmospheric Boundary Layer. Part 1: Hourly-Mean Wind Speeds. ESDU 82026. Engineering Sciences Data Unit. London, UK. 2002.
- [59] Engineering Sciences Data Unit (ESDU). Strong Winds in the Atmospheric Boundary Layer. Part 2: Discrete Gust Speeds. ESDU 83045. Engineering Sciences Data Unit. London, UK. 2002.
- [60] Kim, T.-Y., Lee, B.-S., Lee, D.-H., Hwang, J.-H., and Lee, D.-H., 2003, A Study on Vortex Shedding around a Bluff Body near the Ground. SAE Technical Paper 2003-01-0652, p. 18.
- [61] Kim, T.-Y., Lee, B.-S., Young-Whe, P., Lee, D.-H., and Lee, D.-H., 2003, The Study on a Vortex Shedding around Square Cylinders near a Wall, 41st Aerospace Sciences Meeting and Exhibit, American Institute of Aeronautics and Astronautics, Reno, Nevada, USA, 6-9 January.
- [62] Wang, H.F., and Zhou, Y., 2009, The Finite-Length Square Cylinder near Wake. *J. Fluid Mech.*, 638, pp. 453-490.

- [63] Aly, A.M., and Bitsuamlak, G., 2013, Aerodynamics of Ground-Mounted Solar Panels: Test Model Scale Effects. *J. Wind Eng. Ind. Aerodyn.*, 123, Part A, pp. 250-260.
- [64] Ironridge, Inc., Pole Mounts. *IronRidge,, Inc.*, accessed July 10th, 2016, <http://www.ironridge.com/pole-mounts>.

## **Vita Auctoris**

NAME: Kohei Fukuda

PLACE OF BIRTH: Sapporo, Japan

YEAR OF BIRTH: 1977

EDUCATION: University of Windsor, Windsor  
2005-2008 B.A.Sc  
University of Windsor, Windsor  
2009-2012 M.A.Sc  
University of Windsor, Windsor  
2012- Ph.D.